IRAQI JOURNAL OF APPLIED PHYSICS

The *Iraqi Journal of Applied Physics (IJAP)* is a peer reviewed journal of high quality devoted to the publication of original research papers from applied physics and their broad range of applications. IJAP publishes quality original research papers, comprehensive review articles, survey articles, book reviews, dissertation abstracts in physics and its applications in the broadest sense. It is intended that the journal may act as an interdisciplinary forum for Physics and its applications. Innovative applications and material that brings together diverse areas of Physics are particularly welcome. Review articles in selected areas are published from time to time. It aims to disseminate knowledge; provide a learned reference in the field; and establish channels of communication between academic and research experts, policy makers and executives in industry, commerce and investment institutions. IJAP is a quarterly specialized periodical dedicated to publishing original papers, letters and reviews in: Applied & Nonlinear Optics, Applied Mechanics & Thermodynamics, Digital & Optical Communications, Electronic Materials & Devices, Laser Physics & Applications, Plasma Physics & Applications, Quantum Physics & Spectroscopy, Semiconductors & Optoelectronics, Solid State Physics & Applications, Alternative & Renewable Energy, and Environmental Science & Technology.

ISSN (Print): 1813-2065, ISSN (Online): 2309-1673

Editorial Office:
P. O. Box 88052, Baghdad 12631, IRAQ
Website: www.iraqiphysicsjournal.com
Emails: info@iraqiphysicsjournal.com, editor_ijap@yahoo.co.uk, ijap.editor@gmail.com,

SPONSORED AND PUBLISHED BY
AMERICAN QUALITY FOR SCIENTIFIC PUBLISHING INC.
1479 South De Gaulle Ct, Aurora, CO 80018, United States

IRAQI JOURNAL OF APPLIED PHYSICS

ISSN (Print): 1813-2065, ISSN (Online): 2309-1673

INSTRUCTIONS TO AUTHORS

CONTRIBUTIONS

Contributions to be published in this journal should be original research works, i.e., those not already published or submitted for publication elsewhere, individual papers or letters to editor.
Manuscripts should be submitted to the editor at the mailing address:

Iraqi Journal of Applied Physics, Editorial Board, P. O. Box 88052, Baghdad 12631, IRAQ
Website: www.iraqiphysicsjournal.com
Email: info@iraqiphysicsjournal.com, editor_ijap@yahoo.co.uk, ijap.editor@gmail.com

MANUSCRIPTS

Two hard copies with soft Word copy on a CD or DVD should be submitted to Editor in the following configuration:

- **One-column** Double-spaced one-side A4 size with 2.5 cm margins of all sides
- Times New Roman font (16pt bold for title, 14pt bold for names, 12pt bold for headings, 12pt regular for text)
- Manuscripts presented in English only are accepted.
- English abstract not exceed 150 words
- 4 keywords (at least) should be maintained on (PACS preferred)
- Author(s) should express all quantities in SI units
- Equations should be written in equation form (*italic* and symbolic) NOT in plain text
- Tables and Figures should be separated from text and placed in new pages after the references
- Charts should be indicated by the software used for generating them (e.g., Excel, MATLAB, Grapher, etc.)
- Figures and diagrams can be submitted in original colored forms for assessment and they will be returned to authors after provide printable copies
- Only original or high-resolution scanner photos are accepted
- For electronic submission, articles should be formatted with MS-Word software.

AUTHOR NAMES AND AFFILIATIONS

It is IJAP policy that all those who have participated significantly in the technical aspects of a paper be recognized as co-authors or cited in the acknowledgments. In the case of a paper with more than one author, correspondence concerning the paper will be sent to the first author unless staff is advised otherwise.
Author name should consist of first name, middle initial, last name. The author affiliation should consist of the following, as applicable, in the order noted:
- Company or college (with department name or company division), Postal address, City, Governorate or State, zip code, Country name, contacting telephone number, and e-mail

REFERENCES

The references should be brought at the end of the article, and numbered in the order of their appearance in the paper. The reference list should be cited in accordance with the following examples:
[1] X. Ning, R. Benford and M.R. Lovell, "On the Sliding Friction Characteristics of Unidirectional Continuous FRP Composites", *J. Tribol. Func. Mater.*, 124(1) (2002) 5-13.
[2] M. Barnes, "Stresses in Solenoids", *J. Appl. Phys.*, 48(5) (2001) 2000–2008.
[3] J. Jones, **"Contact Mechanics"**, Cambridge University Press (Cambridge, UK) (2000), Ch.6, p.56.
[4] Y. Lee, S.A. Korpela and R. Horne, "Structure of Multi-Cellular Natural Convection in a Tall Vertical Annulus", Proceedings of 7th International Heat Transfer Conference, U. Grigul et al., eds., Hemisphere (Washington DC), 2 (1982) 221–226.
[5] M. Hashish, "Waterjet Technology Development", High Pressure Technology, PVP-Vol. 406 (2000) 135-140.
[6] D.W. Watson, "Thermodynamic Analysis", ASME Paper No. 97-GT-288 (1997).
[7] C.Y. Tung, "Evaporative Heat Transfer in the Contact Line of a Mixture", Ph.D. thesis, Rensselaer Polytechnic Institute, Troy, NY (1982).

PROOFS

Authors will receive proofs of papers and are requested to return one corrected copy as a WORD file on a compact disc (CD) or by email. New materials inserted in the original text without Editor's permission may cause rejection of paper unless the handling editor is informed.

COPYRIGHT FORM

Author(s) will be asked to sign the IJAP Copyright Form and hence transfer copyrights of the article to the Journal soon after acceptance of it. This will ensure the widest possible dissemination of information.

OFFPRINTS

Authors will receive electronic offprint free of charge and any additional reprints can be ordered.

SUBSCRIPTION AND ORDERS

Annual fees (4 issues per year) of subscription are:
50 US$ for individuals inside Iraq; **200** US$ for institutions inside Iraq;
100 US$ for individuals abroad; **300** US$ for institutions abroad.

IRAQI JOURNAL OF APPLIED PHYSICS
Vol. 19, No. 3B, September 2023, pp. 3-8

Measurement of Uranium and Radon Concentrations in Wells Water Samples of Some Farms near the Mosul City in Iraq

Malik H. Kheder[1]
Hanaa N. Azeez[1]
Mushtaq A. Al-Jubbori[2]

[1] *Department of Physics, College of Education, University of Al-Hamdaniya, Ninawa Province, IRAQ*
[2] *Department of Physic, Education College for Pure Sciences, University of Mosul, Mosul, IRAQ*

The US Environmental Protection Agency recommended the uranium content safe limit for drinking water by 30 μgL^{-1}, therefore Surface well water samples from farms near Mosul city were tested for uranium and radon concentrations. The Rad7 and the CR-39 detector track registration techniques were used in measurements. The Rad7 technique discovered indicating the samples' radon levels ranged from 0.072 to 0.713 BqL^{-1}, while the CR-39 detector discovered radon concentrations ranging from 0.088 to 0.567 BqL^{-1}, uranium concentration varied from 7.162 to 45.958 μgL^{-1}. The values obtained are below the recommended safe limits of 4 to 40 BqL^{-1} by the United Nations Scientific Committee on the Effects of Atomic Radiation. The results showed that radioactive material concentrations are moderate in flat agricultural areas, low in areas near the Tigris River, and increasing in areas where mounds contain rocks. The study area is free of the effects and dangers of radioactive materials.

Keywords: Radon concentration; Uranium content; Well water, CR-39 detector
Received: 11 March 2023; Revised: 24 March 2023; Accepted: 31 March 2023

1. Introduction

Because agricultural areas rely on well water for agriculture and are the primary source of food for people, radioactive materials such as uranium and its daughter radon gas must be controlled. Radon and uranium radionuclides are naturally occurring radionuclides with varying concentrations in surface and groundwater around the world. Radon levels in groundwater generally exceed those in surface water due to the fact that uranium content in the bedrock and soil of an aquifer grows as well [1]. Groundwater radon concentrations vary greatly depending on aquifer characteristics such as geology and rock structural properties, as well as chemical form in the aquifer [2]. Because high concentrations of radon and uranium are hazardous to public health, they must be controlled by measuring their radioactivity contents. Radon concentrations in granite-underlain areas containing uranium are typically higher than in other types of rock [3]. Since uranium in the soil and rock surrounding the water source dissolves in carbonate-rich, alkaline, and oxidizing water and decomposes to radon gas, both surface water and groundwater must contain radium and radon gas [4]. Uranium concentration in the crust of earth ranged from 13.5 to 123 Bq/kg [5]. Because active fault zones are generally more permeable than the rocks around them, they serve as preferred routes for the movement of fluids [6]. High radon concentrations are linked to faults in groundwater, and radon gas escapes during movement from minerals and rocks to fluid phase environments like air and groundwater, and then to the atmosphere. Radium decay produces radon, an inert radioactive gas with a half-life of 3.8 days [7]. Nonetheless, radon concentrations are generally very low in surface water and in water bodies, particularly those used as drinking water sources. Surface water contains radon from bottom sediments diffusion, radon-laden groundwater discharge, and radium suspension and solution [8]. The global radon concentration mean value in groundwater is approximately 180 Bq/L [9]. Deposited uranium transferring to plants from water enters the food chain and becomes a risk to human health; exposure to uranium soluble at 0.1 mg/kg of body weight can damage kidney transients [10]. Drinking water is one of the human body's uranium sources, accounting for approximately 85% of ingested uranium, while food accounts for 15% [11]. The EPA's (Environmental Protection Agency) drinking water reference level for uranium is 30 µg/L [12]. Because reservoir and river water have low radon concentrations due to the possibility of radon gas escaping into the atmosphere, underground water is a significant source of radon [13]. The maximum radon level recommended by the EPA in drinking water is 11Bq/L [14].

Two methods of measurement were employed: the electrical RAD7 detector and the CR-39 detector, which counted the tracks created inside the detector by the radon's alpha particles before chemically etching them in (typically with KOH or NaOH, an alkaline solution) to increase their size, and counting the tracks per unit area (track density) by counting using optical microscopy. After that, the tracks were

transformed into radon concentrations. Radon detectors that integrate, are portable, inexpensive, and light weight are called CR-39 nuclear track detectors.

2. Experimental Work

Ten water samples were collected from ten surface wells on farms in the study area, which is located near the northwestern Mosul city in northern Iraq, 400 kilometers from Baghdad. The study area is an open flat agricultural area that is suitable for growing everything, and it is bordered by the Tigris River in the south and small mounds rich in rocks in the north, and it depends on well water for agriculture and is the main source of food for people, and because the geographical changes are very small in the region, it was taken the distance between each water well and another 3 km to cover the wells of the studied area, except for the wells of the studied area. That is, each sample represents an average area of 3km^2 from the study area, as in (Fig. 1a). The study area has the coordinates 36 ° 24'05.1 "N 43 ° 02'31.8" E. Radon concentration and the annual effective dose AED in water, measured using two techniques, the RAD7 detector (as in Fig. 1b) and CR-39 detector techniques, while uranium concentration measured by CR-39 detector.

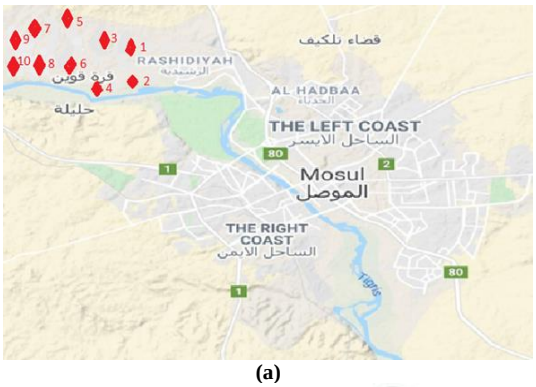

(a)

(b)

Fig. (1) (a) the site map of the studied area (samples are the red points), (b) Rad7 measurement set up

Seven samples were sent to Kirkuk University to perform RAD7 detector measurements at their lab, this detector converts radiation energy to the electrical signal directly, with 0.7-liter hemisphere the internal cell sample is, coated with the electrical conductor from inside, at the hemisphere center, a planar, ion-implanted, solid state, silicon alpha detector. Water 250 protocol with capacity of 250 ml vials used, which configures RAD7 automatically to a test performed according to parameters selected. Five minutes the pump runs, for the sample aerating and the radon delivering to the RAD7. Five more minutes of waiting later, the system starts counting. Five minutes later, it will print the report. Same thing each five minutes will happen again consequently. After 30 minutes the run period from the start, summary prints out by Rad7, showing the reading of average radon from counted four cycles, the cumulative spectrum of these four readings and the bar chart. The water sample radon concentration is calculated by the RAD7 automatically after that. Excluding the spectrum, all data will be printed and will in the memory be stored [15]. CR-39 Detector measurements, the radon dosimeter of plastic can with dimensions (7cm diameter, 29 cm length), with CR-39 detector placed on the bottom of dosimeters cover, and used to measure the samples radon concentration as in (Fig. 2a). Samples filled and stored in the plastic can for exposure time 60 days, 115.4 ml of water with 3cm highest, placed in the dosimeter, the distance from water samples to the detector surface was 26 cm. After 60 days an exposure time, detectors removed from the dosimeter, and chemically etched in NaOH solution of normality 6.25N at 70◦ C for 7 hours. The tracks counted using a 400x optical microscope.

The sample tracks density (ρ_x), obtained by dividing the number of tracks over the area of optical microscope field of view. The water sample's radon concentrations obtained using the comparison between the track densities of standard water samples and the registered by the detectors from the samples, as shown in (Fig. 2b), using the equation [16]

$$C_x = \rho_x \left(\frac{C_S}{\rho_S}\right) \quad (1)$$

Where C_x is the concentration of radon in the unknown sample, ρ_x (track/mm^2) is the unknown sample track density, C_s is the standard sample radon concentration, ρ_s (track/mm^2) is the standard sample track density, C_s/ρ_s =1/slope.

Then C_{Rn}= C_x is the radon levels in the water samples measured in units (Bq/L).

Water effective annual dose AED by the radon intake, obtained from the relation in units of μSv/y [17].

$$AED_W = C_{Rn} C_{RW} D_{CW} \quad (2)$$

Where C_{Rn} is a radon concentration in a unit (Bq/L), in the ingested water, C_{RW} is the rate of water consumption in (730 L/y), and D_{CW} (5×10^{-9} Sv/Bq) is the factor of conversion to Sievert units from Becquerel [18].

 ISSN (print) 1813-2065, (online) 2309-1673

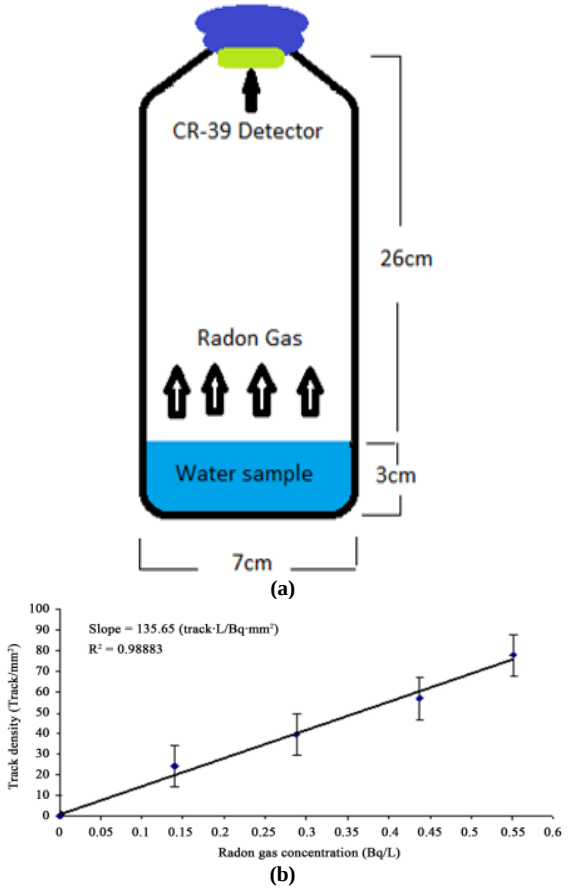

Fig. (2) (a) Radon dosimeter (Plastic can), (b) The relation between the track density, and the radon concentration, in the standard water samples

Uranium contents calculated by the secular activity equilibrium between uranium and its daughters using the radon concentration obtained from the CR-39 detector. The activity of radon A_{Rn} in the sample calculated from C_{Rn} the concentration of radon in the sample using the relation [19]

$$A_{Rn} = C_{Rn} V \quad (3)$$

Where ($V=\pi r2\ L$) =115.4 X 10^{-6} m^3=115.4 mL is the sample volume, the thickness of sample is L = 0.03 m, the radon dosimeter radius is r = 0.035m, thus

$$\lambda_{Rn} N_{Rn} = A_{Rn} \quad (4)$$

The uranium atoms number N_U in the samples calculated from the equation of the equilibrium between uranium with its daughter (the uranium activity equal the radon activity) [20]

$$\lambda_U N_U = \lambda_{Rn} N_{Rn} \quad (5)$$

Where the decay constant of uranium is λ_U=(4.883X10^{-18} s^{-1}). The uranium weight in samples then calculated by the uranium atoms number N_U using the equation

$$W_U = \frac{N_U a_U}{N_{avo}} \quad (6)$$

Where a_U is the uranium mass number ^{238}U, N_{avo}= (6.02X10^{23} atom/Mol) is the number of Avogadro, then W_U in micrograms units (µg). The concentration of uranium, calculated by [21]

$$C_U = \frac{W_U}{W_S} \quad (7)$$

C_U is the uranium concentration in (µg/L) units, where Ws = 115.4 mL (millilitre).

3. Results and Discussion

Results from employing CR-39 and RAD7 detectors on well water samples are listed in table (1). Results from RAD7 revealed the amount of radon present in water samples C_{Rn} varied from 0.072 to 0.713 Bq/L as shown in (Fig. 3a), with a mean value of 0.320 Bq/L, where the low value is in the sample number 4 which is taken from 8-meter depth surface well-located near Tigris river, as in site map of the samples, the high value in the sample number 5 from well of 40 meters deep in mounds area rich with rocks, far from river about 9km so the deeps of well increased, so concentrations increased by rocks, other samples showed moderate concentrations of radon because they are in flat agricultural areas, and the effective annual dose AED_W are in the range of 0.262-2.602 µSv/y and a mean value of 1.170 µSv/y.

Table (1) The CR-39 and RAD7 detectors, results of radon concentrations, the annual effective dose, and uranium concentrations

Sample	CR-39 Detector				RAD7 Detector	
No.	ρ track/m²	C_{Rn} (Bq/L)	AED_W (µSv/y)	C_U (µg/L)	C_{Rn} (Bq/L)	AED_W (µSv/y)
1.	32	0.235	0.861	19.099	0.289	1.054
2.	21	0.154	0.565	12.534	0.134	0.489
3.	47	0.346	1.264	28.052	0.363	1.324
4.	12	0.088	0.322	7.162	0.072	0.262
5.	77	0.567	2.071	45.958	0.713	2.602
6.	28	0.206	0.753	16.712	0.234	0.854
7.	53	0.390	1.426	31.633	0.439	1.602
8.	29	0.213	0.780	17.309		
9.	44	0.324	1.183	26.261		
10.	28	0.206	0.753	16.712		
min	12	0.088	0.322	7.162	0.072	0.262
max	77	0.567	2.071	45.958	0.713	2.602
mean	37.1	0.273	0.998	22.143	0.320	1.170

The radon concentration in water samples was determined by the CR-39 detector to be varied from 0.088 to 0.567 Bq/L, shown in (Fig. 3b), and the mean value of 0.273 Bq/L, the effective annual dose AED_W are in the range of 0.322-2.071 µSv/y with mean value of 0.998 µSv/y, and the concentrations of uranium C_U in water samples are in the range (7.162-45.958 µg/L) with the mean value of 22.143 µg/L. The comparison between RAD7 and CR-39 results for radon concentrations in sample showed that the results of CR-39 are very small amount less than the RAD7 results as seen in (Fig. 3c), and (Fig. 3d) demonstrates that a strong positive correlation (0.9854) between the two detectors used to measure the amount of radon in water samples has been found. It is indicated that the tow detector's results are close together.

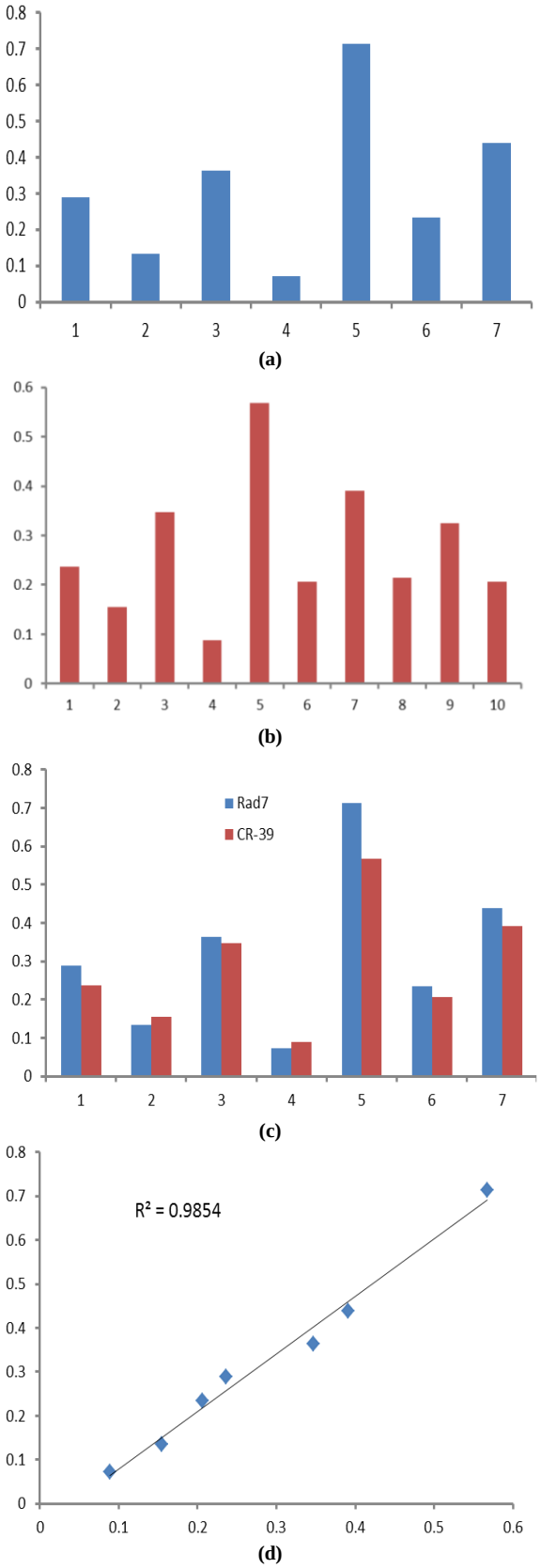

Fig. (3) (a) Radon concentration CRn (Bq/L) in samples using Rad7 technique, (b) Radon concentration in samples by using CR-39 technique, (c) Comparison the radon concentration in samples of tow techniques, Rad7 (Blue), and CR-39 (Red), (d) Comparison between the Rad7and CR-39 detectors

The modest variations in radon concentrations between individual wells in the study area were caused by changes in the soil's geological composition. All measured concentrations of radon in the wells water samples were in the international recommended safe limits concentration, US Agency of Environmental Protection proposed the concentration level of the radon in water for drinking is 11 Bq/L equal to 11000 Bq/m^3, and a maximum contaminant alternative level is 148 Bq/L equal to 148000 Bq/m^3. The agencies of environmental and health protection recommended the safe limit of 4-40 Bq/L for human beings of the content of radon in the drinks water [22]. The obtained results for uranium concentrations are within the 30 µg/L normal uranium concentration level rate for the drinking water based with guidelines of the World Health Organization. The high rate availability of uranium in some regions, is the source of dangerous to public safety and health, so it no danger in studied area to human life, no treatment is needed. The comparison of obtained results with other works in this field using CR-39 and RAD7 detectors showed in (table 2).

Table (2) The comparison of CR-39 and RAD7 detectors results, with the results of the other authors

Research	Radon C_{Rn}(Bq/L)	AED_W (µSv/y)	Uranium C_U (µg/L)	Reference
CR-39 Detector				
Present work	0.088 - 0.567	0.322- 2.071	7.162-45.95	
Nineveh plain region-Iraq	0.362- 1.485	1.32- 5.42	28.76-120	[23]
ThiQar Governorate -Iraq	0.108 - 0.223	0.394- 0.814		[24]
Wassit Governorate -Iraq	0.325- 0.820	0.03- 0.08		[25]
Kirkuk -Iraq	0.063- 0.196		119-363	[26]
Baghdad-Iraq	0.308- 0.881	7.78- 22.24		[27]
Al-Najaf-Iraq			0.254-3.78	[28]
Babylon-Iraq	1.7-5.83			[29]
Basra-Iraq	2.050			[30]
Karbala-Iraq	2.156- 4.112	7.86 -15		[31]
East Anatolian-Turkey	0.1325- 3.319			[32]
RAD7 Detector				
Present work	0.072 - 0.713	0.262- 2.602		
Kirkuk Governorate-Iraq	0.108- 5.630	10.136		[33]
Basra Governorate-Iraq	0.034- 15.531	0.1- 0.843		[34]
Abu- Gharaq, Babylon-Iraq	0.072- 0.688	0.315- 3.013		[35]
Kufa city – Iraq	0.267- 5.662			[36]
Qassim area-Saudi Arabia	0.76 - 9.15	2.77- 33.39		[37]
Ashanti Region-Ghana	0.04-0.16	0.28- 1.14		[38]
Sungai Petani - Malaysia	5.37- 14.7			[39]
NITJ, Punjab-India	2.56-7.75			[40]

The obtained results for radon concentrations are within the measurements of most other researches results, for CR-39 detector less than the

 ISSN (print) 1813-2065, (online) 2309-1673

measurements of all other authors but higher than Kirkuk governorate results. The comparison showed lower results values with the other authors for RAD7 detector, much less than other countries, higher than Ghana results, the table showed comparison of AED_W and uranium concentrations.

4. Conclusion

The study's aim was to assess the uranium and radon contents of water samples in certain farming wells around Mosul City in Iraq and to introduce the surface wells water radiation levels due to the significance of water in the environment and human existence. Because high radiation levels in water are hazardous to public health, radiation concentration measurements in well water are critical. Radon independent behavior revealed that uranium concentrations in well water samples increased in areas rich in rocks, indicating that water and rock interact. The results showed that radioactive material concentrations are moderate in flat agricultural areas, low in areas near the Tigris River, and increasing in areas where mounds contain rocks. The research area is free of the impact and dangers of radioactive materials.

Acknowledgments

We acknowledge to Prof. Dr. Ahmed Abed Ibrahim, the Assistant to the President of the University of Kirkuk for Scientific Affairs, to provide facilities for making measurements on a RAD7 detector in the laboratory of the Kirkuk University.

References

[1] G. Knutsson and B. Olofsson, "Radon content in groundwater from drilled wells in the Stockholm region of Sweden", *Norg. Geol. Under. Bull.*, 439 (2002) 79–85.

[2] G. Igarashi et al., "Ground-water radon anomaly before the Kobe earthquake in Japan", *J. Sci.*, 269(5220) (1995) 60–61.

[3] B.W. Cho et al., "Spatial relationships between radon and topographical, geological, and geochemical factors and their relevance in all of South Korea", *J. Env. Earth Sci.*, 74(6) (2015) 5155–5168.

[4] M.S. Alam and T. Cheng, "Uranium release from sediment to groundwater: Influence of water chemistry and insights into release mechanisms", *J. Contam. Hydrol.*, 164 (2014) 72–87.

[5] I. Bikit et al., "Radioactivity of the soil in Vojvodina (Northern province of Serbia and Montenegro)", *J. Env. Radioact.*, 78(1) (2005) 9-11.

[6] M.M. Moussa and A.M. El Arabi, "Soil radon survey for tracing active fault: a case study along Qena-Safaga road, Eastern Desert, Egypt", *J. Rad. Measur.*, 37(3) (2003) 211-216.

[7] B.W. Cho et al., "A preliminary investigation of radon concentrations in groundwater of South Korea", *J. Soil Groundwater Env.*, 12(5) (2007) 98-104.

[8] C.R. Cothern and J. Smith, **"Environmental Radon"**, 35, Springer Science & Business Media (2013).

[9] L. Beach, "Exposure from the Uranium Series with Emphasis on Radon and Its Daughters, Report No. 77. National Council on Radiation Protection and Measurements", *J. Nucl. Med.*, 25(11) (1984) 1273-1274.

[10] R. Munitions, "The health effects of depleted uranium munitions: a summary", *J. Radiol. Prot.*, 22(2) (2002) 131.

[11] C.R. Cothern and W.L. Lappenbusch, "Occurrence of uranium in drinking water", *J. Health Phys.*, 45(1) (1983) 89-99.

[12] EPA, "US Environmental protection agency edition of the drinking water standards and health advisories tables", 822-F-18-001 (2018).

[13] M.S. Al-Nafiey, M.S. Jaafar and S. Bauk, "Measuring radon concentration and toxic elements in the irrigation water of the agricultural areas in Cameron highlands", *J. Sains Malaysiana*, 43(2) (2014) 227-231.

[14] EPA, "US Environmental protection agency, "Federal Register: November 2, 1999, Part 2. 40 CFR Parts 141 and 142. National Primary Drinking Water Regulations: Radon-222: Proposed Rule", (Federal Register Washington, DC 1999).

[15] J.M. Lee and G. Kim, "A simple and rapid method for analyzing radon in coastal and ground waters using a radon-in-air monitor", *J. Env. Radioact.*, 89(3) (2006) 219-228.

[16] S.A. Durrani and R.K. Bull, **"Solid State Nuclear Track Detection: Principles, Methods and Applications"**, 111, Elsevier (2013).

[17] M.H. Kheder, H.N. Azeez and F.M. Al-Jomaily, "Alpha emitters radioactivity concentrations in some cosmetics used in Iraq using LR-115 detector", *J. Eureka: Phys. Eng.*, (2) (2020) 65-70.

[18] M.N. Alam et al., "Radiological Assessment of Drinking Water of the Chittagong Region of Bangladesh", *J. Rad. Protect. Dosim.*, 82(3) (1999) 207-214.

[19] K.O. Abdullah, S.Z. Muhammed and A.M. Hussein, "Assessment of Rn and U Concentrations in the Soil of Qadafery, Kalar and Zarayan Located in Sulaimani Governorate of Kurdistan Region, Iraq", *Am. J. Env. Protect.*, 4(1) (2015) 40-44.

[20] H. Cember, T.E. Johnson and P. Alaei, **"Introduction to health physics, Medical Physics"**, 35 (2008) 5959.

[21] M.H. Kheder et al., "Radioactivity concentrations in barley and wheat crops in

Nineveh plain region in Iraq", *Int. J. Nucl. Ener. Sci. Technol.*, 14(1) (2020) 50-60.
[22] S. Mittal, A. Rani and R. Mehra, "Estimation of radon concentration in soil and groundwater samples of Northern Rajasthan, India", *J. Rad. Res. Appl. Sci.*, 9(2) (2016) 125-130.
[23] M.H. Kheder et al., "Radon and uranium concentration in ground water of Nineveh plain region in Iraq", J. Phys.: Conf. Ser., 1234(1) (2019).
[24] L.A. Najam et al., "Measurement of Radon Gas Concentrations in Tap Water Samples for Thi-Qar Governorate Using Nuclear Track Detector (CR-39)", *Detection*, 4(01) (2016) 1-8.
[25] L.A. Najam, M.S. Karim and T.K. Hameed, "Measurement of Radon Gas Concentration in Tap Water Samples in Wassit Governorate by Using Nuclear Track Detector (CR-39)", *Int. J. Phys.*, 4(5) (2016) 119-122.
[26] N.F. Salih, Z.M. Jafri and M.S. Jaafar, "Measurement of radon concentration, and uranium concentration in drinking water in Kirkuk governorate", *J. Sci. Res. Develop.*, 2(13) (2015) 127-131.
[27] B.K. Rejah et al., "Estimate Level of Radon Concentration for Drinking Water in Some Regions of Baghdad City", Arab. J. Sci. Eng., 43(7) (2018) 3831-3835.
[28] A.A. Abojassim and H.A. Mohammed, "Comparing of the uranium concentration in tap water samples at Al-Manathera and Al-Herra Regions of Al-Najaf, Iraq", *Karbala Int. J. Mod. Sci.*, 3(3) (2017) 111-118.
[29] S.H. Lefta and J.H. Ibrahim, "Radon Concentration of Ground Water in Babylon Governorate", *J. Acad. Res. Int.*, 4(3) (2013) 260.
[30] A.H. Subber, M.A. Ali and T.M. Al-Asadi, "The Determination of Radon Exhalation Rate from Water using Active and Passive Techniques", *J. Adv. Appl. Sci. Res.*, 2(6) (2011) 336-346.
[31] I.T. Al-Alawy and A.A. Hasan, "Radon Concentration and Dose Assessment in Well Water Samples from Karbala Governorate of Iraq", J. Phys.: Conf. Ser., 1003(1) (2018) 12117.
[32] O. Baykara and M. Dogru, "Measurements of radon and uranium concentration in water and soil samples from East Anatolian Active Fault Systems (Turkey)", *J. Rad. Measur.*, 41(3) (2006) 362-367.
[33] A.A. Ibrahim, I.Z. Hassan and S.H. Moklofe, "Radon Concentrations in Tap and Ground Water in Kirkuk Governorate Using Active Detecting Method RAD7", The Int. J. Phys., 5 (2017) 37-42.
[34] M.A. Ali, "Measuring the concentrations of radon gas ^{222}Rn naturally-emitted from water samples selected from the marshes of Basra Governorate, southern Iraq", *Iraqi J. Aquacult.*, 17(2) (2020).
[35] K.H. Hatif, M.K. Muttaleb and A.H. Abass, "Measurement of Radioactive Radon Gas Concentrations of Water in the schools for Abu Gharaq", *J. Univ. Babylon Pure Appl. Sci.*, 26(1) (2018) 174–80.
[36] A.A. Al-Hamadwi, A.A. Al-Bayati and A.H. Al-Mashhadani, "Radon and Thoron Concentration measurement of Ground Water in Kufa City by using RAD7 detector ", *J. Kufa Phys.*, 4(2) (2012) 44-49.
[37] W.R. Alharbi, A.E. Abbady and A. El-Taher, "Radon Concentrations Measurement for groundwater Using Active Detecting Method", *Am. Sci. Res. J. Eng. Technol. Sci.*, 14(1) (2015) 1–11.
[38] I. Opoku et al., "Annual effective dose of radon in groundwater samples for different age groups in Obuasi and Offinso in the Ashanti Region, Ghana", *Environ. Res. Commun.*, 1(10) (2019) 105002.
[39] N. Ahmad, M.S. Jaafar and M.S. Alsaffar, "Study of radon concentration and toxic elements in drinking and irrigated water and its implications in Sungai Petani, Kedah, Malaysia", *J. Radiat. Res. Appl. Sci.*, 8(3) (2015) 294-299.
[40] K. Badhan, R. Mehra and R.G. Sonkawade, "Measurement of radon concentration in ground water using RAD7 and assessment of average annual dose in the environs of NITJ , Punjab", *Indian J. Pure Appl. Phys.*, 48 (2010) 508-511.

 ISSN (print) 1813-2065, (online) 2309-1673 PRINTED IN IRAQ

IRAQI JOURNAL OF APPLIED PHYSICS
Vol. 19, No. 3B, September 2023, pp. 9-14

Indoor Radon Measurements in Some Nineveh Plain Region Homes Using a Small Container with CR-39 Detector

Hanaa N. Azeez
Rajaa A. Basheer
Malik H. Kheder

Department of Physics, College of Education, University of Al-Hamdaniya, Ninawa Province, IRAQ

In the environment and living homes it is necessary to evaluate the radon inhalation dose and its progeny on a regular basis because Radon is carcinogenic agent. Radon concentrations in homes in the Nineveh plain region were measured in this study using a passive personal radon monitor with a CR-39 detector in the small container for contact lenses storing. The determined concentrations of radon ranged from 50.50 to 120.65 Bq.m^{-3}, the excess lifetime cancer risk (ELCR) was in the range of 9.26x10^{-3} to 22.13x10^{-3}, and the lung cancer cases (LCC) incidence per million people per year was in the range of 103x10^{-9} to 248x10^{-9}. The mean radon concentration found fell below the World Health Organization's (WHO) permitted level of 100 Bq.m^{-3}. The research area is still free of significant radon concerns despite certain values being above the permitted limit.

Keywords: Effective annual dose; Radon concentration; Alpha potential energy; CR-39 detector
Received: 11 March 2023; Revised: 24 March 2023; Accepted: 31 March 2023

1. Introduction

Radon is an ionizing radioactive gas that occurs naturally as a result of the breakdown of uranium. Uranium and radium are the primary sources of indoor radon because they are naturally occurring elements in rocks, soil, and building materials [1]. When people are exposed to high levels of radon and its daughters for an extended period of time, Pathological effects occur, such as changes in respiratory function and the emergence of lung cancer. Radioactive particles that can be absorbed and become stuck in lung tissues are created as radon gas gradually breaks down [2]. Leukemia and other malignancies, such as melanoma, kidney, and prostate cancer, have been related to an increased chance of developing due to indoor radon exposure [3], so it is necessary to evaluate radon concentrations in the environment and living homes on a regular basis, which can be easily detected using radon measurement devices. Radon concentrations have recently been measured using nuclear solid-state track detectors. Because of their low price, compact size, and simplicity of use, these detectors are a great option [4]. Many authors and laboratories around the world have developed dosimeters and detectors of various types to assess indoor radon concentrations using passive-type monitors that record long-term readings [5]. Small size dosimeters developed are used as personal dosimeters and to measure indoor radon concentrations. Some examples of developed dosimeters include: A little black box with dimensions of 4.0x7.5x0.5 cm is the Kodalpha radon dosimeter. A film tag fastened to the interior of the lid's hinge serves as the dosimeter's actual radon sensor. The nuclear solid state track detector (SSNTD) method was used to develop the LR-115 type-II track plastic detectors used in these film badges by Kodak-Path in France. These detectors were used to gauge radon levels and are particularly beneficial for direct alpha particle registration. KODAK's more than 30 years of experience with SSNTD technology have yielded these superior films [6- 9]. The NRPB- passive type personal dosimeter of radon is made from the plastic and is composed of two parts: the CR-39 track detector, which is housed inside the dosimetric cassette and measures 5.5 cm in diameter and 2 cm in thickness. The diffusion cup-based NRPB dosemeter is intended for use in mines with high relative humidity levels. The NRPB-type dosimeter's key design feature is that, after it is closed, only radon can pass via microcavities and reach the interior. As a result, Regardless of the number of radon daughters present in the air, the radon concentration inside the dosimetric chamber reaches a level that is identical to that found in the ambient air. It is possible to establish the average radon content in the air during a certain measurement period. An NRPB dosimeter is hence a tool used to gauge radon exposure [10, 11]. The Altrac model PD radon personal dosimetry system makes use of radiation detector diffusion chambers based on nuclear track detectors. The dosimeters are divided into lower sections with built-in detector holders and higher sections with domes. A square CR-39 detector is placed in the center of the lower parts to provide security. The housings are created from a special plastic blend that includes steel fiber. The plastic's polymer matrix and the dosimeters' interior are penetrated by radon in about 9 minutes. This guarantees that the measurements are unaffected by

the radon isotopes ^{220}Rn and ^{219}Rn, which have half-lives respectively of 3.96 and 55.6 seconds [12]. It was possible to create a low-cost, transportable, and simple-to-find passive personal radon monitor out of a small contact lens storage container. There was 3.2 cm3 of liquid in each container. One CR-39 piece was secured at the top of each container using adhesive clay and a 1 cm^2 CR-39 detector as the detecting material. Earlier passive radon monitors' containers were made of electro-conductive materials to avoid electrostatic phenomena that can cause an uneven radon progeny deposition. Thoron is prevented from entering the monitor by the air gap formed by the covers on each container. The monitor was placed in the Institute of Radiation Emergency Medicine's radon calibration chamber, where the conversion factor (CF) to radon concentration was later obtained (IREM) [13].

This study aims to establish the indoor radon concentration levels in dwellings in the Nineveh Plain area using a passive radon personal monitor with a CR-39 detector in a small container for storing contact lenses, as well as the annual effective dosage of radon to which people are exposed. The necessity of radon measurement to routinely monitor radon concentrations in occupied buildings and guarantee their suitability for human habitation emphasizes the significance of this study.

2. Experimental Work

Mean long-term indoor radon concentrations were measured in 45 homes in the Nineveh plain region using a passive small container dosimeter with a CR-39 detector, which is similar to the small size dosimeters mentioned in the introduction. The used container was a contact lens storage container similar to the one used in ref. [13] because it is simple to use, inexpensive, and widely available. The contact lens storage consisted of two storage compartments, the alpha track detector CR-39 was used as a piece 1×1cm^2 in size and fixed in the top cover of each storage compartment, the 3 mm diameter hole made in the bottom of the right hand storage compartment used to radon measurement, the lift hand without hole used as background measurement to ensure they were in the same environment, and each home was coded with a number. Dosimeters were placed in a room away from the floor at a height of 2.00-2.25 m, 50 cm away from walls, windows, and sunlight for 90 days. Fig. (1) depicts the used container and its diagram.

The measurements were only carried out in rooms on the ground level of homes in the studied area, the sitemap of the study area is given in Fig. (2).

The concentration of radon (C_{Rn}) was determined by the equation.

$$C_{Rn} = \frac{N-N_0}{CF_{Rn}.T} \quad (1)$$

where C_{Rn} is the average radon concentration over the exposure time in kBq/m^3, N_0 and N are the background and the track density in the measurement in (tracks/cm^2) respectively, and T in unit of hours is the exposure time, CF_{Rn} is the conversion factor for radon concentration, which was discovered during a calibration test and has the value (2.0±0.3 tracks/cm^2 per kBq.h/m^3) from reference [13].

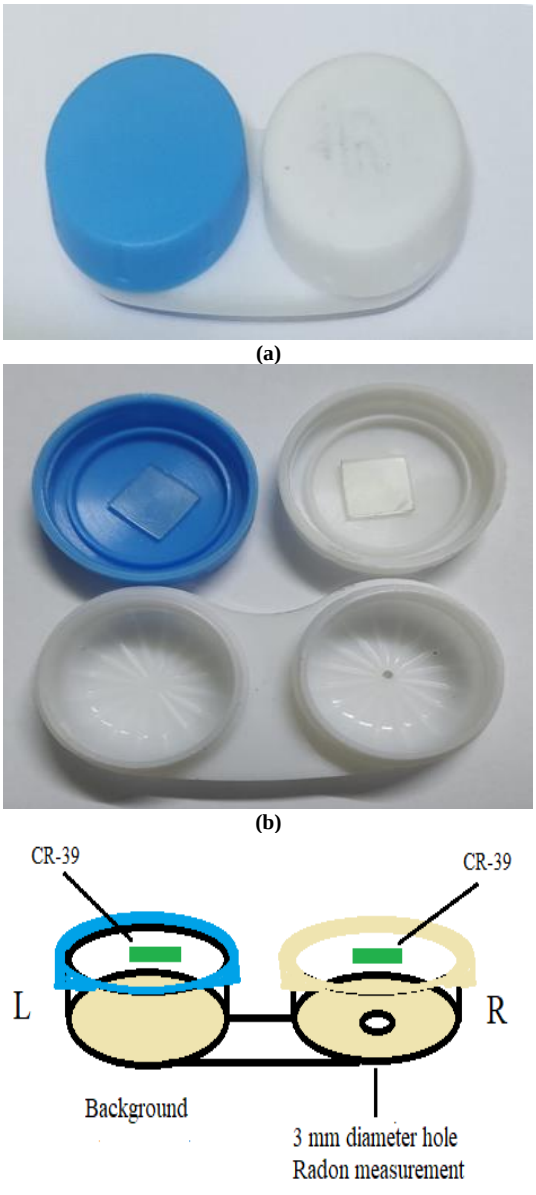

Fig. (1) View of the small container for storing contact lenses used as a passive radon monitor; (a) closed storing contact lenses, (b) opened storing with CR-9 detector, and (c) schematic representation of the monitor

The effective annual dose (AED) for radon in units (mSv.y^{-1}) was determined using the following formula:

$$AED = C_{Rn}.O.F.T.D \quad (2)$$

where C_{Rn} is the concentration of radon in (Bq/m^3), O is the occupancy factor (0.8), F is the equilibrium factor (0.4), T (8760 h/y) is the one-year duration in hours [14], and D is the conversion factor from (Bq.m^{-3}) to mSv.h^{-1}. Based on recent epidemiological studies and dosimetric model, the International Commission on Radiological Protection (ICRP) in 2017 suggested a new dose conversion factor for

 ISSN (print) 1813-2065, (online) 2309-1673

radon in structures and underground mines of (17 nSv per Bq.h.m^{-3}= 17×10^{-6} mSv.h^{-1} (Bq.m^{-3})$^{-1}$) [15,16].

LCC is the estimated annual incidence of lung cancer per million population, as determined using the equation. [17].

$$LCC = 18 \times 10^{-6} E_{Inh} \quad (3)$$

where 18x10^{-6} is a lung induction cancer risk factor expressed in units of mSv^{-1}, and E_{Inh} is the computed lung yearly equivalent dose, which can be computed using the equation.

$$E_{Inh} = AED.W_R.W_T \quad (4)$$

where W_R is the weighting factor for radiation (20 for particles) and W_T is the weighting factor for tissue (0.12 for lung) [18].

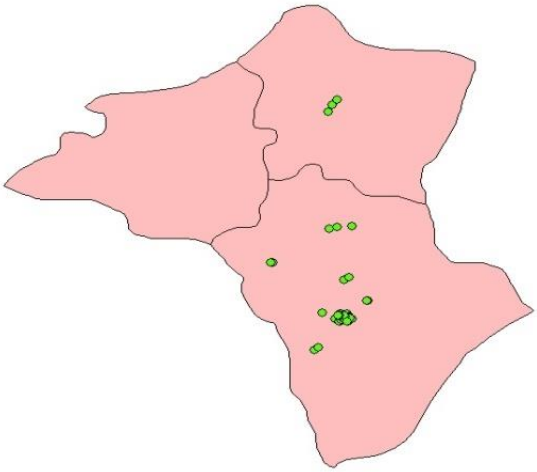

Fig. (2) The sitemap of the study area

Excess lifetime cancer risk (ELCR) is defined as potential carcinogenic effects that estimate the incidence probability of cancer in individuals in the population for a specific exposure lifetime based on dose–response data. The intake is multiplied by the slope factor to achieve this. The results of the ELCR are a matter of probability. Cancer is more likely to develop as a result of a person's lifetime exposure to toxic substances. The ELCR is concerned about the lifetime risk of developing cancer as a result of exposure. The equation produces the ELCR in million people per year (MPY).

$$ELCR = AED.DL.RF \quad (5)$$

where DL is the life duration (70 years), and RF is the risk factor (0.055 Sv^{-1}) [19].

Measurements of Alpha Potential Energy Concentration (PAEC) are necessary to determine the amount of radon gas and its byproducts in the air and its effective concentration. This amount eliminates the need to measure the concentration of each isotope separately by reflecting the total concentration of radon and its offspring from short-lived radon isotopes in one indicator. Its value is expressed in terms of the unit (WL), which is the work level in locations where radon gas has been fully dissolved in lead ^{210}Pb. The base working level concentration of dissolution products in equilibrium with (100 pCi/L) of parent radon ^{222}Rn. The (100 pCi/L) can be converted to (Bq.m^{-3}), and the concentration-energy concentration can be measured in units (Bq.m^{-3}). Alpha potential energy concentration is determined using the equation [20].

$$PAEC_{(WL)} = \frac{F\,C_{Rn}}{3700} \quad (6)$$

PAEC is the short-lived progeny of radon's potential alpha energy concentration in air (in WL units), where 1 WL = 3700 Bq.m^{-3} [21].

3. Results and Discussion

The findings from CR-39 detector of indoor radon measurements in some Nineveh plain region homes and other derived parameters are listed in table (1).

Indoor radon levels were measured in 45 homes in the Nineveh plain region. The levels of radon knowledge in these homes are critical to the safety and well-being of civilians, so maintaining a safe radon concentration in the homes is one of the primary sustainability plans for ensuring a safe living environment for people. Indoor radon measurements are taken in the ground level of homes in the study area, where radon accumulates due to its heavier than air nature. Radon levels measured ranged from 50.50 to 120.65 Bq.m^{-3}, with a mean of 72.82 Bq.m^{-3}, as illustrated in Fig. (3).

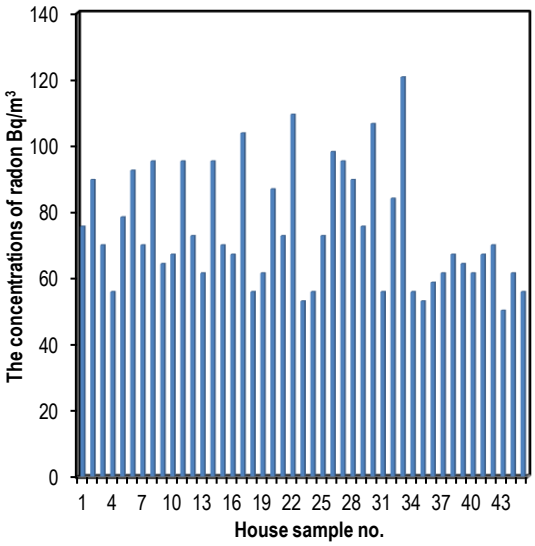

Fig. (3) Radon concentrations in the studied houses

Figure (3) shows that the home sample number 33 has the highest radon concentration and is located in Sinharip Q in Al-Hamdaniya city. The sample number 43 has the lowest radon concentration. Radon is emitted by the Earth's crust, with the highest concentrations found in ground-level structures. The radon concentration values obtained are lower than the WHO Organization of World Health reference level of 100 Bq.m-3 [22], with the exception of some homes, which are higher than this reference level but have a lower mean value. All obtained values are less than the European Commission and the UK National Board of Radiation Protection (NRPB) recommended level of 200 Bq.m^{-3} [23]. In the studied area, there is

no high radon risk. Radon concentrations indoors are reduced by the increased movement and air exchanges provided by fans and air conditioning. There is no need to take any action in regards to the construction materials. Despite the fact that low levels of radon exposure can cause lung cancer, the research site is free of radon-related health risks and radiological risks.

As radon concentrations, the other parameters are higher in sample 33 lower in sample 43, the AED annual effective dose ranged from 2.40 to 5.74 mSv/y, with a mean value of 3.470 mSv/y, the LCC ranged from 103.97×10^{-9} to 248.38×10^{-9} with a mean value of 149.926×10^{-9}, implying that this radon concentration range can cause 103-248 lung cancers per Billion people per year, and the ELCR due to radon exposure ranging from 9.266×10^{-3} to 22.135×10^{-3}. The Potential alpha energy concentration PAEC ranged from 2.07 to 6.97 mWL, with a mean of 4.48 mWL, the relationship between radon levels and the number of PAEC is depicted in Fig. (4).

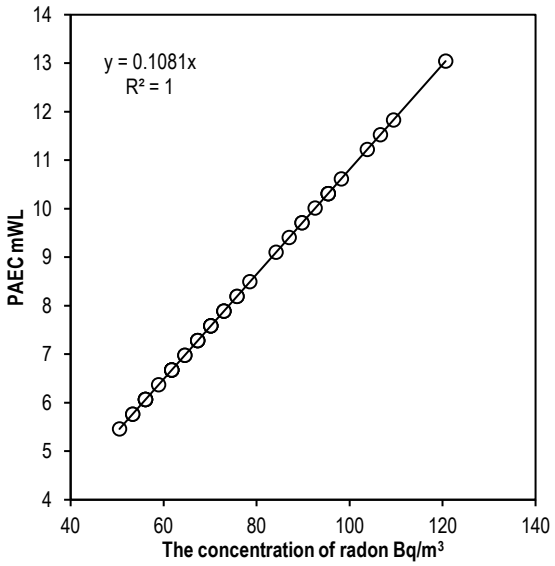

Fig. (4) The relationship between PAEC and radon concentration

Figure (4) shows the strong positive correlation (1.00) found between radon concentration and PAEC demonstrated that as radon content increased, so did the PAEC. The current study's findings are compared to some previous studies in Iraq and with Turkey, which is the closest country to the studied area are listed in table (2).

The current study's radon concentration results are lower than previous studies in the Ainkawa region of Kurdistan in Iraq, Izmir in Turkey, and higher than the other studies. The annual effective dose mean value is higher than in all previous studies due to the use of the new recommended dose conversion factor 17 nSv per Bq h m^{-3} for radon in buildings by the International Commission on Radiological Protection (ICRP) in 2017 [15], which is twice the old dose conversion factor 9 nSv per Bq h m^{-3} given by the UNSCEAR 2006 report on the sources and effects of ionizing radiation [29]. The variation in mean radon concentration values across studies could be explained by radon-influencing factors. The geology of the various locations is one of the most important factors in each study.

4. Conclusions

One of the most important long-term plans for ensuring the levels of radon knowledge in the homes are critical to the safety and well-being of civilians, so the primary sustainability plans for ensuring a safe living environment for peoples is to maintain a safe radon concentration in the homes. Radon is emitted by the Earth's crust, and the highest concentrations are found in ground-level structures. The radon concentration values obtained are lower than the WHO Organization of World Health reference level of 100 Bq.m^{-3}, except in some homes, which are higher than this reference level but have less of it on average, and the high-value reason is that the air conditioning lacks ventilation, causing ventilation in this building to be reduced. Radon concentrations indoors are reduced by the increased movement and air exchanges provided by fans and air conditioning. There is no need to take any action in regards to the construction materials. Despite the fact that low levels of radon exposure can cause lung cancer, the research site is free of radon-related health risks and radiological risks. The radon concentration results in the present study are withen than previous studies, but the annual effective dose mean value is higher than all the other previous studies because the using of the new recommended dose conversion factor for radon in buildings by the International Commission on Radiological Protection (ICRP) in 2017, which is twice the old dose conversion factor given by the UNSCEAR 2006 report. The LCC values obtained indicate that implying that this radon concentration range can cause 103-248 lung cancers per Billion people per year. There is no high radon risk in the homes of the studied area.

References

[1] G. Degu Belete and Y. Alemu Anteneh, "General Overview of Radon Studies in Health Hazard Perspectives", *J. Oncol.*, 2021, Article ID 6659795.

[2] BEIR VI, National, Research (Nat. Acad. Press, Washington, DC, 1999).

[3] D.L. Henshaw, J.P. Eatough and R.B. Richardson, "Radon as a causative factor in induction of myeloid leukaemia and other cancers ", Epidemology, 335(8696) (1990) P1008-1012.

[4] H.N. Azeez et al., "Radon Concentration Measurement in Ainkawa Region Using Solid

 ISSN (print) 1813-2065, (online) 2309-1673

State Nuclear Track Detector", *Iraqi J. Sci.*, 59(1C) (2018) 482-488.

[5] A.C. George, T. Weber, "An Improved Passive Activated C Collector for Measuring Environmental ^{222}Rn in Indoor Air", *Health Phys.*, 58(5) (1990) 583-589.

[6] N. Dwaikat, G. Safarini, M. El-hasan, "CR-39 detector compared with Kodalpha film type (LR115) in terms of radon concentration", *Nucl. Instrum. Meth. Phys. Res. A*, 574(2) (2007) 289-291.

[7] P. Parajuli, D. Thapa and B.R. Shah, "Study of Radon Exhalation Rate in Soil Samples of Kathmandu Valley Using Passive Detector LR115", *Int. J. Chem. Phys. Sci.*, 4(4) (2015) 30-39.

[8] Kodalpha Radon Dosimeters and LR115 SSNTD specifications: Accessible online at: www.radon.at (2014).

[9] D. Thapa and B.R. Shah, "Residential Radon Concentrations in Kathmandu Valley Using Solid State Nuclear Track Detectors", Conf. Proc. Am. Assoc. Radon Sci. Technol. (AARST), South Carolina (2014).

[10] P.J. Gilvin, D.T. Bartlett, "Performance of a PADC radon dosemeter", *Int. J. Rad. Appl. Instrum. D*, 15(1-4) (1988) 571-576.

[11] J. Olszewski and K. Walczak, "Radon in houses of Kowary - Sudety Mountains, Poland", *Nukleonika*, 65 (2020) 149-152.

[12] J. Dehnert, A. Guhr and J. Engelhardt, "Improvement of a Radon Dosimetry System for Miners by Replacing Reference Dosimeters with Radonproof Boxes Containing Activated Carbon Cartridges", *Health Phys.*, 118(2) (2020) 117-128.

[13] Y. Tamakuma et al., "Passive-Type Radon Monitor Constructed Using a Small Container for Personal Dosimetry", *Int. J. Environ. Res. Public Health*, 17(16) (2020) 5660.

[14] S. Singh, M. Kumar and R. Kumar Mahajan, "The study of indoor radon in dwellings of Bathinda district, Punjab, India and its correlation with uranium and radon exhalation rate in soil", *Radiat. Measur.*, 39(5) (2005) 535-542.

[15] ICRP, Occupational Intakes of Radionuclides: Part 3, (Annals of the ICRP: NY, USA, 2017).

[16] S. Tokonami, "Some Thought on New Dose Conversion Factors for Radon Progeny Inhalation", *Jap. J. Health Phys.*, 53(4) (2018) 282-293.

[17] G. La Verde, "COVID-19 and the Additional Radiological Risk during the Lockdown Period in the Province of Naples City (South Italy)", Life, 12(2) (2022) 246.

[18] N.L. Nemerow, **"Environmental Engineering: Environmental Health and Safety for Municipal Infrastructure, Land Use and Planning, and Industry"**, 6th ed., John Wiley & Sons (2009).

[19] R.H. Clarke and W. Bines, Evolution of ICRP recommendations-1977, 1990, and 2007, Radiological Protection, Nuclear Energy Agency (2011).

[20] A.J Khan, "A study of indoor radon levels in Indian dwellings, influencing factors and lung cancer risks", *Radiat. Measur.*, 32(2) (2000) 87-92.

[21] D.J. Pawel and J.S. Puskin, "The U.S. Environmental Protection Agency's assessment of risks from indoor radon", *Health Phys.*, 87(1) (2004) 68-74.

[22] WHO, **"Handbook on Indoor Radon: A Public Health Perspective**", World Health Organization (Geneva, 2009).

[23] 90/143/Euratom: Commission Recommendation of 21 February 1990 on the protection of the public against indoor exposure to radon.

[24] R.W. Kleeb, S.A.M. Salah and E.S. Ali, "Calculation of Radon Gas Concentration in the Buildings of Samara University Using the Nuclear Track Detector CR-39", *NeuroQuantology*, 18(2) (2020) 82-87.

[25] A.A. Abojassim et al., "Estimation of the excess lifetime cancer risk from radon exposure in some buildings of Kufa Technical Institute, Iraq", *Nucl. Phys. Atom. Ener.*, 18(3) (2017) 276-286.

[26] Z.A. Hussein, A.H. Ismail and A.A. Battawy, "Indoor radon levels in apartments of Erbil city by using long and short term techniques", *Tikrit J. Pure Sci.*, 21(3) (2016) 150-154.

[27] B. Can et al., "Measurements of indoor radon concentration levels in Kilis, Osmaniye and Antakya, Turkey during spring season", *J. Radioanal. Nucl. Chem.*, 292 (2012) 1059-1063.

[28] T. Alkan and O. Karadeniz, "Indoor 222Rn Levels and Effectiv Dose Estimation of Academic Staff in izmir-Turkey", *Biomed. Environ. Sci.*, 27(4) (2014) 259-267.

[29] UNSCEAR, Effects of Ionizing Radiation; Volume II: Annex E Sources-to-Eff ects Assessment for Radon in Homes and Workplaces (UNSCEAR: New York, 2009).

Table (1) The track density, concentrations of radon, annual effective dose, LCC, ELCR, and PAEC

S. no.	S. Location	S. code	ρ Track/cm^2	CR_n Bq/m^3	AED mSv/y	LCC x10^{-9}	ELCR x10^{-3}	PAEC mWL
1	Bartilla	Brt1	327.272	75.757	3.610	155.959	13.899	8.189
2		Brt2	387.878	89.786	4.278	184.841	16.473	9.705
3		Brt3	303.030	70.145	3.342	144.407	12.869	7.582
4		Brt4	242.424	56.116	2.674	115.525	10.295	6.066
5	Bashiqa	Ba1	339.393	78.563	3.743	161.736	14.413	8.492
6		Ba2	400.000	92.592	4.412	190.617	16.987	10.009
7		Ba3	303.030	70.145	3.342	144.407	12.869	7.582
8		Ba4	412.121	95.398	4.546	196.393	17.502	10.312
9	Shikhan	Sh1	278.787	64.534	3.075	132.854	11.840	6.976
10		Sh2	290.909	67.340	3.209	138.631	12.354	7.279
11		Sh3	412.121	95.398	4.546	196.393	17.502	10.312
12		Sh4	315.151	72.951	3.476	150.183	13.384	7.886
13	Karales	Kar1	266.666	61.728	2.941	127.078	11.325	6.672
14		Kar2	412.121	95.398	4.546	196.393	17.502	10.312
15		Kar3	303.030	70.145	3.342	144.407	12.869	7.582
16		Kar4	290.909	67.340	3.209	138.631	12.354	7.279
17	Hamdaniya Somer Q.	So1	448.484	103.815	4.947	213.722	19.047	11.222
18		So2	242.424	56.116	2.674	115.525	10.295	6.066
19		So3	266.666	61.728	2.941	127.078	11.325	6.672
20		So4	375.757	86.980	4.145	179.065	15.958	9.402
21	Hamdaniya Ashur Q.	Ash1	315.151	72.951	3.476	150.183	13.384	7.886
22		Ash2	472.727	109.427	5.214	225.275	20.076	11.829
23		Ash3	230.303	53.310	2.540	109.749	9.780	5.762
24		Ash4	242.424	56.116	2.674	115.525	10.295	6.066
25	Hamdaniya Kalih Q.	Kal1	315.151	72.951	3.476	150.183	13.384	7.886
26		Kal2	424.242	98.204	4.679	202.170	18.017	10.615
27		Kal3	412.121	95.398	4.546	196.393	17.502	10.312
28		Kal4	387.878	89.786	4.278	184.841	16.473	9.705
29	Hamdaniya Rasin Q.	Ra1	327.272	75.757	3.610	155.959	13.899	8.189
30		Ra2	460.606	106.621	5.080	219.499	19.561	11.525
31		Ra3	242.424	56.116	2.674	115.525	10.295	6.066
32		Ra4	363.636	84.175	4.011	173.288	15.443	9.099
33	Hamdaniya Sinharib Q.	Sn1	521.212	120.651	5.749	248.380	22.135	13.042
34		Sn2	242.424	56.116	2.674	115.525	10.295	6.066
35		Sn3	230.303	53.310	2.540	109.749	9.780	5.762
36		Sn4	254.545	58.922	2.807	121.302	10.810	6.369
37		Sn5	266.666	61.728	2.941	127.078	11.325	6.672
38	Hamdaniya Akad Q.	Ak1	290.909	67.340	3.209	138.631	12.354	7.279
39		Ak2	278.787	64.534	3.075	132.854	11.840	6.976
40		Ak3	266.666	61.728	2.941	127.078	11.325	6.672
41		Ak4	290.909	67.340	3.209	138.631	12.354	7.279
42	H. Bakhded	Bk1	303.030	70.145	3.342	144.407	12.869	7.582
43		Bk2	218.181	50.505	2.406	103.973	9.266	5.459
44		Bk3	266.666	61.728	2.941	127.078	11.325	6.672
45		Bk4	242.424	56.116	2.674	115.525	10.295	6.066
Min	**218.181**	**50.5050**	**2.406**	**103.973**	**9.266**	**5.459**		
Max	**521.212**	**120.651**	**5.749**	**248.380**	**22.135**	**13.042**		
Mean	**321.885**	**72.827**	**3.470**	**149.926**	**13.361**	**7.872**		

Table (2) Comparison of the obtained results to those of other studies

No	Reference	location	C_{Rn} Bq.m^{-3}	AED mSv.y^{-1}
1	Present work	Iraq- Nineveh Plain region homes	72.82	3.470
2	(Azeez et al., 2018) ref. [4].	Iraq -Erbil-Ainkawa- the region of Kurdistan	84.30	2.124
3	(Kleeb et al., 2020) ref. [24].	Iraq- Samara University Buildings	41.4	0.4
4	(Abid et al., 2017) ref. [25].	Iraq- Kufa technical institute Buildings.	50	1.2
5	(Hussein et al., 2016) ref. [26].	Iraq-Erbil city- the region of Kurdistan	56.72	1.14
6	Bayram Can et al. 2011 ref. [27].	Turkey- Osmaniya	51	1.29
7	(Alkan and Karadeniz, 2014) ref. [28].	Turkey- Izmir	161	0.79

 ISSN (print) 1813-2065, (online) 2309-1673

IRAQI JOURNAL OF APPLIED PHYSICS
Vol. 19, No. 3B, September 2023, pp. 15-19

Malik H. Kheder

Department of Physics,
College of Education,
University of Al-Hamdaniya,
Ninawa Province, IRAQ

Radium and Uranium Concentrations in Some Fruits and Vegetables Cultivated in Nineveh Governorate, Iraq

Environmentally safe factors include clean soil and water that are free of pollution, particularly radioactive pollution, which has a significant impact on human health. Concentrations of uranium and radium were measured. in some fruit and vegetable samples collected from locally cultivated plants in the Nineveh governorate and chosen from among the people's most popular foods. Radium concentrations ranged from 0.085 to 0.366 Bq.Kg^{-1} and the range of uranium concentrations was 0.0935 to 0.4010 ppm with a mean value of 0.2327 ppm. The annual total effective equivalent dose from natural radionuclide ingestion ranged from 6.1988 to 41.883 Sv.y^{-1}, with a mean value of 18.602 Sv.y^{-1}. These values are much lower than the background dose from natural radionuclide ingestion in food, which is approximately 0.25-0.4 mSv per year. The samples' total radon concentrations were all found to be far below the ICRP's (International Committee on Radiological Protection) permitted level of 400 Bq.m^{-3} in fruits.

Keywords: Food safety; Radon concentration; Uranium content; CR-39 detector
Received: 11 March 2023; Revised: 24 March 2023; Accepted: 31 March 2023

1. Introduction

Humans consume leafy vegetables at a rate of 30 kg/year worldwide and about 35 kg/year in West Asia, while fruits and other vegetables are consumed at a rate of 150 kg/year worldwide and 140 kg/year in West Asia, implying that they have a high health impact on human life. Their radiation concentration must be measured. It is inevitable for humans to be subjected to ionizing radiation from both anthropogenic and natural sources; on average, we are exposed to 2.4 mSv of radiation annually from all-natural sources. The average annual dose from cosmic and terrestrial gamma radiation is 0.7 mSv. Natural radionuclide ingestion in food causes a portion of the background dose to be 0.25-0.4 mSv per year [1]. High energy cosmic ray particles striking air molecules in the atmosphere, In addition, there are ancient radioactive nuclides in the earth's crust, naturally occurring radioactive substances, are one of the primary causes of natural radiation [2]. Primordial radionuclides enter the soil through weathering of the earth's crust. It took the radionuclides in the soil by plants up through their roots and passed them on to humans when crops are consumed, resulting in internal exposure to ionizing radiation. Radionuclides consumed through food are major radiation pathways for health long-term considerations, significantly contributing to average doses of radiation to different human body parts and tissues [3]. Air, water, and soil are the sources of the elements that plants require. There are two ways for radionuclides in the environment to get to plants. The first method is via indirect uptake from the soil via roots. In polluted soil, food crops are grown, and the contaminated soil migrates to the roots and eventually the shoots. Activity is then used in relation to human nutrition. By mineral uptake, radioactive elements and nutrients are transported into plants where they concentrate in different areas of the plant and reach edible portions. Direct absorption via plant aerial parts is the second method. Several studies have looked into whether radioactivity can be found in plant organs [4]. Radon gas, which exists in the air, water, and soil, The most prevalent natural source of human radiation exposure [5]. The ICRP recommended natural limits for the public permissible value of 400 Bq.m^{-3} in fruits [6]. Soil characteristics, human activities, and geological formations related to radiation and radioactivity are all crucial variables in the increasing natural radiation background levels. By entering ecosystems and human food chains, natural radioactive elements are transmitted and cycled across different environmental compartments and through natural processes. Vegetables may be contaminated by uranium-series radionuclides both directly and indirectly. Using fertilizers causes an increase in uranium-series nuclides in vegetables [7]. Radium is a radioactive solid element that is naturally occurring and is found in sand, soil, rock, plants, water, and animals. Chemically, it is comparable to calcium and is absorbed from the soil by plants before entering the food chain for humans. Consuming radium results in anemia, bone cancer, and other health issues [8]. Because radon is generated via alpha decay of ^{226}Ra, radium-containing samples contribute to the level of radon in the environment. Radon and radium emit alpha particles, which bombard the marrow of bone to produce blood red cells and destroy the tissues. It

has been linked to cancer. This radiation of alpha damages the sensitive lungs, increasing the risk of lung cancer [9]. Long-term exposure of the populace to high radon concentrations results in pathological effects such altered respiratory function and the development of lung cancer [10]. Deposited uranium moves to plants from water and then into the food chain, and it poses a health risk to humans. Food is one of the human body's uranium sources, accounting for around 15% of total uranium. The primary uranium and radium deposition sites are the kidneys, liver, and bones [11, 12].

This study's objective was to quantify the radioactivity in samples of fruits and vegetables in order to assess the dangers to people's health. CR-39 detectors were employed for the measurements. Using the measurement track method, the detector measured alpha particles produced by radon.

2. Experimental Work

Seventeen samples of various fruits and vegetables grown in the Nineveh governorate of Iraq are in Fig. (1). The most popular foods among Iraqis were chosen as samples. To clean and eliminate any sand, all samples were first rinsed with water. They were then cut into mini pieces followed by drying in an electric oven at 100 °C for 3 hours to remove moisture before being measured. The components were ground into a fine powder and sieved using a 0.8 mm mesh sieve to achieve a homogenous particle size. The samples were coded to distinguish them. For 80 days, the samples were sealed in the plastic can (10 cm in length, 7 cm in diameter) shown in Fig. (2). The radon levels in samples was measured by a CR-39 detector using the registration technique for emitted alpha-particle tracks. CR-39 was cut into 1cm in width x1 cm in length, these detectors were placed in the cylinder cover at the closed top of a plastic can, four pieces were used and the average value was taken for each sample type to reduce the statistical errors. Each sample weights 70 gm, has a height of 3 cm, and is placed from the CR-39 detector at 7 cm. After 80 days the detectors chemically were etched with a 6.25 N of NaOH solution at 70°C fof about 8 hours. An optical microscope was used to count the tracks.

Concentration of the radon inside of the can air volume is determined by the equation [13].

$$C_{Rn} = \rho / KT \quad (1)$$

where ρ denotes the density of tracks which is the number of tracks per cm^2 in the microscope's view, T denotes the exposure time, The calibration factor of the CR-39 detector is K, and its value (0.05916 $Traks.cm^{-2}.day^{-1}/Bq.m^{-3}$) is determined using the formula [14].

$$K = \frac{1}{4} r \left(2cos\theta_c - \frac{r}{R_i}\right) \quad (2)$$

where θ_c is the CR-39 critical angle (35º), r is (3.5 cm) the radius for a sealed can, and R_i is the range of alpha particle in the air which for radon is (4.09 cm) calculated by [15].

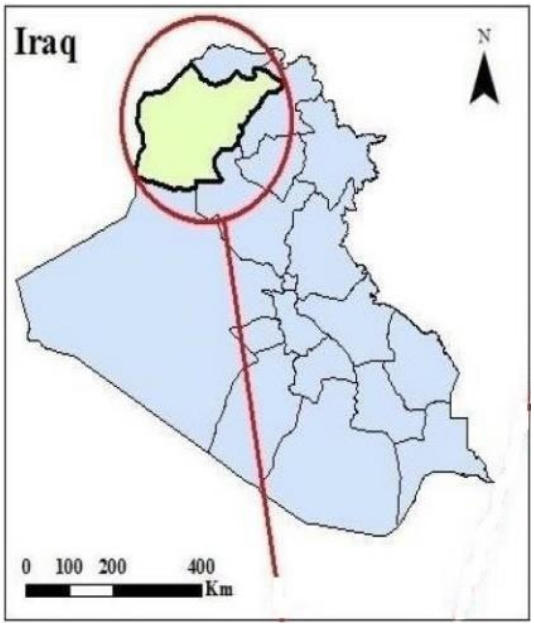

Fig. (1) Nineveh Governorate map

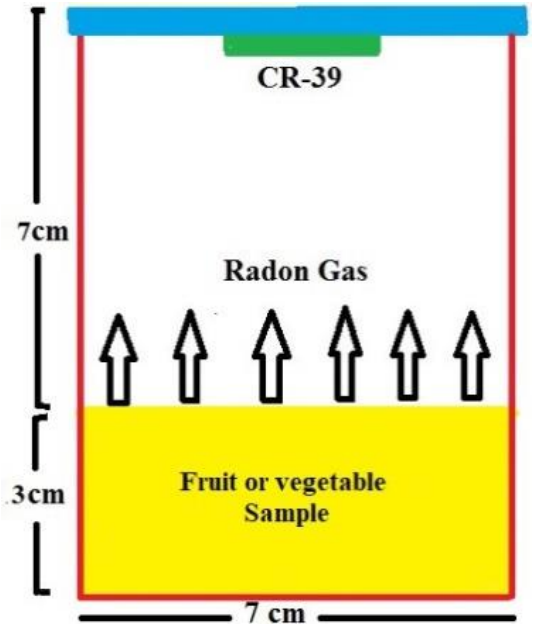

Fig. (2) Plastic can for radon measurement

The sample's radon concentrations were determined using the formula [16, 17].

$$C_s = \lambda_{Rn} C_{Rn} HT/l \quad (3)$$

where C_S: is the radon concentration in the sample ($Bq.m^{-3}$), C_{Rn}: is the radon concentration in the air space ($Bq.m^{-3}$), λ_{Rn} is the constant of radon decay ($0.1814\ day^{-1}$), H; is the air height space inside the plastic can (7 cm), T; is the exposure time (80 days), and *l* is the sample height in the can (3 cm).

Radium concentration C_{Ra} (Bq/kg) calculated using the equation [18].

$$C_{Ra}(Bq.Kg^{-1}) = \left(\frac{\rho}{KT_e}\right)\left(\frac{HA}{M}\right) \quad (4)$$

where A is the sealed container cross-section area in m^2, M is the sample mass in kilograms, H is the

 ISSN (print) 1813-2065, (online) 2309-1673

distance in meters between the sample surface and the detector, and According to the relation, T_e stands for the effective exposure period during the day.

$$T_e = \left[T - \lambda_{Rn}^{-1}\left(1 - e^{-\lambda_{Rn}T}\right)\right] \quad (5)$$

T being the exposure time and λ_{Rn} is the radon decay constant.

The sample's radon activity A_{Rn} is determined from the sample's radon concentration C_s by the equation.

$$A_{Rn} = C_s V \quad (6)$$

where the sample volume V is ($V = \pi r^2 l$) = 115.39 X 10^{-6} m^3, the plastic can radius r = 0.035 m, l = 0.03 m is the height of the sample. Therefore:

$$\lambda_{Rn} N_{Rn} = A_{Rn} \quad (7)$$

$$A_U = A_{Rn} \quad (8)$$

The number of uranium atoms present in a sample N_U was calculated by the secular equilibrium equation between uranium and radon activity.

$$\lambda_U N_U = \lambda_{Rn} N_{Rn} \quad (9)$$

The uranium constant decay is λ_U = (4.883 X 10^{-18} sec^{-1}). Uranium weight in the samples was determined by the uranium atom number N_U using the relation.

$$W_U = N_U a_U / N_{avo.} \quad (10)$$

where a_U is the uranium mass of ^{238}U, $N_{avo.}$= (6.02 X 10^{23} atom/Mol) is Avogadro number, W_U in microgram units (µg). Concentration of uranium is then determined.

$$C_U = W_U / Ws \quad (11)$$

where C_U is uranium concentration in units (ppm) part per a million, where the mass of the sample is Ws = 70 grams.

The uranium activity concentration in ($Bq.Kg^{-1}$) units will be.

$$Ac_U = \lambda_U N_{avo.} [a_U]^{-1} C_U \quad (12)$$

where C_U in (g/kg) units are required (where 1ppm=10^{-6}g/g = 10^{-3}g/Kg) [19].

The effective dose from food consumption is useful for assessing the likelihood of various radionuclides originating from diverse radioactive sources. The radiation ingested doses are calculated by multiplying the radionuclide activity concentration in the food (Bq. kg^{-1}) by the food consumed mass over a specific period (kg/year) and applying the factor (Sv/Bq) of dose conversion for each radionuclide [20].

$$AED = \sum A_f I_f F_{DCF} \quad (13)$$

The annual effective equivalent dose (AED) from radionuclide ingestion in (Sv/y), Af is the activity concentration of radionuclide in the sample (Bq/kg), If is the annual food consumed over a year for leafy vegetables is 30 in West Asia and 35 in the world, and fruit with other Vegetables is 140 in West Asia and 150 in the world, and F_{DCF} is the internal conversion dose factor (Sv/Bq) by radionuclide ingestion. The radionuclide ingestion dose was calculated for the entire body use of dosage conversion factors of 0.045 Sv/Bq for uranium and 0.28 Sv/Bq for radium [21].

3. Results and Discussion

The findings from the samples of fruits and vegetables are shown in table (1).

Table (1) Shows the CR-39 track density, radon concentrations, radium activity concentrations, uranium concentrations, uranium activity concentrations, and the total annual equivalent effective dose

No	Sample		ρ track /cm^2	CRn Bq/m^3	CRa Bq/Kg
1.	Leafy Vegetables	Basil	266.6	56.327	0.23263
2.		Celery	284.8	60.173	0.24851
3.		Chard	267	56.412	0.23298
4.		Rashad	420	88.738	0.36649
5.		Leek	327.3	69.152	0.28560
6.	Fruit / Vegetables	Pepper	186	39.298	0.16230
7.		Lemon	104	21.973	0.09075
8.		Potato	171	36.129	0.14921
9.		Orange	218.2	46.101	0.19040
10.		Okra	181.8	38.411	0.15863
11.		Eggplant	318	67.187	0.27748
12.		Tangerine	108	22.818	0.09424
13.		Garlic	272	57.468	0.23734
14.		Onion	211	44.580	0.18411
15.		Olive	98	20.705	0.08551
16.		Radish	386	81.555	0.33682
17.		Cucumber	325	68.666	0.28359
Min			98	20.705	0.08551
Max			420	88.738	0.36649
Mean			243.8	51.506	0.21278

No	Sample		CU (ppm)	CU Bq/Kg	Total AED µSv/y
1.	Leafy Vegetables	Basil	0.2545	3.1442	6.1988
2.		Celery	0.2719	3.3589	6.6220
3.		Chard	0.2549	3.1489	6.2081
4.		Rashad	0.4010	4.9534	9.7656
5.		Leek	0.3125	3.8601	7.6102
6.	Fruit / Vegetables	Pepper	0.1776	2.1936	20.182
7.		Lemon	0.0993	1.2265	11.284
8.		Potato	0.1632	2.0167	18.554
9.		Orange	0.2083	2.5734	23.676
10.		Okra	0.1735	2.1441	19.726
11.		Eggplant	0.3036	3.7504	34.505
12.		Tangerine	0.1031	1.2737	11.718
13.		Garlic	0.2597	3.2079	29.514
14.		Onion	0.2014	2.4885	22.895
15.		Olive	0.0935	1.1558	10.633
16.		Radish	0.3685	4.5524	41.883
17.		Cucumber	0.3103	3.8330	35.264
Min			0.0935	1.1558	6.1988
Max			0.4010	4.9534	41.883
Mean			0.2327	2.8751	18.602

The findings revealed that the range of the radon gas concentration was 20.705 to 88.738 Bq/m^3 with the mean value 51.506 Bq/m^3, the uranium concentration ranged from 0.0935 to 0.4010 ppm with the mean value of 0.2327 ppm, the uranium activity concentration varied from 1.1558 to 4.9534 Bq/Kg with the mean value of 2.875 Bq/Kg, and the concentration of radium varied from 0.08551to 0.36649 Bq/Kg with the mean value 0.2127 Bq/Kg as shown in Fig. (3).

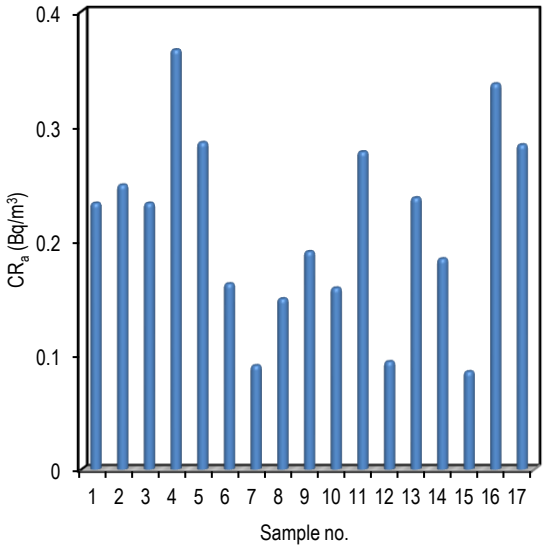

Fig. (3) Variation of radium concentrations in fruit and vegetable samples

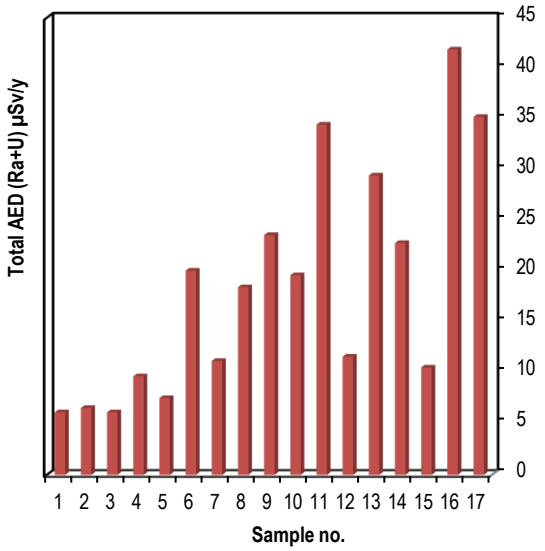

Fig. (4) Variation of total annual effective dose in fruit and vegetable samples

These concentrations differed from one sample to the next depending on the type of sample, with the low concentration in sample no. 15 being olive and the high concentration in sample no. 4 being Rashad, these are normal concentrations even though it absorb heavy metals from the soil where animal waste and fertilizers are used. Fertilizers are necessary for agriculture because they provide nutrients to farming fields. Radionuclides and some of their daughter decay products are used to increase agricultural production. Agricultural fields and the ecosystem are contaminated by radionuclide-rich phosphate fertilizers during cultivation [22]. Fertilizers are considered a type of technologically enhanced natural radiation that raises the amount of uranium in the environment [23]. Phosphate rock fertilizers contain naturally occurring radioactive nuclides from the thorium and uranium decay series. Because of the uptake of these fertilizers, these radioactive nuclides will end up in fruits and vegetables, and they pose radiological hazards to human health by consuming agricultural produce. The obtained results are comparable with those of similar papers [24-26] performed on other Iraqi vegetables. The total annual effective dose equivalent, which is the sum of uranium and radium annual effective doses, ranges from 6.1988 to 41.883 Sv/y, with a mean value of 18.602 Sv/y as shown in Figure 4. Whereas the lower value was in sample no.1 which represents the basil sample, and the higher value was in sample no.16 which represents the radish sample, the results show that different samples have a higher concentration of radionuclides because the annual effective dose depends on the annual food consumed over a year, which is for leafy vegetables is 30 in West Asia and 35 in the world, and fruit with the other vegetables is 140 in West Asia and 150 in the world.

4. Conclusions

Radium, radon, and uranium concentrations were measured in samples of fruits and vegetables chosen among the most popular food of people, collected from local cultivated in Nineveh governorate. An agricultural area consists of fertile soil and fields where fertilizers and animal waste are used, it is dependent on irrigation. Aside from the rain, phosphate rock-derived fertilizers contain naturally occurring radioactive nuclides from the thorium and uranium decay series. As a result of the fertilizer's uptake, these radioactive nuclides will wind up in the crop.

All radon concentration values obtained for the samples were found to be significantly low than 400 Bq.m^{-3} the permissible value in fruits recommended by (ICRP). The results were compared to other works; the comparison revealed that the obtained results are comparable with those of similar papers performed on other Iraqi vegetables. The total annual equivalent effective dose from natural radionuclides ingestion was measured and found to be much lower than the background dose resulting from the ingestion of naturally occurring radionuclides in food, which is approximately 0.25-0.4 mSv per year. The fruits and vegetables under study pose no significant risk due to the presence of these radionuclides, and they are considered radiologically safe for human consumption.

References

[1] UNSCEAR (United Nations Scientific Committee on the Effects of Atomic Radiation), “Sources and effects of ionizing radiation. Report to the General Assembly with Scientific Annexes, 1. Annex B: Exposures from natural radiation sources”, New York (2000).
[2] ICRP (International Commission on Radiological Protection), “The 2007

 ISSN (print) 1813-2065, (online) 2309-1673

Recommendations of the International Commission on Radiological Protection", Annals of ICRP Publication 103 (2007).
[3] N. Jibiri, I. Farai and S. Alausa, "Estimation of annual effective dose due to natural radioactive elements in ingestion of foodstuffs in tin mining area of Jos-Plateau, Nigeria", *J. Env. Radioact.*, 94 (2007) 31.
[4] D. Robinson, **"Food Biochemistry and Nutritional Value"**, Longman Scientific and Technical Pub. (NY, 1987).
[5] M. Eisenbud and T. Gesell, **"Environmental Radioactivity from natural, industrial and military sources: from natural, industrial and military sources"**, 4th ed., Elsevier (1997).
[6] ICRP (International Commission on Radiological Protection), "Committee 4, Radionuclide Release Into the Environment: Assessment of Doses to Man", a Report of Committee 4 of the International Commission on Radiological Protection (1979). (No. 29).
[7] E. Ekdal, T. Karali and M. Sac, "^{210}Po and ^{210}Pb in soils and vegetables in Kucuk Menderes basin of Turkey", *Radiat. Measur.*, 41 (2006) 72.
[8] A. Mahur et al., "Measurement of effective radium content of sand samples collected from Chhatrapur beach, Orissa, India using track etch technique", *Radiat. Measur.*, 43 (2008) S520.
[9] N. Ding, J. Li and L. Sun, "Molecular Mechanisms and Treatment of Radiation-Induced Lung Fibrosis", *Current Drug Targets*, 14 (2013) 1247.
[10] BEIR, VI., "Report of the Committee on the Biological Effects of Ionizing Radiation: The health effects of exposure to indoor radon", National Research Council, (Washington, DC. (1999). The National Academies Press).
[11] C. Cothren and W. Lappenbusch, "Occurrence of Uranium in Drinking Water in the U.S.", *Health Phys.*, 45 (1983) 89.
[12] ATSDR. Agency for toxic substances and disease registry, "Toxicological profile for radium", (Atlanta, Georgia: US Department of health and human services(1990)).
[13] H. Azeez et al., "Radon Concentration Measurement in Ainkawa Region Using Solid State Nuclear Track Detector", *Iraqi J. Sci.*, 59(1C) (2018) 482-488.
[14] M. Kheder, H. Azeez and F. Al-Jomaily, "Alpha Emitters Radioactivity Concentrations in Some Cosmetics Used in Iraq Using LR-115 Detector", *Eureka: Phys. Eng.*, 2 (2020) 65.
[15] M. Mansy et al., "Theoretical calculation of SSNTD response for radon measurements and optimum diffusion chambers dimensions", *Radiat. Measur.*, 41 (2006) 222.
[16] G. Somogyi, "Track detection methods of radium measurements No. ATOMKI-E-25", Magyar Tudomanyos Akademia (1986).
[17] M. Kheder et al., "Radioactivity concentrations in barley and wheat crops in Nineveh plain region in Iraq", *Int. J. Nucl. Ener. Sci. Technol.*, 14 (2020) 50.
[18] M. Khan, D. Srivastava and A. Azam, "Study of radium content and radon exhalation rates in soil samples of northern India", *Env. Earth Sci.*, 67 (2012) 1363.
[19] M. Kheder et al., "Radon and uranium concentration in ground water of nineveh plain region in Iraq", *J. Phys.: Conf. Ser.*, 1234 (2019) 012033.
[20] C. Kansaana et al., "Measurement of Activity Concentrations of ^{226}Ra, ^{232}Th, ^{40}K and ^{137}Cs in Some Common Spices Consumed by Inhabitants in Accra Metropolis, Ghana", *Int J. Food Sci. Nutr. Diet*, 2 (2013) 75.
[21] S. Giri et al., "Estimation of annual effective dose due to ingestion of natural radionuclides in foodstuffs and water at a proposed uranium mining site in India", *Int. J. Rad. Biol.*, 89 (2013) 1071.
[22] IAEA., "Measurement of radionuclides in food and the environment, A Guidebook", Vienna: Technical Reports Series 229 (1989).
[23] D. Ghosh et al., "Measurement of natural radioactivity in chemical fertilizer and agricultural soil: evidence of high alpha activity", *J. Env. Geochem. Health*, 30 (2008) 79.
[24] A. Hashim, and L. Najam, "Radium and Uranium Concentrations Measurements in Vegetables Samples of Iraq", *Detection*, 3 (2015) 21.
[25] H. Hady, A. Abojassim and Z. Mohammed, "Study of Radon Levels in Fruits Samples using LR-115 Type II Detector", *J. Env. Sci. Technol.*, 9 (2016) 446.
[26] S. Amin, A. Ayoub and A. Jassim, "Radioactivity Levels in Some Vegetables and Herbs", *Eng. Technol. J.*, 36(C2) (2018) 174-178.

IRAQI JOURNAL OF APPLIED PHYSICS
Vol. 19, No. 3B, September 2023, pp. 20-24

Determining the Optimal Direction and Angle of Incidence of Solar Radiation to Obtain Electrical Energy from Solar Panels in the Nineveh Plain Region

Ban A. Bader
Rajaa A. Basheer
Malik H. Kheder
Hanaa N. Azeez

Department of Physics, College of Education, University of Al-Hamdaniya, Ninawa Province, IRAQ

The goal of this study is to discover the nature of the climatic characteristics in the study region, which has excellent climatic potential, and to emphasize them. It also seeks access to the elements impacting it in order to direct the solar panels to get the most advantage. The results show that installing solar panels in the study region is best done facing south. The direction in which solar cells are placed is also determined by the angle of incidence of solar radiation; as a result, they should be installed at angles that are consistent with the monthly distribution. Cloud cover also affects the number of hours of brightness while using solar energy. The study region has limited solar energy usage, but solar panels can be utilized there to provide electricity for a variety of purposes, including street lights, security cameras, charging gadgets, and other uses.

Keywords: Solar radiation; Solar cells; Solar energy; Solar panels
Received: 11 March 2023; Revised: 24 March 2023; Accepted: 31 March 2023

1. Introduction

Energy production and consumption serve as a barometer for the degree of civilized sophistication of a country since they reveal how far the economy has advanced in terms of both its general direction and its overall scope. Recently, man has come to the realization that any increase in production and consumption may result in an increase in cost within the environmental economic system. As a result, man has sought to find renewable energy that does not burden his nature's ecological system, and as a result, a trend toward producing electricity from solar energy has emerged. sun cells either directly or indirectly using techniques like the thermoelectric method and the thermal ion conversion method [1, 2]. As a result, the concept of creating a solar cell emerged more than 150 years ago, and it was discovered that, in accordance with the photovoltage phenomenon, solar light could be transformed into a potential difference. In 1839, Edmund Becquerel made the discovery and observed that the incident light affects the voltage between electrodes submerged in an electrolyte solution [3].

In the past, solar cells could only be used to provide sparsely populated areas with energy. These cells are already being used in more and more applications, and usage is predicted to rise, particularly if prices remain low and take the anticipated form in the near future [4]. Researchers have also been compelled to lower production costs as a result of the rise in the cost of making silicon-based solar cells. Despite being abundant in nature, this material is quite expensive to turn into solar cells, which is why there is currently a lot of research being done to lower the costs of producing electricity from solar radiation [5]. A study was conducted on the theoretical underpinnings of solar radiation, its influences, its geographical distribution in the Anbar Governorate, as well as its uses and potential applications in the creation of alternative energy sources [6]. On the Syrian coast during the four summer months, the ideal angle of inclination of solar panels was discovered after studying the influence of the angle of inclination of solar panels on the amount of water flowing per day to a water pump powered by solar energy. According to the study, there was no effect on the curve of the relationship between the intensity of solar radiation and the flow of the pump throughout the day when the inclination angle of the solar panels was changed from 25° to 35.5°. The solar energy falling on the solar panels per day is decreasing, which had the consequence of reducing the hydraulic capacity of the pump. Hence, less water flows each day [7]. After finishing an analysis of solar radiation and its major affecting elements, it was determined how much electrical energy (current and voltage) was produced by solar radiation in Iraq. It also emphasized the importance of investing in Iraq's potential for using solar energy to provide electricity [8]. A study also revealed that there are solar radiation potentials that might be used to produce renewable energy. As well as researching how each type of solar radiation is influenced by the climate. The study concentrated on how to use solar energy to make

 ISSN (print) 1813-2065, (online) 2309-1673 PRINTED IN IRAQ

investments in renewable energy sources [9]. Another study demonstrated the impact of clouds and rain by using a cell with a 100 watt efficiency that can produce 5.5 amperes under normal circumstances, but it was discovered that during the presence of rain, this panel's production decreased to 0.8 amperes, meaning that its efficiency decreased by 85.5% of its original efficiency, or the panel's efficiency is 14.5% of watts. In other words, clouds and rain are to blame for this weakness in efficiency [10]. Another study examined the parameters influencing solar radiation, their seasonal and geographic distribution, and the existing applications of renewable energy [11].

The most significant climatic factors in Iraq that can be used to produce renewable energy in the future and implement it as a replacement for fossil traditional energy were the subject of a study [12]. A study using the Arab countries as a case study examined the significance of utilizing renewable energy sources and their preference over fossil fuels for producing power and safeguarding the environment. The study came to a number of conclusions, including: The majority of the energy used to produce electricity in Arab nations comes from fossil fuels, but due to their near total reliance on them, the amount of carbon dioxide that these nations released into the atmosphere increased, reaching 1678.2 million tons in 2017. As a result, it is imperative that these nations fully utilize their abundant renewable energy resources to produce electricity as a viable and environmentally friendly alternative to fossil fuels [13]. In addition to choosing the best locations for solar power plant construction in the Dohuk Governorate, it dealt with the research of solar radiation and the natural and human variables impacting it [14]. In the Assiut Governorate of Upper Egypt, which experiences high temperatures, a study was done to conduct a practical and theoretical investigation of the influence of ambient air temperatures and effect of dust on the efficiency of solar cells.

Temperatures significantly affect diminishing the generated capacity, which is one of the study's useful conclusions. It was discovered that dust had a significant impact on lowering the electrical capacity produced by solar cells when considering the factor of deposition and accumulation of dirt and dust on the performance of solar cells during the time that saw notable activity of dust-laden winds throughout the year. Thus, it is necessary to frequently clean solar cells every four days, especially after a dust storm [15].

2. Experimental Work

The solar system and its influencing factors

- Solar panels: A part of the solar energy system are solar cells. Due to its compact design, the solar cell converts sunlight into direct current electrical energy, which is the same energy that is stored in the battery, as it comes into contact with it. The solar cell is referred to as a photovoltaic cell since the conversion process relies on the photoelectric effect.

- Solar energy batteries: As the public electric grid serves as a reliable source of electricity when the sun isn't shining, solar systems that are connected to it do not need to employ solar energy batteries. Batteries are needed for solar systems that are not connected to the national grid in order to store energy when the sun is not shining as it should. This is especially true for devices like solar-powered watches that should never have their power switched off. Instead, this kind of application necessitates the use of batteries with a very big capacity, enough to last for several days without exposure to sunlight.

- Charge Controller: As its name suggests, the solar charging regulator, also known as the solar rectifier, serves an important purpose. It controls how batteries are charged. By cutting off the current from the batteries if they reach a predetermined amount of charge that falls short of 100%, it prevents the batteries from being overcharged. It keeps the batteries' safety intact in this way. Also, the solar rectifier or charge controller modifies the energy from the solar panels so that the batteries can accept the proper voltage and current. Instead, some types force solar panels to operate at their full capacity, which enhances their performance.

- Solar Inverter: The necessity to use these cells to produce highly variable electricity that can power big electrical and electronic devices in households or workplaces gives this stage its importance. In this case, we must employ equipment known as inverters, which change direct current whether it be 12 volts, 24 volts, or any other value into a high variable current (110 V AC or 220 V AC) to power heavy equipment and gadgets that run on variable current [16].

The final step, without which the solar panels would be of no real use, is the conversion of the constant voltage, whether it be 12 volts or 24 volts, into a variable voltage AC220 V, which can power devices like a television, a small refrigerator, or a personal computer inside. This is the same device that is used in cars to connect to the car lighter. This device's power is expressed in watts, which represent the maximum load it can support.

System setup: To charge portable electronics and simple purposes, a straightforward solar energy system has been put up. Three solar panels, a DC to AC inverter, two batteries, and a charging regulator make up the apparatus. PWM as in Fig. (1).

3. Results and discussion

As a test was conducted in the middle of the day at 12:00 pm because the solar beam falls perpendicular to the ground, several directions were tested practically to obtain the best productivity of the solar panels. The inclination of the panels was fixed at an angle of 450 as a reference angle for all four directions. Obtained the readings depicted in table (1), which revealed that the direction that produces

the largest capacity of solar power is the south, making it the optimum direction for solar panels (31.32W). For the remainder of the investigation, the south direction will serve as a guide.

(a)

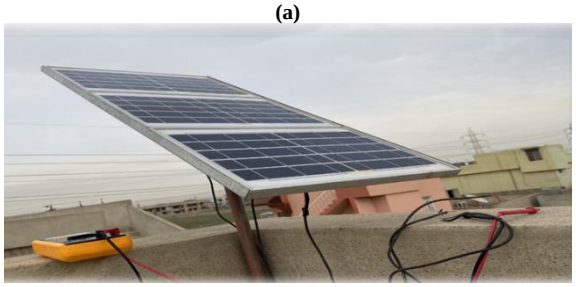

(b)

Fig. (1) System configuration (a) charging regulator, and (b) solar panels

Table (1) Choosing the best direction

Direction	North (0°)	East (90°)	South (180°)	West (270°)
I_{in}	0.65	0.95	1.76	0.8
V_{in}	15.3	17.3	17.8	16.9
P_{in}	9.945	16.435	31.32	13.52

In order to find the ideal angle of inclination, different angles towards the south were evaluated when the study first started in October, as shown in table (2) and Fig. (2), from those, we discovered that for the month of October, as specified in the direction of the south, the best angle of inclination for the solar panels is the angle (45^0), where we acquired the largest capacity of (31.862W), In the month of November, the best angle of inclination of the solar panels mentioned in the direction of the south is the angle (60^0), where we obtained the highest capacity of (32.578W), and in the month of December, we discovered that the same is true, with the best angle of inclination mentioned in the direction of the south being the angle (60^0), where we obtained the highest capacity of (32.578W) (26.5518W). The best angle of inclination specified in the south (60^0, where we obtained the largest capacity of) during the month of January was (27.396W). In February, the angle (45^0) is the best one specified in the direction of the south, where the largest capacity of (32.199W). The angle (45^0) in March month, where the largest capacity of 31.222W is mentioned, is in the direction of the south.

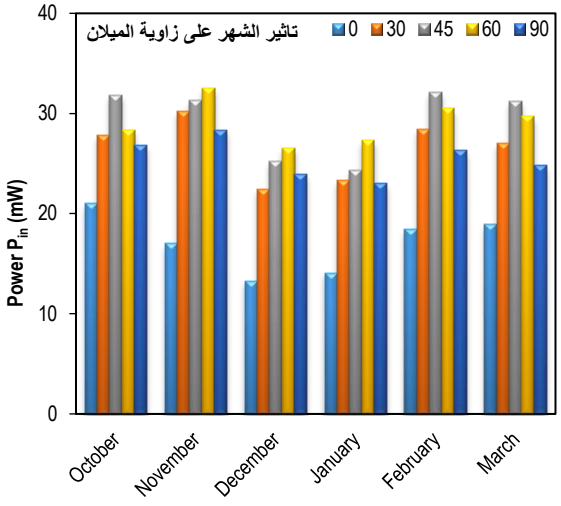

Fig. (2) Variation of the power with Angle for solar panels through the months

Table (2) Standard angle of inclination in the months

Month		Angle				
		0^0	30^0	45^0	60^0	90^0
October	I_{in}	1.2	1.62	1.79	1.65	1.56
	V_{in}	17.5	17.2	17.8	17.2	17.2
	P_{in}	21	27.864	31.862	28.38	26.832
November	I_{in}	1.0	1.74	1.76	1.82	1.64
	V_{in}	17	17.4	17.8	17.9	17.3
	P_{in}	17	30.276	31.328	32.578	28.372
December	I_{in}	0.78	1.27	1.42	1.49	1.35
	V_{in}	17.15	17.68	17.79	17.82	17.75
	P_{in}	13.377	22.4536	25.2618	26.5518	23.962
January	I_{in}	0.82	1.34	1.38	1.54	1.30
	V_{in}	17.2	17.45	17.65	17.79	17.7
	P_{in}	14.104	23.383	24.357	27.396	23.01
February	I_{in}	1.07	1.63	1.81	1.73	1.51
	V_{in}	17.25	17.46	17.79	17.67	17.42
	P_{in}	18.457	28.459	32.199	30.569	26.304
March	I_{in}	1.11	1.55	1.76	1.69	1.43
	V_{in}	17.1	17.48	17.74	17.61	17.39
	P_{in}	18.981	27.094	31.222	29.760	24.867

Two days in December were used for this test, one sunny and the other entirely cloudy. The results are displayed in tables (3) and (4) and Fig. (3). Using the above-mentioned tables as a guide. Figure (3) illustrates the difference in capacity production between a sunny day and a wholly cloudy day. The number of hours is shown on the x-axis, and the capacity created is shown on the y-axis. When installing solar panels, cloudy days or the percentage of the sky that is covered by clouds, as depicted in the included image, are among the most crucial considerations because this weather phenomenon restricts or reduces the amounts of solar radiation that can reach these solar cells. As a result, the more cloud coverage there is, the less sunlight will reach the solar cells. The likelihood of investing in the solar radiation required to produce usable renewable electrical energy has decreased as a result of the sky becoming clouded.

 ISSN (print) 1813-2065, (online) 2309-1673

Table (3) Voltages and currents for a sunny day

Hour	I_{in}	V_{in}	P_{in}
7:00	0.23	17.62	4.05
8:00	0.57	17.66	10.06
9:00	1.13	17.67	19.96
10:00	1.38	17.70	24.4
11:00	1.51	17.65	26.65
12:00	1.68	17.46	29.33
13:00	1.56	17.37	27.09
14:00	1.31	17.27	22.62
15:00	0.85	17.24	14.65
16:00	0.29	16.83	4.88

Table (4) Voltages and currents for a completely cloudy day

Hour	I_{in}	V_{in}	P_{in}
7:00	0.05	14.90	0.745
8:00	0.07	16.40	1.148
9:00	0.09	16.75	1.507
10:00	0.25	17.51	4.377
11:00	0.45	17.74	7.983
12:00	0.79	17.82	14.077
13:00	0.60	17.50	10.5
14:00	0.48	17.44	8.371
15:00	0.15	16.73	2.509
16:00	0.10	16.38	1.638

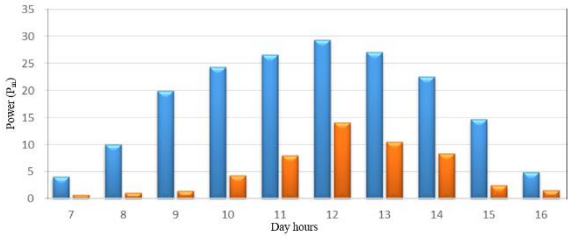

Fig. (3) The difference in power capacity production between a sunny day and a total cloudy day

The impact of shade on solar panel performance is highlighted since this impact can clearly reduce the performance of the panels, as shown in the images below. Since solar panels depend on light from the sun to function, any shading over them will serve to lessen the amount of solar radiation that strikes them, which will result in a large and noticeable decrease in the value of the electrical power that comes out of the panel as a result.

4. Conclusions

The most significant finding from the study of this project is that solar energy initially produces less electricity than anticipated. However, as time goes on and the solar system is used, it will become clearer to what extent it is important and of great benefit. With enough knowledge of how the system operates and its generating capacity, solar energy can be considered a reliable source of energy for the majority of the time. Another key finding is that the solar system's effectiveness is significantly influenced by the atmosphere and its position.

- The best direction for solar panel installation in the research region is toward the south.
- The solar cells should be positioned within angles that are suitable with the monthly distribution because the angle of incidence of solar radiation determines the direction in which they should be put.
- The amount of solar radiation coming on cloudy days is lower than on sunny days with a clear sky and a bright sun because clouds reduce the number of hours of brightness when it comes to using solar energy.
- The location of the solar panel installation must be far from any obstructions to the solar cell's ability to receive solar radiation.
- One of the biggest environmental risks associated with solar energy is dust, which builds up on the glass surface of the solar panels and blocks the light from reaching the cells inside. This requires cleaning the solar panels every month to prevent a reduction in the amount of energy they produce.
- According to the data, there are climatic factors that can be used in conjunction with solar cells to generate and make up for a lack of electrical energy. There are also other factors and potentials, but they have not yet been fully utilized, and despite these factors, there are only a few solar energy applications in the study area.
- In the study region, solar energy can be employed and benefited from in many different industries and activities, such as (electric power generation, street lighting, security cameras, charging gadgets, and other purposes).

References

[1] M. Bengtsson et al., "Transforming systems of consumption and production for achieving the sustainable development goals: moving beyond efficiency", *Sustain Sci.*, 13(6) (2018) 1533-1547.

[2] S.O. Oyedepo, "Energy and sustainable development in Nigeria: the way forward", *Ener. Sustain. Soc.*, 2(15) (2012).

[3] R.J. Komp, "Practical photovoltaics: electricity from solar cells", *Ann. Arbor: AATEC Pub.*, (1995).

[4] A. Shah et al., "Photovoltaic technology: the case for thin-film solar cells", *Science*, 285(5428) (1999) 692-698.

[5] A. Shah et al., "Towards very low-cost mass production of thin-film silicon photovoltaic (PV) solar modules on glass", *Thin Solid Films*, 502(1-2) (2006) 292-299.

[6] M. Tadros, M.A.M. Mustafa and M. Abdel-Wahab, "Estimation of the global horizontal solar radiation in Iraq", *Int. J. Emerg. Technol. Adv. Eng.*, 4(8) (2014) 587-605.

[7] A.A. Kazem, M.T. Chaichan and H.A. Kazem, "Dust effect on photovoltaic utilization in Iraq", *Renew. Sustain. Ener. Rev.*, 37 (2014) 734-749.

[8] H.A.H. Alshamri, "Optimal sizing of hybrid renewable systems to improve electricity supply reliability in Iraqi domestic dwellings", Diss., University of Leeds (2019).

[9] H.H. Al-Kayiem and S.T. Mohammad, "Potential of renewable energy resources with an emphasis on solar power in Iraq: An outlook", *Resources*, 8(1) (2019) 42.
[10] M.T. Chaichan, B.A. Mohammed and H.A. Kazem, "Effect of pollution and cleaning on photovoltaic performance based on experimental study", *Int. J. Sci. Eng. Res.*, 6(4) (2015) 594-601.
[11] B.E. Ssekulima et al., "Wind speed and solar irradiance forecasting techniques for enhanced renewable energy integration with the grid: a review", *IET Renew. Power Gen.*, 10(7) (2016) 885-989.
[12] M. Asif and T. Muneer, "Energy supply, its demand and security issues for developed and emerging economies", *Renew. Sustain. Ener. Rev.*, 11(7) (2007) 1388-1413.
[13] A. Qazi et al., "Towards sustainable energy: a systematic review of renewable energy sources, technologies, and public opinions", *IEEE Access*, 7 (2019) 63837-63851.
[14] G.A.F. Ibrahim, K.W. Mahmood and M.M. Mahmud, "Multi Criteria Decision Analysis Technique for Solar Power Sites Selection in Duhok Governorate–Iraq", *Preprints*, (2021).
[15] Hassaan, A. Sherif M., B. A. El Samhay, and C. Haggag, "Performance Study of Monocrystalline, Polycrystalline, and Thin-film Solar PV Modules in the Egyptian Environment."
[16] Chauhan, and B. S. Rajpurohit, "DC distribution system for energy efficient buildings" Eighteenth National Power Systems Conference (NPSC). IEEE, (2014).

 ISSN (print) 1813-2065, (online) 2309-1673

IRAQI JOURNAL OF APPLIED PHYSICS
Vol. 19, No. 3B, September 2023, pp. 25-29

Tharaa J. Polus[1,4]
Thoalfiqar A. Zaker[2,4]
Hala N. Mohammed[3]

1 Directorate of Education in Al-Hamdaniya, Nineveh, 41006, IRAQ
2 Department of Physics, College of Education, University of Al-Hamdaniya, Nineveh, IRAQ
3 Department of Physics, College of Education for Pure Sciences, Mosul University, Mosul, IRAQ
4 Laser and Spectroscopy Department, Laser and Photonics Research Center, University of Al-Hamdaniya, Nineveh, IRAQ

Effect of Laser Frequency on Nonlinear Optical Properties of ZnO Thin Films

Zinc oxide thin films' nonlinear optical characteristics of thickness of 425 nm were studied throughout the research. Using a laser diode with a wavelength of 650 nm and a low laser power of 2 mW, the well-known Z-scan technique was employed. The measurements were made at various frequencies between 1 kHz and 100 kHz. The results indicate a positive sign for two photon absorption coefficient at both the low and high frequency range. The Kerr coefficient starts with a positive sign at low frequency range that switch to a negative sign when the frequency range gets higher.

Keywords: Z-scan technique; Zinc oxide; Thin films; Nonlinear absorption
Received: 11 March 2023; Revised: 24 March 2023; Accepted: 31 March 2023

1. Introduction

Due to its significance in numerous scientific applications, the study of the nonlinear optical (NLO) response has garnered a lot of attention during the past few decades [1-3]. NLO phenomena occur when the light with high intensity travel through medium [4]. When high-intensity lasers interact with a transparent material, a collateral laser-induced damages (LIDs) can easily occurs. By using materials that have high damage thresholds one can avoid the damage [5-7]. Pulse lasers allow this response to occur within low laser energies. In the process of light interacting with matter, pulse-based laser operation instead of continuous (CW) generates significant control (time-space) for nonlinear optical response. The properties of the pulse laser, such as frequency [8], polarization [9], repetition rate [10], and wavelength [11] showed a modification of material property. The impact of laser pulse frequency and polarization on NLO characteristics has received significant attention from the scientific community [12,13]. In which the effect of varying laser frequency on NLO depends on molecular property. All materials display defocusing and focusing effects depending on the frequency of the laser pulses [14,15]. Many investigations on the impact of high repetition rate laser pulse have recently been conducted. where the heat load from the laser pulse train overflows NLO effects. There were many attempts to achieve NLO property without thermal suppression from condense laser pulses. Recently, pulse picker and optical chopper were used to maintain the accumulative heat effect in a medium [16]. These methods do have limitations, though, because of how they work. For instance, the cumulative heat effect from condensed laser pulses is reduced when the NLO property is obtained via an optical chopper [17]. Alternately, increasing the signal-to-noise ratio to account for the effect of NLO [18].

The mechanics underlying the focusing and defocusing phenomena in materials can be understood when the material molecule interacts with light [19]. Thermal load may develop close to the lighted volume as a result of energy loss through radiative and non-radiative processes [20]. Thermal degradation occurs over a period of milliseconds or longer. The material is heated as a result, changing its nonlinear refractive index (n_2). The material's refractive index may change in one of two ways, including a positive refractive index change (light converges), also known as self-focusing. Self-defocusing is a negative refractive index change (divergence of light) [21].

The Z-scan approach was proposed as one of the most simple, accurate, and well-established methods for examining a material's NLO characteristic [22]. Z-scan method is a very sensitive approach for identifying the sign and values of the real and imaginary components of $\chi^{(3)}$ respectively. They are connected to the nonlinear absorption (NLA) coefficient and the nonlinear refractive index (NLR). Due to the method's ease of use in both the experimental setup and data processing, it has been widely adopted [23]. This paper's main goal is to discuss the thermal effect that results from the interaction of laser pulses with ZnO thin films. Depending on the target material, zinc oxide (ZnO) thin films was used in this research for its wide properties such as, high thermal conductivity [24], good transparency [25], has a 60 meV high exciton binding energy with a large 3.37 eV straight band gap [26]. Making it use in many application in optoelectronic devices such as solar cells [27], photodetectors [28,29], light emitting diodes [30], etc. The nonlinear property of this material will

determine how well it can be used to analyze how thermal load affects nonlinear refraction and absorption.

In this study, we present a straightforward way for investigating, using the Z-scan method, the impact of laser frequency operation on the NLO characteristics of ZnO thin films. We show that this technique works well for estimating the third-order nonlinearities of ZnO.

2. Experimental Work

Experiment Setup: For ZnO thin films, the NLR index and NLA coefficient were measured using the Z-scan technique. ZnO thin films were applied to the glass substrates using the air pressure chemical vapor deposition (APCVD) process. The samples were deposited for 20 min at a temperature of 500 °C. To eliminate all the impurities, substrates were first ultrasonically cleaned with acetone, ethanol, and distilled water for around 15 min in each solution. These substrates were then dried in a hot air stream. The grown film's estimated thickness was close to 425 nm. Further experimental details can be found elsewhere [31]. The material was placed on a rotational stage controlled by an ARDUINO and moved through the incident laser path as it moved closer to the focus. A CW red laser diode operating in continuous-wave mode with a maximum output power of (<3mW) was used as the light source.

The laser transmission was measured using the experimental Z-scan technique setup, which is depicted in Fig. (1). Using a lens with a focal length of around 30 cm, the laser beam was focused. In a closed aperture arrangement, it is applied to an aperture with a diameter of (0.5 mm).

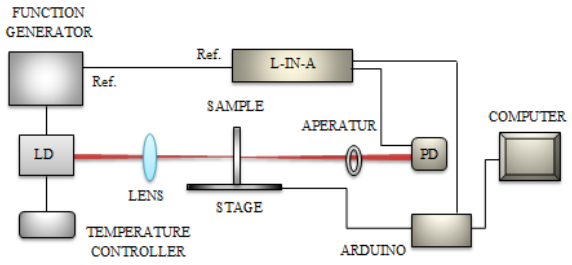

Fig. (1) The Z-scan experimental setup; where PD is a photodetector, LD is a laser diode, L-in-A is a Lock-in-Amplifier

Using the edge knife technique, the laser beam waist radius (w) was measured, and it was discovered to be 27 m. 3.52 mm, which was used to compute the Rayleigh length equation [32]

$$Z_R = \frac{\pi w_0^2}{\lambda} \qquad (1)$$

where Z_R is the Rayleigh length (also referred as Z_0), and λ is the laser wavelength

The laser beam was detected by a Silicon photo detector silicon photo detector (DET10A). Stable temperature is required in the setup. As it can affect the laser parameters such as the laser efficiency, wavelength and threshold current. leading to an alteration in the material's nonlinearity. The used temperature controller accuracy is of ±0.05 °C. The CW laser diode was converted to a pulse laser diode as the study dependent on the frequency variation, a Function Generator was employed in the setup.

The Lock-in-Amplifier (L-IN-A) of the model SR830 DSP was used to take an accurate measurement even when the signal is small. The measurement is rejected and unaffected by noise signals at frequencies other than the reference frequency.

To investigate the NLA coefficient, the linear absorption coefficient determination from Eq. (2). is required [33]. The material's absorbance is taken at different wavelengths, as shown in Fig. (2). Where it can clearly notice a decrease in both the NLA coefficient and the absorbance with the increasing of wavelength.

$$\alpha_0 = \frac{2.303A}{L} \qquad (2)$$

where α_0 is the linear absorption coefficient, A is the material's absorbance, and L is the sample thickness

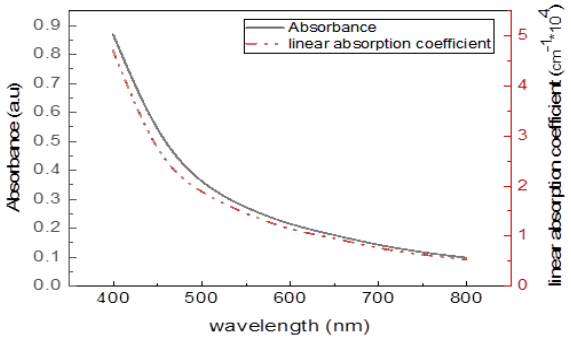

Fig. (2) Absorption spectra and linear absorption coefficient of ZnO thin films

3. Results and Discussion

Figure (3) displays the normalized transmittance curves for ZnO thin films at various frequencies using an open aperture Z-scan. The measurements were taken at a fixed laser intensity, which is equal to 2mW. When the nonlinear sample is moved in a Gaussian laser beam path toward the focal point in the (-Z) direction. The transmission of the laser beam shows a decrease until it reaches its minimum value at the focus of the lens. Whereas the sample continues to move toward the (+Z) direction, then the laser transmission will be increased. The laser transmission will exhibit a valley shape, which indicates the occurrence of the multi-photon process represented in the two-photon absorption (TPA). Making the sign of the TPA coefficient to be positive, as shown in table (1). In Fig. (3b), a widening and sharp decrease can be noticed in the (-Z) area compared with the curves in Figure 3a. For the valley, we can notice a lack of symmetry between (-Z) and (+Z). This shows that not all the transmitted light by the sample were collected by the detector [34].

 ISSN (print) 1813-2065, (online) 2309-1673

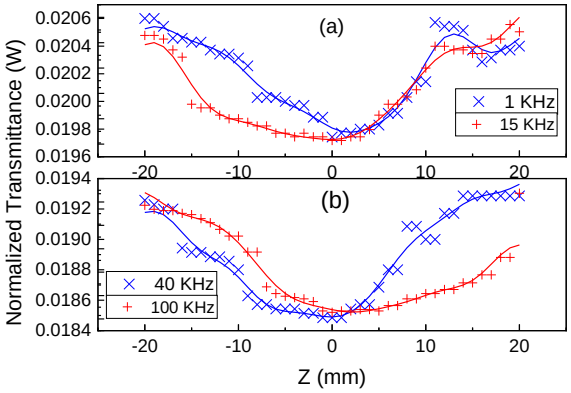

Fig. (3) The normalized transmittance curves at open aperture Z-scan for ZnO thin film at different frequencies. P =2mW, the peak intensity at focus I_0=174.74W/cm^2 (a) f=1kHz; f=15kHz, (b) f=40kHz; f=100kHz

Table (1) The extracted values of nonlinear absorption coefficient (β), nonlinear refractive index (n_2), imaginary (Im($\chi^{(3)}$) and real (Re($\chi^{(3)}$) parts of nonlinear susceptibility and total nonlinear optical susceptibility ($\chi^{(3)}$) of ZnO thin films

f kHz	β cm/W	n_2x10^{-4} cm^2/W	Im ($\chi^{(3)}$) x10^{-2} esu	Re ($\chi^{(3)}$) x10^{-2} esu	$\chi^{(3)}$ x10^{-2} esu
1	7.502	1.774	0.397	1.814	1.85
15	6.924	1.647	0.366	1.685	1.72
40	8.255	-2.02	0.436	-2.066	2.11
100	6.137	-1.998	0.324	-2.044	2.06

The data have been collected from the experimental setup for Z-scan technique, as shown in Fig.1, and fitted through equations (3) and (4) [35]:

$$T(z) = \frac{1+q_0(z)}{q_0(z)} \qquad (3)$$

Here

$$q_0 = \frac{\beta I_0\left[1-\frac{e^{-\alpha_0 L}}{\alpha_0}\right]}{1+\left(\frac{z}{z_0}\right)^2} \qquad (4)$$

where I_0 is the laser intensity at the focus, which can be calculated from the following: $I_0=2P/\pi w_0^2$

Figure (4) shows the normalized transmittance curves at closed aperture Z-scan for ZnO thin films at different frequencies, in which a nonlinear refractive index can be detected. The nonlinear index has the maximum change at the center, for a beam that has the highest intensity at the center [36]. When the nonlinear sample is moved along the Gaussian laser beam path, two processes occur when changing the frequency. The self-focusing and defocusing processes occur at low and high frequencies, respectively.

At low frequencies of 1–15 KHz, a valley-to-peak shape occurs when the sample is moved along the axis toward the focus. This leads to a positive sign for NLR index. While at higher frequencies of 40–100 kHz, a peak-to-valley shape occurs when the sample transitions along the axis toward the focus. This indicates a negative sign for the NLR index, as shown in table (1). Here, the NL processes will convert from the self-focusing to self-defocusing and the NLR index sign will convert from a positive value to a negative one as the frequency is increased.

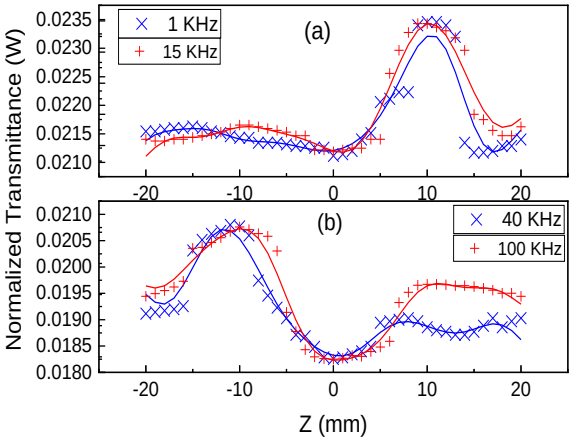

Fig. (4) The normalized transmittance curves at closed aperture Z-scan for ZnO thin films at different frequencies. P=2mW, the peak intensity at focus I_0=174.74 W/cm^2 (a) f=1kHz; f=15kHz, (b) f=40kHz; f=100kHz

This variation in the NLR sign with increasing the frequency is because of the thermal effect [22], this is due to the laser heating of the sample [37]. Where the thermal effects can't be neglected at those frequencies [38]. As the self-defocusing process is strongly correlated with the variation of the NLR index with temperature [39]. Generally, figure (4) shows a widening and depth with increasing in frequency because of the thermal effect. They occur as the frequency is increased, even at low frequencies started from 1 kHz [40]. The curves exhibit an improvement in the peak and valley-shape. Improving nonlinearities at higher frequencies compared with at low frequencies. The NLR index can be obtained by fitting the data to equations (5) and (6) [35]:

$$T(z) = 1 + \frac{(4\Delta\phi(I_0)_0(3).(\frac{z}{z_0})}{\left[\left(\frac{z}{z_0}\right)^2+9\right].\left[\left(\frac{z}{z_0}\right)^2+1\right]} \qquad (5)$$

Here,

$$\Delta\phi(I_\circ)_\circ(3) = K\,\Delta n[1-exp(-\alpha_\circ L)/\alpha_\circ] \qquad (6)$$

where $\Delta\phi(I_\circ)_\circ(3)$ is the third-order phase, K is the wavenumber that equals to $2\pi/\lambda$, and $\Delta n=n^2.I_0$ is the nonlinear change in the refractive index

The imaginary and real parts of nonlinear susceptibility were obtained using equations (7) and (8) [40]:

$$Im\,(\chi^{(3)}) = (10-2\,n_\circ 2\,\varepsilon_\circ c2\,\lambda/4\pi 2)\beta \qquad (7)$$

$$Re\,(\chi^{(3)}) = (10^{-4} n_\circ{}^2\,\varepsilon_\circ\,c^2/\pi)\,n_2 \qquad (8)$$

where n_0 is the linear refractive index, $\varepsilon_\circ$ is the vacuum permittivity, c is the speed of light in vacuum. The de-termination of the total third-order nonlinear optical susceptibility ($\chi^{(3)}$) can be performed as follows [41,42]:

$$|\chi(3)| = \sqrt{[Re\,(\chi^{(3)})]^2 + [Re\,(\chi^{(3)})]^2} \qquad (9)$$

4. Conclusions

With the use a simple Z-scan technique, the NLR index and NLA coefficient were measured separately. The data were extracted at different frequencies

within the range 1-100 kHz with a laser diode operating at 650 nm as an excitation source. The ZnO thin films' results indicate a positive sign for the TPA coefficient at both the low and high frequency range, a positive sign for the Kerr coefficient at a low frequency range that switches to a negative sign when the frequency range is higher.

References

[1] Y. Zhou et al., "Nonlinear optical properties of halide perovskites and their applications", *Appl. Phys. Rev.*, 7 (2020) 041313.
[2] O.A. Hamadi, "Characteristics of CdO-Si Heterostructure Produced by Plasma-Induced Bonding Technique", *Proc. IMechE, Part L, J. Mater.: Design & Appl.*, 222 (2008) 65-71.
[3] O.A. Hamadi and K.Z. Yahiya, "Optical and electrical properties of selenium-antimony heterojunction formed on silicon substrate", *Sharjah Univ. J. Pure Appl. Sci.*, 4(2) (2007) 1-11.
[4] E. Garmire, "Resource Letter NO-1: Nonlinear Optics", *Am. J. Phys.*, 79 (2011) 245–255.
[5] R. Edziah et al., "Z-scan measurements using ultrashort high-repetition-rate lasers: how to recognize the parasitic effects of non- linear behavior of fused-silica damage sites", *Peer J. Phys. Chem.*, 1 (2019) e1.
[6] R.A. Ismail et al., "Characterization of Si p-n Photodetectors Produced by Laser-Induced Diffusion", *Int. J. Mod. Phys.*, 19(31) (2005) 4619-4628.
[7] O.A. Hamadi, "Profiling of Antimony Diffusivity in Silicon Substrates using Laser-Induced Diffusion Technique", *Iraqi J. Appl. Phys. Lett.*, 3(1) (2010) 23-26.
[8] M. Vivacqua et al., "Application of the Z-scan technique to determine the optical Kerr coefficient and two-photon absorption coefficient of magnetite nanoparticles colloidal suspension", *J. Appl. Phys.*, 111 (2012) 113509.
[9] J. O'Dowd et al., "Polarization dependence of a GaAs-based two-photon absorption microcavity photodetector", *Opt. Exp.*, 16 (2008) 17682–17688.
[10] C. Gorling, "Self-trapped exciton luminescence and repetition rate dependence of two-photon absorption in CaF_2 at 193nm", *Opt. Commun.*, 216 (2003) 369–378.
[11] J. Szeremeta et al., "Wavelength Dependence of the Complex Third-Order Nonlinear Optical Susceptibility of Poly(3-hexylthiophene) Studied by Femtosecond Z-Scan in Solution and Thin Film", *J. Phys. Chem. C*, 117 (2013) 26197–26203.
[12] M.G. Vivas et al., "Polarization effect on the two-photon absorption of a chiral compound", *Opt. Exp.*, 20 (2012) 18600–18608.
[13] O.A. Hammadi and M.S. Edan, "Temperature Dependencies of Refractive Index and Optical Elasticity Coefficient on Lens Induced in Nd:YAG Crystal", *Iraqi J. Appl. Phys.*, 8(1) (2012) 35-41.
[14] M. Sheik-Bahae et al., "Nonlinear refraction and optical limiting in thick media", *Opt. Eng.*, 30(8) (1991).
[15] A.A.K. Hadi and O.A. Hamadi, "Optoelectronic Characteristics of As-doped Si Photodetectors Produced by LID Technique", *Iraqi J. Appl. Phys. Lett.*, 1(2) (2008) 23-26.
[16] J.A. Dávila Pintle, E.R. Lara and M.D. Iturbe Castillo, "Sensitivity optimization of the one beam Z-scan technique and a Z-scan technique immune to nonlinear absorption", *Opt. Exp.*, 21 (2013) 15350–15363.
[17] A. Nag, A.K. De and D. Goswami, "Two-photon cross-section measurements using an optical chopper: z-scan and two-photon fluorescence schemes", *J. Phys. B Atom. Mol. Opt. Phys.*, 42 (2009) 065103.
[18] O.A. Hamadi, B.A.M. Bader and A.K. Yousif, "Electrical Characteristics of Silicon p-n Junction Solar Cells Produced by Plasma-Assisted Matrix Etching Technique", *Eng. Technol. J.*, 28 (2008).
[19] A.K. Yousif and O.A. Hamadi, "Plasma-Induced Etching of Silicon Surfaces", *Bulg. J. Phys.*, 35(3) (2008) 191-197.
[20] O.A. Hamadi, "Effect of Annealing on the Electrical Characteristics of CdO-Si Heterostructure Produced by Plasma-Induced Bonding Technique", *Iraqi J. Appl. Phys.*, 4(3) (2008) 34-37.
[21] R.A. Ismail et al., "Full characterization at 904 nm of large area Si p-n junction photodetectors produced by LID technique", *The Euro. Phys. J. – Appl. Phys.*, 38(3) (2007) 197-201.
[22] B.A.M. Badr, O.A. Hamadi and A.K. Yousif, "Measurement of thermooptic coefficient of semiconductors by single-beam scanning technique", *Eng. Technol. J.*, 27(5) (2007).
[23] O.A. Hamadi, N.J. Shakir and F.H. Mohammed, "Magnetic Field and Temperature Dependent Measurements of Hall Coefficient in Thermal Evaporated Tin-Doped Cadmium Oxide Thin Films", *Bulg. J. Phys.*, 37(4) (2010) 223-231.
[24] R. Kumar et al., "ZnO nanostructured thin films: Depositions, properties and applications: A review", *Mater. Exp.*, 5 (2015) 3–23.
[25] Z.L. Wang, "Zinc oxide nanostructures: growth, properties and applications", *J. Phys. Cond. Matter.*, 16 (2004) R829.
[26] E. Bacaksiz et al., "The effects of zinc nitrate, zinc acetate and zinc chloride precursors on investigation of structural and optical properties of ZnO thin films", *J. Alloys Comp.*, 466 (2008) 447-450.
[27] S. Abed et al., "Nonlinear optical properties of zinc oxide doped bismuth thin films using Z-scan technique", *Opt. Mater.*, 56 (2016) 40–44.

 ISSN (print) 1813-2065, (online) 2309-1673

[28] Z.A. Wang et al., "Growth of ZnO:Al films by RF sputtering at room temperature for solar cell applications", *Solid State Electron.*, 53 (2009) 1149-1153.
[29] J. Sun et al., "The ultraviolet photoconductive detector based on Al-doped ZnO thin film with fast response", *Sci. China. Ser. G: Phys. Mech. Astron.*, 54 (2011) 102-105.
[30] O.A. Hammadi, "Electrical and Spectral Characteristics of Visible-Blind ZnO/Si Heterojunction Fabricated by Plasma-Induced Bonding", J. Optoelctron. Photon., 7(5) (2016) 21-24.
[31] J.-H. Bae and H.-K. Kim, "Characteristics of Al doped ZnO co-sputtered InZnO anode films prepared by direct current magnetron sputtering for organic light-emitting diodes", *Thin Solid Films*, 516 (2008) 7866-7870.
[32] Y.H. Mohammed, "Fabrication of n-MgZnO/p-Si heterojunction diode: Role of magnesium doping", *Superlat. Microstr.*, 131 (2019) 104-116.
[33] M. Borhani Zarandi and H. Amrollahi Bioki, "Effects of cobalt doping on optical properties of ZnO thin films deposited by sol-gel spin coating technique", *J. Optoelectron. Nanostr.*, 2 (2017) 33-44.
[34] W.R. Saleh et al., "Synthesis Sol-Gel Derived Highly Transparent ZnO Thin Films for Optoelectronic Applications", *Adv. Mater. Phys. Chem.*, 2 (2012) 11-16.
[35] M. Vivacqua, D. Espinosa and A. Martins Figueiredo Neto, "Application of the Z-scan technique to determine the optical Kerr coefficient and two-photon absorption coefficient of magnetite nanoparticles colloidal suspension", *J. Appl. Phys.*, 111 (2012) 113509.
[36] M. Sheik-Bahae et al., "Sensitive Measurement of Optical Nonlinearities Using a Single Beam", *IEEE J. Quantum Electron.*, 26 (1990) 760-769.
[37] S. Singhal, S. Dinda and D. Goswami, "Measurement of pure optical nonlinearity in carbon disulfide with a high-repetition-rate femtosecond laser", *Appl. Opt.*, 56 (2017) 644–648.
[38] C.A. Carter and J.M. Harris, "Comparison of models describing the thermal lens effect", *Appl. Opt.*, 23 (1984) 476.
[39] L. Zhang et al., "Femtosecond Z-scan measurements of the nonlinear refractive index of fused silica", Proc. Vol. 10621, 2017 *Int. Conf. on Opt. Instrum. Technol.: Optoelectron. Measur. Technol. Sys.*; 106210H (2018)
[40] J. Amoani, "Intensity dependent nonlinear refractive index of fused silica", MSc thesis, University of Eastern Finland (2019).
[41] A. Gnoli, L. Razzari and M. Righini, "Z-scan measurements using high repetition rate lasers: how to manage thermal effects", *Opt. Exp.*, 13 (2005) 7976–7981.
[42] M.B. Zidan et al., "Z-scan measurements of the third order optical nonlinearity of C60 doped poly(ethylacetylenecarboxylate) under CW regime", *Optik*, 127 (2016) 2566–2569.

IRAQI JOURNAL OF APPLIED PHYSICS
Vol. 19, No. 3B, September 2023, pp. 30-34

Determination of Mass and Linear Absorption Coefficient for Some Reinforced Polymeric Materials from X-Ray Characteristics

Lubna H. Ismael
Ghazwan G. Ali
Raad A. Rasool

Department of Physics, College of Education for Pure Sciences, University of Mosul, Mosul, IRAQ

The composite materials with polymer-based were prepared by using hand lay-up of epoxy resin as a base material supported by Al_2O_3 nanoparticles and by weight (5%, 10%, 15%). Radiation attenuation measurements were carried out using Cu tube x-ray unit of different voltages (13, 15, 17, 19, and 21 kV) to demonstrate the effect of the addition of epoxy alumina to x-ray radiation blocking. The linear attenuation coefficient and coefficient mass attenuation for the same range of voltages above, and through the correlation between the absorption logarithm and thickness as well as the equivalent thickness, respectively. The results obtained on the efficiency of the material produced in x-ray absorption and attenuation, and this efficiency is relatively variable according to the added ratio, indicating the positive effect of this additive on the properties of radiation shielding of epoxy and alumina composite.

Keywords: Composite materials; Epoxy; Alumina; X-ray attenuation
Received: 11 March 2023; Revised: 24 March 2023; Accepted: 31 March 2023

1. Introduction

Polymeric materials are derived from oil, natural gas, coal. Polymers are known as giant chemical bonds consist of a large number of atomic aggregates. These chains named as repeated units and called as monomer, which is the basic unit of polymer construction [1].

Polymers are widely used in technology, industrial and electronic applications. However, there are still some engineering problems for polymers such as their lack of stiffness, strength relative to metals, many methods have been used to improve these defects such as fiber reinforcement such as Fakers, Fillers or Particles to strengthen polymer particle cohesion [2,3]. Thus, it is possible to obtain good industrial materials called composite materials, which are defined as the solid systems resulting from the participation of two or more materials, each material represents a separate phase in the system, including the reinforcement phase in order to obtain new materials with suitable properties between the properties of the raw materials involved in the preparation of the composite materials to pass the bad properties of the materials to be reach more suitable for industrial applications [4,5].

The present study aims to study the effect of addition ratios of alumina nanopowder on linear and mass attenuation coefficients of epoxy resin in range of energy 13-21 kV and conduct a theoretical study to calculate the mass attenuation coefficient of x-ray of the composite materials and compare it with the practical results.

2. Experimental work

One of the most important x-ray characteristics is represented by its ability to penetrate different materials. This penetration is not absolutely but relatively. When a pack of x-ray photons passes across a degenerated medium, each photon in this package does not react at all medium or interacts with absorption and scattering reactions as a result of the release of photons. The intensity or energy decreases with the length of the path that the ray travels through this medium [6].

When the intensity of package single-photon energy (I_0) falls on the target of the thickness (dx), the decrease in intensity (dI) from the initial intensity value (I_0) due to the photon's interaction, emission and absorption can be represented by the following equation [7]:

$$dI = -\mu\, I_0\, dx \quad (1)$$

By complementing Eq. (1) we obtain:

$$I = I_0\, e^{(-\mu x)} \quad (2)$$

The magnitude of $e^{(-\mu x)}$ represents the probability that the photon will intersect the distance (x) within the interceptor medium (dissolved) without any interaction, and that it may react after the distance (x) directly crossed, and the beam has suffered an exponential decrease (μ) in intensity with the length of the distance, where ($I<I_0$), and then Eq. (2) becomes as follows:

$$\frac{I}{I_0} = e^{(-\mu x)} \quad (3)$$

Thus, μ can be calculated by Eq. (2) to be as follows:

$$\mu = \frac{Ln\, A}{x} \quad (4)$$

 ISSN (print) 1813-2065, (online) 2309-1673 PRINTED IN IRAQ

As x is the samples thickness (cm), $A=I_0/I$ is the attenuation ratio [8].

The term μ is the proportionality constant (denotes x-attenuation coefficient), which is generally dependent on the photon energy, the type of interaction of the incident photon, structure and density of the intercepting medium. The attenuation role is described by the type of attenuation medium. It demonstrates mathematical formula of the incident particle. There are many attenuation functions include [9]:

1- Mathematical formula of attenuation. It occurs in medium with a thickness of dx. The probability will be very small of the aborted photon in this medium ($\mu dx<<1$). Therefore, the attenuation can be as following form:
$$I = I_0(1 - \mu dx) \quad (5)$$
2- Gaussian attenuation is the important factor to describe the attenuation of charge particles which is related this attenuation of Gauss's function (Gaussian distribution).
3- Exponential attenuation is used to describe photon energy of the attenuated medium. Additionally, the intensity of the beam decreases into the medium. Every photons in the package are deleted from the reactive package individually with the attenuated center atoms [10]. The attenuation coefficient (μ) is calculated by cm^{-1} of the incident photon, it is called the total linear attenuation coefficient (μ_L). Furthermore, the total mass attenuation coefficient (μ_m) is measured by units (cm^2/g) as the following equation:
$$\mu_m = \frac{\mu_L}{\rho} = \frac{ln(I_0/I)}{\rho x} \quad (6)$$

where ρ and x are the density and thickness of the medium, respectively [11]

The free path rate is defined as the average distance traveled by photon in the interceptor medium before it is removed from the beam, and is expressed mathematically by the relationship [12]:
$$\lambda = \frac{1}{\mu} \quad (7)$$

where λ is in cm or gm/cm^2 depending on the coefficient of attenuation (μ) whether linear or mass, and the standard deviation of the σ_λ will be calculated from the following relationship:
$$\sigma_\lambda = \frac{x}{A(ln\ A)^2} . \sigma_\mu \quad (8)$$

where $A=I_0/I$ is the attenuation ratio

The thickness required to attenuate the intensity of radiation passing through it to half value of its original value is known as half thickness ($X_{1/2}$), its units are cm or g/cm^2.

The half thickness associated with the attenuation coefficient by the following physical equation:
$$X_{\frac{1}{2}} = \frac{ln\ 2}{\mu} \quad (9)$$

To adopt half thickness on attenuation coefficients, it will have a standard deviation accordingly and given the following relationship:
$$\sigma_{\frac{1}{2}} = \sigma_\lambda . (Ln\ 2) \quad (10)$$

where σ_λ represents the standard deviation of the average of free-pass

The materials used in this study are:

(1) Matrix material: The base material used is the Turkish epoxy resins, transparent viscosity medium its density is 1.05 g/cm^3 and prepared by mixed with DEBE-A (Dia Ethylene Bis Epoxy-A) with the material of the crucifixion (DT) (Hardener: Dia Tetrawen), and for volume of (3R./1H.).

(2) Reinforcement material: Alumina powder in grain boundary nanotubes (30nm) of Chinese origin with density of 3.98 g/cm^3, has been exclude micrometric volume for deposition below the sample.

The compound was prepared from Al_2O_3 and in the following weights for samples **A**(95%, 5%), **B**(90%, 10%) and **C**(85%, 15%). The composite was placed in a plastic mold in form of parallel rectangles, before the casting process, the mold was cleaned with acetone followed by drying and placing a vaplon sticker inside walls of mold and then coated with a thin layer of sliding material such as Paraffin Wax to facilitate the removal of the molded material from the mold. After extracting the mold left for 5 days to harden and then placed in oven at temperature of 50-55°C to complete the tangling process.

A PHYWE x-ray instrument equipped with a Cu-tube and a Geiger-Miller thermometer was used, where the equivalent thickness and all samples were measured in cubes, with a square base of 10 mm length with different thickness after measuring its mass by means of the sensitive electrical balance and determining its density using the following equation:
$$\rho_{sample} = \left(\frac{m_s}{V_t}\right) = \frac{m_s}{\pi r^2 x} \quad (11)$$

As m_s is the mass of sample, V_t is the size of sample, x is the thickness of sample

The tables from (1) to (3) cleared the values of thickness, mass, apparent density and thickness equivalent to the different research samples on the sequence as in tables (1-3).

Table (1) Thickness, mass, apparent density and thickness equivalent to sample (A)

Thickness (cm)	Mass (g)	Apparent Density (g/cm^3)	Thickness Equivalent (g/cm^2)
0.25	0.29807	1.192282164	0.3153
0.23	0.27447	1.193343343	0.2900
0.20	0.23872	1.1936	0.2524
0.17	0.20285	1.193224886	0.2146
0.15	0.17892	1.192788836	0.1893

Table (2) Thickness, mass, apparent density and thickness equivalent to sample (B)

Thickness (cm)	Mass (g)	Apparent Density (g/cm^3)	Thickness Equivalent (g/cm^2)
0.25	0.31531	1.261227903	0.3153
0.23	0.28999	1.260811558	0.2900
0.20	0.25238	1.26188919	0.2524
0.17	0.21457	1.262160161	0.2146
0.15	0.18931	1.262098524	0.1893

Table (3) Thickness, mass, apparent density and thickness equivalent to sample (C)

Thickness (cm)	Mass (g)	Apparent Density (g/cm³)	Thickness Equivalent (g/cm²)
0.25	0.3498	1.399200286	0.3498
0.23	0.322	1.400006365	0.3220
0.20	0.28001	1.400053763	0.2800
0.17	0.23826	1.401549293	0.2383
0.15	0.21008	1.400565379	0.2101

3. Results and Discussion

The linear attenuation (μ_L) and mass attenuation (μ_m) values were obtained through the linear equations. Figures (1), (2) and (3) represent the linear relationship between x-ray and x(cm), and that the slope the linear line of linear equations represents the practical values of the linear attenuation coefficient.

The study of these forms showed that the increase in thickness is accompanied by an increase in the absorption logarithm and the voltage range is 13-21kV.

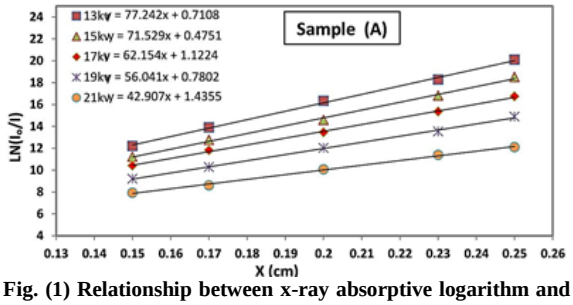

Fig. (1) Relationship between x-ray absorptive logarithm and thickness

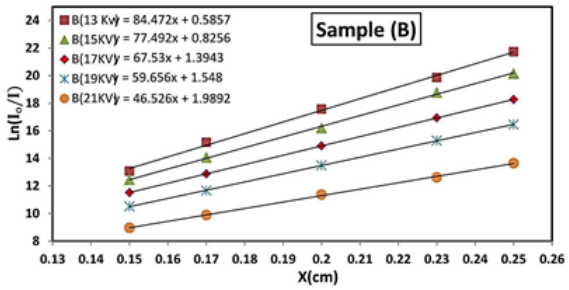

Fig. (2) Relationship between x-ray absorptive logarithm and thickness

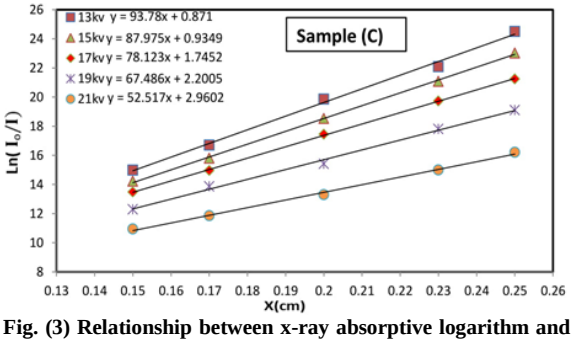

Fig. (3) Relationship between x-ray absorptive logarithm and thickness

Figures (4), (5) and (6) show that the linear relationship between x-ray absorptive logarithm and equivalent thickness x_m (cm/cm^2), the linear slope of linear equations represents the practical values of mass attenuation coefficient (μ_m) for all the samples.

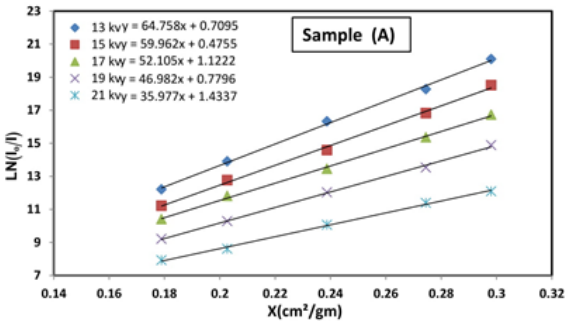

Fig. (4) Relationship between x-ray absorptive logarithm and thickness

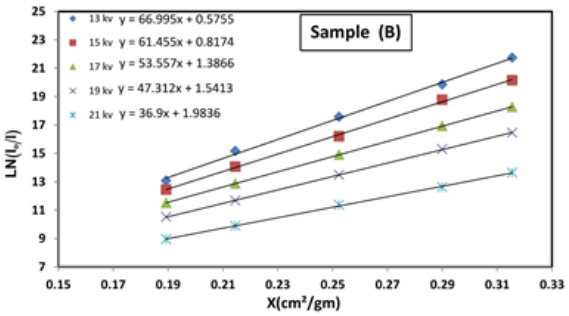

Fig. (5) Relationship between x-ray absorptive logarithm and thickness

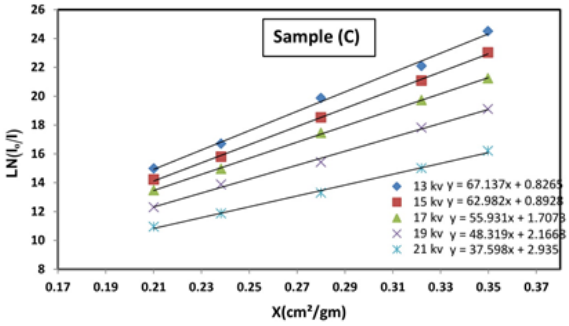

Fig. (6) Relationship between x-ray absorptive logarithm and thickness

The total linear attenuation coefficient of x-ray (μ_L) in the range of voltages used in the present study for all the research samples after measuring the counting rates of (I_0, I) was measured by using Eq. (4). The results of this equation represent the theoretical values, in table (4).

Table (4) Total linear attenuation coefficient for samples A, B, and C

U (kV)	μ_L (exp)			μ_L(theo)		
	A	B	C	A	B	C
13	77.242	84.472	93.78	78.381	85.589	94.951
15	71.529	77.492	87.975	73.622	78.604	89054
17	62.154	67.53	78.123	63.074	68.427	79.396
19	56.041	59.656	67.486	57.298	60.522	68.561
21	42.907	46.526	52.517	43.411	47.734	53.422

The total mass attenuation coefficient (μ_m) from Eq. (6) was also calculated, the virtual density of the

 ISSN (print) 1813-2065, (online) 2309-1673

research samples was calculated according to Eq. (11), which was included in tables (1), (2) and (3) as shown in table (5).

Table (5) Total mass attenuation coefficient for samples A, B, and C

U (kV)	μ_m (exp)			μ_m (theo)		
	A	B	C	A	B	C
13	64.785	66.976	67.024	64.182	65.836	66.115
15	59.94	61.462	62.839	59.227	60.823	61.259
17	52.071	53.515	55.8	51.661	52.615	54.903
19	46.966	47.265	48.151	46.159	46.941	47.44
21	35.972	36.864	37.497	35.248	35.908	36.677

The average free path values of linear and mass x-ray attenuation coefficients of the research samples were calculated with standard deviation values according to the equations (7) and (8), respectively, increasing in values are shown in tables (6) and (7) by increasing voltages [13].

Table (6) Values of average free path and standard deviation of linear attenuation coefficient for samples A, B, and C

U (kV)	Average Free Path $\lambda_L=1/\mu_L$			Standard Deviation		
	A	B	C	A	B	C
13	0.0129	0.01184	0.0107	0.0037	0.0038	0.0034
15	0.0140	0.0129	0.0114	0.0035	0.0037	0.0033
17	0.0161	0.01481	0.0128	0.0031	0.0034	0.0032
19	0.0178	0.01676	0.0148	0.0027	0.0033	0.0030
21	0.0233	0.02149	0.0190	0.0024	0.0031	0.0028

Table (7) Values of average free path and standard deviation of mass attenuation coefficient for samples A, B, and C

U (kV)	Average Free Path $\lambda_L=1/\mu_L$			Standard Deviation		
	A	B	C	A	B	C
13	0.0154	0.01493	0.0149	0.0044	0.0048	0.0047
15	0.0167	0.01627	0.0159	0.0041	0.0047	0.0047
17	0.0192	0.01869	0.0179	0.0037	0.0043	0.0045
19	0.0213	0.02116	0.0208	0.0033	0.0042	0.0042
21	0.0278	0.02713	0.0267	0.0028	0.0040	0.0039

The half-thickness values of linear and mass attenuation coefficients of x-ray for all samples were calculated with standard deviation values according to the equations (9) and (10), respectively, as shown in tables (8) and (9) by increasing half thickness for linear and mass attenuation of all samples by increasing voltages.

Table (8) Values of half thickness and standard deviation of linear attenuation coefficient for samples A, B, and C

U (kV)	Half Thickness $X_{1/2}=Ln2/\mu_L$			Standard Deviation		
	A	B	C	A	B	C
13	0.0090	0.0082	0.0074	0.0022	0.0020	0.0018
15	0.0097	0.0089	0.0079	0.0020	0.0018	0.0017
17	0.0111	0.0103	0.0089	0.0019	0.0018	0.0016
19	0.0124	0.0116	0.0103	0.0019	0.0016	0.0015
21	0.0162	0.0149	0.0132	0.0017	0.0015	0.0014

Table (9) Values of half thickness and standard deviation of mass attenuation coefficient for samples A, B, and C

U (kV)	Half Thickness $X_{1/2}=Ln2/\mu_L$			Standard Deviation		
	A	B	C	A	B	C
13	0.0107	0.0103	0.0103	0.0025	0.0025	0.0025
15	0.0116	0.0113	0.0110	0.0023	0.0023	0.0024
17	0.0133	0.0129	0.0124	0.0023	0.0022	0.0023
19	0.0148	0.0147	0.0144	0.0023	0.0021	0.0020
21	0.0193	0.0188	0.0185	0.0021	0.0020	0.0019

Scanning electron Microscope (SEM) images in Fig. (6) show Al_2O_3 nanoparticles deposited on epoxy. It can be seen that the distribution of nanoparticles was uniform for all different weights of Al_2O_3 layers. Moreover, it was found that the deposited alumina covered all the surface of substrate. However the surface roughness was increased with increasing of Al_2O_3 thickness because the particles size is associated with the film thickness [14].

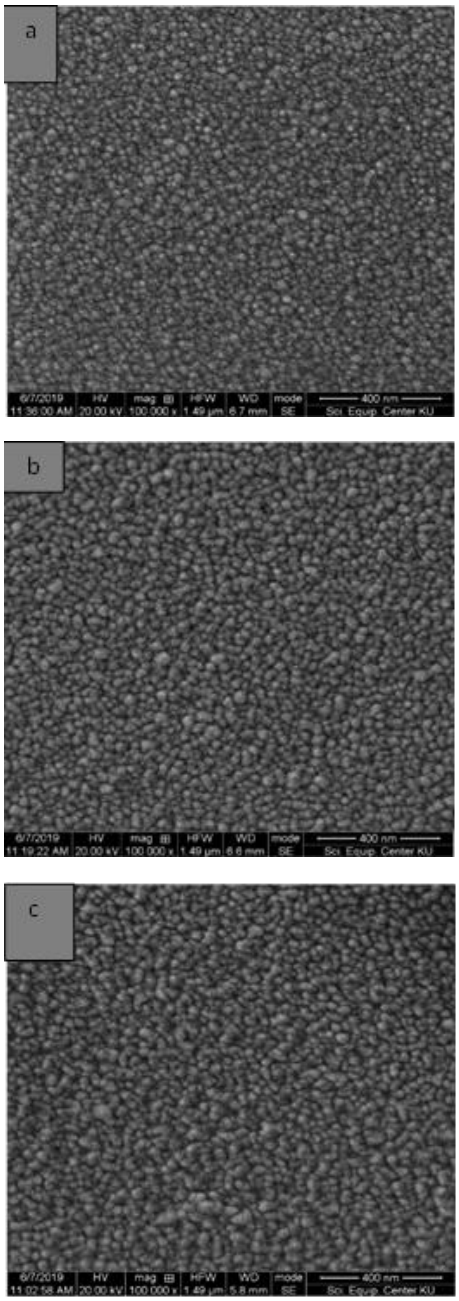

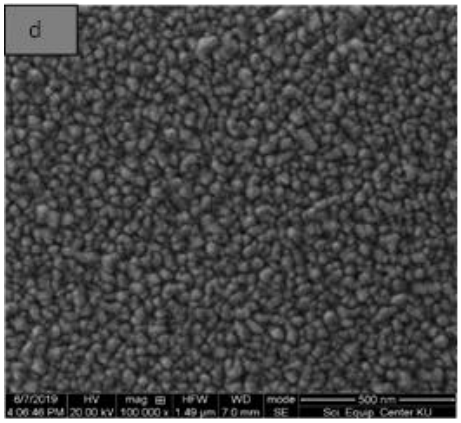

Fig. (7) SEM images of Al_2O_3 nanoparticles for weight (5%, 10%, 15%) on Epoxy

4. Conclusions

The results obtained on the efficiency of the material produced in the x-ray absorption and attenuation showed that the efficiency is relatively variable according to the added ratio, indicating the positive effect of this added on the radiation shielding properties of the epoxy and alumina composites.

References

[1] M.P. Stevens, **"Polymer Chemistry"**, Oxford University Press (NY, 1999).
[2] A. Nadhim et al., J. Al-Qadisiyah Pure Sci., 17 (2012) 1-16.
[3] R.A. Rasool, G.G. Ali and N.A. Hussein, "The Effect of Epoxy Layer Supported by Carbon, Alumina and Silica Grains on the solar cell", *Dig. J. Nanomater. Biostruct.*, 14(3) (2019) 743-750.
[4] P.A. Thomton and V.J. Colengelo, **"Fundamentals of Engineering Materials"**, Prentice Hall, Inc. (1985).
[5] M. Grayson, **"Encyclopedia Materials and Components"**, John-Wiley and Sons (NY, 1983).
[6] W.R. Leo, **"Techniques for Nuclear and Particle Physics Experiments"**, Springer-Verlag (Berlin, 1987).
[7] A. Azzouz, **"Introduction to Nuclear Physics"**, University of Mosul (Mosul, 1983).
[8] A.E. Profio, **"Radiation Shielding and Dosimeter"**, John-Wiley and Sons, Inc. (1979).
[9] P.P. Pawar and C.S. Mahajan, "Measurement of Mass and Linear Attenuation Coefficient of Gamma-Rays of Glycine for 0.360 MeV Photons", *Sci. Res. Report.*, 3(1) (2013) 53-56.
[10] C. Laxman and R. Dayanand, "Attenuation Coefficient of Soil Samples by Gamma Ray Energy", *J. Recent Sci.*, 1 (2012) 41-48.
[11] S.L. Mitkar, "Measurment of Linear and Mass Attenuation coefficient of Alcohol soluble compound for Gamma rays at energy 0.511 Mev", *Archiv. Appl. Sci.*, 4 (2012) 1748-1752.
[12] W.H. Tait, **"Radiation Detection"**, Butterworths (UK, 1980).
[13] Y.K. Yasir, G.G. Ali and M.H. Younus, "Irradiation Effects on The Sensitivity of ZnO Thin Films Synthesized on Glass Substrate by Sol-gel Method", *Iraqi J. Sci.*, 62(1) (2021) 130-137.
[14] L. Rabih, G.G. Ali and M.H. Younus, "Evaluation of optical and electrical properties of TiO_2 thin films doped Cu ions", *AIP Conf. Proc.*, 2201 (2019) 020001.

 ISSN (print) 1813-2065, (online) 2309-1673

IRAQI JOURNAL OF APPLIED PHYSICS
Vol. 19, No. 3B, September 2023, pp. 35-38

Influence of Light Intensity and Irradiation Time on Efficacy of Polymerization Temperature Using Diode Laser and Light-Emitting Diodes

Muna Y. Slewa
Rajaa A. Basheer
Malik H. Kheder
Balsam W. Jarjees

Department of Physics, College of Education, University of Al-Hamdaniya, Ninawa Province, IRAQ

When composite resin light-curing is used in dental treatment, a significant amount of heat is produced, which can result in dental injury. This study used two LED processing units versus diode laser methods to measure the temperature increase caused by changes in light intensity during polymerization. At each irradiation time, three samples were collected (10, 20, 30, 40, 50, and 60 s). The findings revealed that light intensity and irradiation time had a significant impact, accounting for 85 percent of the temperature variations. When using a continuous light-cure LEDB with the intensity of light (1400 mw.cm^{-2}) the temperature rises, which has a negative impact on tooth restoration. Temperatures do not rise when using a light-cure device at intensity levels of light (250 mw.cm^{-2} or 900 mw.cm^{-2}). As a result, for tooth restoration, a laser diode with a lower light intensity (250 mw.cm^{-2}) is recommended.

Keywords: Light intensity; Irradiation time; Diode laser; Polymerization temperature
Received: 11 March 2023; Revised: 24 March 2023; Accepted: 31 March 2023

1. Introduction

In recent years, dental lasers have grown in popularity. Many areas of dentistry benefit from laser technology, including surgery, conservative care, polymerization, tooth whitening, and photodynamic therapy. Nonetheless, scientists have expressed interest in the visible region of the electromagnetic spectrum, where a variety of wavelengths are used, including red laser diodes at 655 nm, green KTP lasers at 532 nm, blue argon lasers at 488 nm, and diode lasers at 405 nm [1-3].

Blue laser diodes have been a significant advancement in laser diode history. The 405 nm blue diode laser interacts with the in vivo material in such a way it is greatly absorbed by hemoglobin and is more than an order of magnitude more absorbed by melanin than near-infrared light [4, 5]. Other studies have shown that this laser type is effective as a device for tooth whitening procedures [6-8]. Studies have shown that this laser has the potential to be used in Photodynamic Therapy as a photosensitizer for PDT. In conservative dentistry, halogen lamps are typically used to polymerize composite materials for teeth and LED modules are used. However, in recent years, dentists have been using low-power lasers. Intense visual light with wavelengths ranging from 400 to 500 nm was used to excite the dikton, resulting in the production of free radicals [9].

The unavoidable outcome of the chemical reaction is high temperature. The rising temperature is influenced by more than just the heat generated by polymerization during illumination and the chemical reaction that occurs during the material-setting process [10]. The authors found that as the density of the light source grew, so did the exothermic reaction speed of the visible-light activated composite resin. They came to the conclusion that the resin rather than the source light had a higher impact on the temperature rise during curing [11]. The unit of the light-activation generates the greatest amount of heat during light-activated restorative polymerization, not the material itself [12]. The curing lights emit thermal energy, which a professional dentist is concerned about. Heat transferred to the tooth can cause pulp damage [13]. Although it is feasible to cure LED lights so that the semiconductor source emits less heat laterally, it is unknown whether this means that the heat release is any less than that of the light guide tip. First-generation LED curing lights have a lower power density than the most recent light generation. LED curing lights produce less heat as a result of their limited emission range. Just a modest power density can be produced by the original LED lights. The concentrating effect and power density of light guides can be impacted by modifications to their curing distance, diameter, or material [14]. An LED light with a narrow emission spectrum has a higher curing efficiency [15,16].

This study sought to locate the best device and compare it to the one that emits the least heat by evaluating the polymerization effectiveness of laser diodes and light-emitting diode LED devices utilizing light intensity and laser diode with light irradiation time.

2. Experimental Work

The following light source units were used in this study:

Laser light intensity of 250 mw.cm^{-2} from a

1. diode laser beam with a wavelength of 405 nm [Fig. (1a)].
2. Light source unit with a wavelength range of 430–490 nm and a light intensity of 900 mw.cm^{-2}. [Fig. (1b)].
3. LED.B light source unit with a wavelength range of 440–490 nm and a light intensity of 1400 mw.cm^{-2} (both pulse and continuous) radiation [Fig. (1c)].

(a) Diode laser

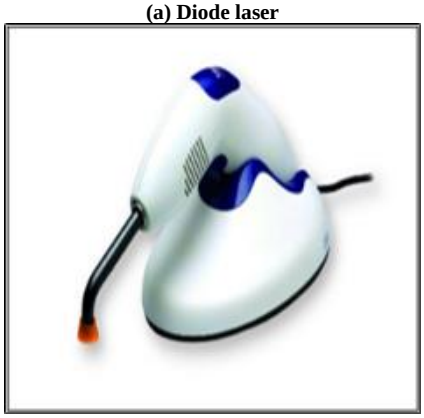

(b) LEDition

(c) LED.B

Fig. (1) Light sources used in this work

An HTC-2 digital LCD thermocouple with a timer was used to measure the irradiation time. Figure (2) shows the arrangement of these devices. The laboratory temperature was recorded every 10 seconds for a minute, and the temperature was recorded for 1 min with three repeated readings.

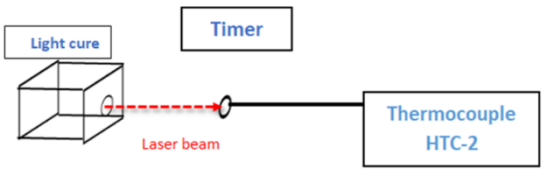

Diode laser

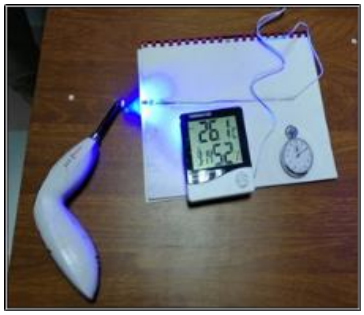

LED.B

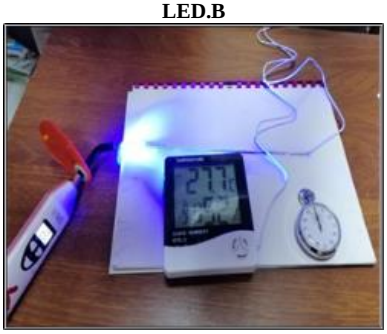

LEDition

Fig. (2) The experimental setup used in the study

3. Results and Discussion

We obtained the results shown in table (1) after conducting the experiments in the laboratory. To determine the temperature increase from the laboratory temperature caused by the light intensity, we subtracted the laboratory temperature from each recorded temperature for each irradiation time, yielding table (2) and Fig. (3).

The rise in average temperatures using continuous light cure LED.B with light intensity (1400 mw/cm^2) at the times of irradiation (20, 30, 40, 50, and 60 seconds) is clearly greater than the rise in average temperatures using other light intensity levels, as shown in table (2) and Fig. (3). Consequently, we anticipate that the mean temperature using this light intensity level will be significantly different from other means.

 ISSN (print) 1813-2065, (online) 2309-1673

Table (1) The recorded average temperature at the time of irradiation using different levels of light intensity for laser diode and three light cure LED devices

Irradiation Time (s)	Laser Diode with Light Intensity (250 mW/cm^2)	Pulse Light Cure LED.B with Light Intensity (1400 mW/cm^2)	CW light Cure LED.B with Light Intensity (1400 mW/cm^2)	Light cure LEDition with Light Intensity (900 mW/cm^2)
10	21.10	26.00	25.50	25.40
20	21.90	26.95	28.05	26.20
30	22.35	27.80	29.45	26.80
40	22.75	28.70	30.65	28.25
50	22.95	29.35	31.00	28.65
60	23.15	29.65	31.55	29.10

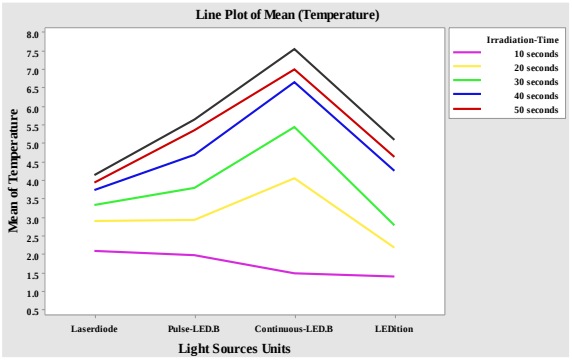

Fig. (3) Increase in average temperatures for different levels of light intensity at different irradiation times for all devices

Table (2) The increase in average temperatures (T_{av}-T_0) °C during irradiation time with various levels of light intensity

Irradiation Time (s)	Laser Diode with Light Intensity (250 mW/cm^2)	Pulse Light Cure LED.B with Light Intensity (1400 mW/cm^2)	CW light Cure LED.B with Light Intensity (1400 mW/cm^2)	Light cure LEDition with Light Intensity (900 mW/cm^2)
	T_0= 19°C	T_0= 24°C	T_0= 24°C	T_0= 24°C
10	2.10	2.00	1.50	1.40
20	2.90	2.95	4.05	2.20
30	3.35	3.80	5.45	2.80
40	3.75	4.70	6.65	4.25
50	3.95	5.35	7.00	4.65
60	4.15	5.65	7.55	5.10

Furthermore, as shown in Fig. (4), the average temperature increases with increasing radiation interval for all light intensity levels. We must understand the type and characteristics of radiation emitted by light cure units, as it can have characteristics within different emission spectral. The light and beam output can change dramatically during exposure. Also, laboratory instrumentation should to be used to describe the real-time spectral radiation intensity and spectral emission of the light cure units [17]. The diode laser with low radiation intensity was chosen to measure the temperature rise in this study. Dental clinics cannot use this gadget, so manufacturers should be encouraged to offer correct information about the light-producing properties of these devices.

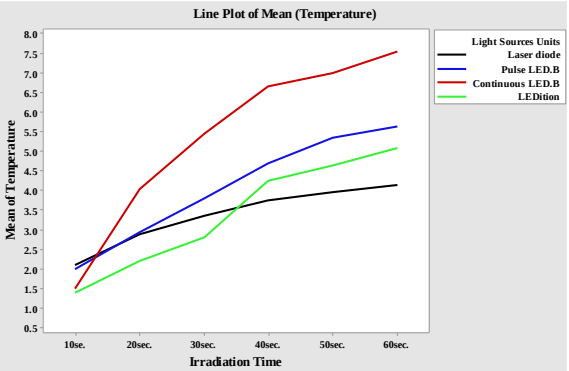

Fig. (4) Increase in average temperatures for various light intensities and irradiation time levels

When light sources are used, radiometers can be used to track changes in the light output, but care must be taken when checking the absolute radiation value. Researchers found a considerable difference between the radiation values recorded by radiometers and those measured in a lab, with the exception of light emitting diode (LED), which provided accurate data [18]. Because of its benefits, including energy efficiency, long life, and ergonomics, the light-emitting diode (LED) device is becoming more and more popular in the treatment of dental restorative materials. Another application of LED technology is a high-intensity beam positioned inside the body or at the far end of a gun or pen-like device [19]. The light that these devices emit does not contain infrared energy, but because it can reach energy densities higher than 2000 mW/cm^2, a large amount of heat can be anticipated to be emitted at the target [20]. Despite the fact that laser diode beam and LED curing modules produce light in different ways, these variations can be explained by a greater temperature rise, a greater output intensity, and longer exposure times than the same light beam profile. Evaluating the thermal changes during the photo polymerization of the composite must take into account all the variables, which include the type of device, wavelength, the intensity of the light produced, irradiation time, as well as the dental composite material. However, the use of new processing equipment must be considered, mainly due to the power achieved by those devices, as this study showed that we used a diode laser, which is used for the first time, as it achieved less heat generation with less intensity than the heat generated by a device LED. Hence, it is also necessary to use a pulsed mode or even modular medium-intensity to ensure a successful and exciting dental treatment.

4. Conclusions

Temperature is classified as a major operator in the occurrence of dental lesions; when the thermocouple is directly exposed to a laser beam for a while and the temperature is observed over time,

temperature differences and apparent differences between high temperatures for each device used in the study can be observed. The results showed that the light intensity and irradiation time had a significant influence, accounting of the temperature variations.

Using a continuous light cure LED.B at light intensity (1400 mw/cm^2) results in a significantly high temperature, which results in dental treatment, increasing the temperature of the tooth surface, and thus increasing the temperature, whereas using a light cure device at light intensity levels (250 mw/cm^2 or 900 mw/cm^2) does not result in a significant increase in temperature.

According to the results, it is preferable to use a low-intensity laser diode, which was used for the first time and according to the specifications that distinguished it and became ready for use with these specifications in the polymerization of the dental material, as the results showed good effectiveness, and here it turns out that the device worked to strengthen the outer layer of the material used in dental restoration. Increasing the irradiation time in this process reduces the shrinkage of the materials used in tooth restoration. By registering low temperatures, increasing irradiation time, and low intensities, diode lasers are highly effective in phototherapy treatment.

References

[1] E. Berutti, M. Riccardo and A. Alessandra, "Penetration ability of different irrigants into dentinal tubules", *J. Endodontics*, 23(12) (1997) 725-727.

[2] C. Fornaini et al., "405 nm diode laser, halogen lamp and LED device comparison in dental composites cure: an "in vitro" experimental trial", *Laser Therapy*, 24(4) (2015) 265-274.

[3] M. Yacoob et al., "Mathematical Study for laser and its Clinical Applications in dentistry: Review and Outlook", *J. Phys.: Conf. Ser.*, 1660(1) (2020) 012101.

[4] J. Boulnois, "Photophysical processes in recent medical laser developments: a review", *Lasers in Med. Sci.*, 1 (1986) 47-66.

[5] H. Hatayama, I. Akira and K. Junji, "Study on use of blue-violet laser diode module as dental/oral surgical device", *Sei Tech. Rev. (English ed.)*, 66 (2008) 142.

[6] S. Verma et al., "Laser in dentistry: An innovative tool in modern dental practice", *Nat. J. Maxillofacial Surg.*, 3(2) (2012) 124.

[7] M. Sulieman, "An overview of bleaching techniques: 3. In-surgery or power bleaching", *Dental Update*, 32(2) (2005) 101-108.

[8] M. Sulieman, M. Addy and S. Rees, "Surface and intra-pulpal temperature rises during tooth bleaching: an in vitro study", *British Dent. J.*, 199(1) (2005) 37-40.

[9] A. Braun, B. Michael and F. Roland, "The 445-nm semiconductor laser in dentistry introduction of a new wavelength", *Quintessenz*, 66(2) (2015) 205-211.

[10] D. Diehl and L. Diehl. **"High-Power Diode Lasers: Fundamentals, Technology, Applications"**, 78 Springer Science & Business Media (2000).

[11] S. Mirsasaani, M. Mohammad and M. Mohammad, "Photopolymerization of a dental nanocomposite as restorative material using the argon laser", *Lasers in Med. Sci.*, 26 (2011) 553-561.

[12] R. Strang et al., "*in vitro* temperature rises produced by five polymerising light sources", *Restor. Dent.*, 4(2) (1988) 33-35.

[13] M. Hannig and B. Bott, "*in-vitro* pulp chamber temperature rise during composite resin polymerization with various light-curing sources", *Dent. Mater.*, 15(4) (1999) 275-281.

[14] M. Yacoob, K. Raed and Y. Muna, "Use of Multi-Response Logistic Regression to Determine the Factors Affecting the Radiation Values of Light-Curing Units in Private Dental Clinics in Erbil", *Iraqi J. Sci.*, (2022) 4721-4732.

[15] T. Yoon et al., "Degree of polymerization of resin composites by different light sources", *J. Oral Rehabil.*, 29(12) (2002) 1165-1173.

[16] F.M. Hamam, B.A.M. Bader and M.Y. Slewa, "Evaluation of Mechanical Properties for Selected Dental Composite Resin Polymerized by Light Curing Technology at Different Thickness", *Mater. Sci. Forum*, 1002 (2022) 331-339.

[17] J. Harlow et al., "Characterizing the output settings of dental curing lights", *J. Dentistry*, 44 (2016) 20-26.

[18] C. Shimokawa et al., "Ability of four dental radiometers to measure the light output from nine curing lights", *J. Dentistry*, 54 (2016) 48-55.

[19] C. Shortall et al., "Advances in light-curing units: four generations of LED lights and clinical implications for optimizing their use: Part 2. From present to future", *Dent. Update*, 39(1) (2012) 13-22.

[20] A. Rueggeberg et al., "Light curing in dentistry and clinical implications: a literature review", *Braz. Oral Res.*, 31(Suppl. 1) (2017).

 ISSN (print) 1813-2065, (online) 2309-1673

IRAQI JOURNAL OF APPLIED PHYSICS
Vol. 19, No. 3B, September 2023, pp. 39-42

Malik H. Kheder[1]
Thoalfiqar A. Zakar[1]
Ahmed T. Abdulhameed[1]
Mushtaq A. Dawood[2]

[1] *Department of Physics, College of Education, University of Al-Hamdaniya, Ninawa Province, IRAQ*
[2] *Department of Physics, College of Education for Pure Sciences, University of Mosul, Mosul, IRAQ*

Effect of Laser Power on Optical Properties of CN-85 Nuclear Track Detector

The effect of a diode laser on the optical properties of a thin CN plastic detector was investigated. A laser with a wavelength of (632 nm) and different operating currents were used to control the power of the laser beam falling on the CN detector. The relationship between the laser's operating current and the intensity measured by the photodetector in the absence of a detector, with a detector that has not been exposed to radiation, and with a number of detectors that have been exposed to radiation with various energies and alpha particles from the americium source (2.3, 3.0, 3.5, 4) MeV in order to research how the photodetector's detector absorption affects the laser intensity detection. Intensity through the detector is reduced as irradiation with alpha particles is increased, increasing the detector's absorption and quenching coefficient.

Keywords: Optical properties; Diode laser; CN detector; Laser beam
Received: 11 March 2023; Revised: 24 March 2023; Accepted: 31 March 2023

1. Introduction

The cellulose nitrate detector is a type of organic reagent having the chemical formula $(C_6H_8N_2O_5)_n$ with a chemical makeup that includes carbon, hydrogen, and nitrogen. It is regarded as one of the materials with excellent efficiency in detecting fission fragments as well as thermal and rapid neutron doses. It is used to determine radon flow and uranium contents. Protons, detrons, and alpha particles are among the charged particles that can be detected using it [1, 2]. Since some materials change color when exposed to radiation and heating, optical absorbance is used to calculate the radiation dose from ionizing radiation (such as gamma rays, neutrons, charged particles, etc.). For instance, a detector's color changes and tends to turn yellow at high temperatures, but glass samples exposed to gamma rays will change to a blueish hue. When heated, these samples lose their brown color. The absorption coefficient and the value of the energy gap are both determined using optical absorbance [3-5]. The analysis of the thermal luminescence spectra and the understanding of the damage centers that happen when the single crystals are heated or exposed to ionizing radiation both make use of the optical absorption spectra [6. 7]. There are three sorts of bonds: metallic, ionic, and covalent, and the radiation causes more damage in the particles of the substance on which it falls. Compared to its impact on other bonds, radiation has a greater impact on covalent bonds [8]. The influence of radiation is significant since it was in those reagents because organic reagents are made up of molecules joined by covalent bonds. The penetration of the particles into the nuclear trace detectors, including a detector, causes the dissociation of the long polymeric chains, which results in the production of free radicals at the impact of the falling particle. The particles affect the weak group in the polymer, which is unstable, and because the group is present, oxygen with carbon atoms acts as a catalyst in breaking the bond. This cycle is repeated [9-11]. In addition to playing a significant part in creating the polymer structure, it also plays an essential part in decomposition and the beginning of new decompositions, which lowers the polymer's thermal stability. The polymer undergoes physical and chemical modifications as a result of the produced free radicals, resulting in a polymer with broken short chains and a drop in the molecular weight of the polymer. Free radicals entering certain processes may cause the polymer to crosslink, increasing its molecular weight [12-17].

In this study, a solid-state laser with a wavelength of 632 nm and various operating currents were used to explore some of the optical features of the CN detector and adjust the power of the laser beam impinging on it.

2. Experimental Work

The samples used in our study were CN-85 nuclear trace detectors with a thickness of (100 μm) and a cut area of (1 cm^2), and they were exposed to alpha particles using the element americium, which has a half-life of (432 years), for seven minutes at various energies (2.3, 3.0, 3.5, and 4) MeV using a special holder. The energies were calculated for each of these dimensions. Using a solid-state laser with a wavelength of (632 nm) and various operating currents to regulate the power of the laser beam falling on the CN detector, some of the optical features of this detector were investigated. where the laser's strength and intensity were measured using a photodetector and sent through the CN detector.

When a radiation of intensity (I_o) falls on the surface of a material of thickness (t), the radiation of intensity (I) will escape from the other side, and the intensity (I) will be less than the incident (I_o) due to absorption and scattering within the material and reflection from its surface. The model's absorption process is the primary factor in reducing the intensity [18].

$$I = I_o \, exp\,(-\alpha t) \quad (1)$$

where alpha denotes the absorption coefficient, which is a property of the substance. The absorbance A is [19].

$$A = Log \ \frac{I_o}{I} \quad (2)$$

Based on the determined absorption coefficient from the subsequent relationship [20].

$$\alpha = 2.303 \ \frac{A}{t} \quad (3)$$

The amount of energy that is absorbed by the medium's electrons from the energy of the incident radiation photons is known as the quenching coefficient [21,22].

$$K_o = \frac{\alpha\lambda}{4\pi} \quad (4)$$

3. Results and Discussion

The relationship between the intensity measured by the photodetector and the amount of operating current for the laser without a detector, in the presence of a non-irradiated detector, and in the presence of a number of detectors irradiated with alpha particles and different energies was conducted and studied to better understand the characteristics of the laser used in the study of the optical properties of the CN trace detector.

The results of applying current to the laser and measuring the intensity transmitted through the plastic detector are shown in table (1) and Fig. (1). We observe that the intensity transmitted through the detector decreases as the energy of the alpha particles used to irradiate it rises to 3.5 MeV, and then it begins to rise again. This phenomenon is due to the fact that higher doses of radiation cause more damage to the metallic, ionic, and covalent bonds found in the metallic, ionic, and covalent bonds that the detector is exposed to. Compared to its impact on other bonds, radiation has a greater impact on covalent bonds.

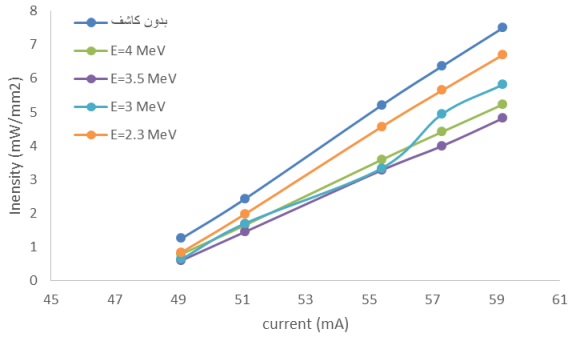

Fig. (1) The relations of applied currents and measured intensity

Table (1) The applied current of laser and measured intensity of different irradiation energies

Current (mA)	I (mW/mm²)					
	Without detector	$E_\alpha = 0$	$E_\alpha = 2.3\ MeV$	$E_\alpha = 3\ MeV$	$E_\alpha = 3.5\ MeV$	$E_\alpha = 4\ MeV$
49.1	1.25	0.65	0.84	0.64	0.6	0.79
51.1	2.43	1.52	1.98	1.7	1.45	1.65
55.4	5.21	2.8	4.57	3.34	3.28	3.59
57.3	6.37	4.34	5.65	4.95	4	4.42
59.2	7.5	5.12	6.7	5.82	4.82	5.23

The effect of radiation is significant since it was in those reagents because organic molecules are joined together by covalent bonds. The penetration of the particles into the nuclear trace detectors, including a detector, causes the dissociation of the long polymeric chains, which results in the production of free radicals at the impact of the falling particle. The particles affect the weak group in the polymer, which is unstable, and because the group is present, oxygen with carbon atoms acts as a catalyst in breaking the bond. This cycle is repeated. In addition to playing a significant part in creating the polymer structure, it also plays an essential part in decomposition and the beginning of new decompositions, which lowers the polymer's thermal stability. The molecular weight of the polymer decreases as the produced free radicals engage in transformations that cause physical and chemical changes in the polymer. This results in a polymer with broken short chains. In some processes, the presence of free radicals can cause the polymer to crosslink, increasing its molecular weight. The detector becomes stronger, harder, and heavier as a result of the complex network structure that results from this interconnection. When the polycarbonate surface was exposed to the laser, the surface particles interlocked, hardened, and re-adhered to one another. As a result, the amount of laser light that passes through the detector is reduced, and absorption is increased. The same is true for the relationship between laser power and alpha particle energy, as shown in table (2), Fig. (2) and the absorption with alpha particles energy shown in table (3), Fig. (3) and the quenching coefficient with alpha particles energy shown in table (4), Fig. (4).

Table (2) The irradiation energy and the measured power for applied currents

E_α (MeV)	P (mW)				
	I= 49.1 mA	I= 51.1 mA	I=55.4 mA	I=57.3 mA	I=59.2 mA
4	0.51	1.06	2.3	2.83	3.35
3.5	0.39	0.93	2.1	2.56	3.09
3	0.41	1.09	2.14	3.17	3.73
2.3	0.54	1.27	2.93	3.62	4.29

Table (3) The measured absorption with irradiated energy for applied laser current

E_α (MeV)	Abs.				
	I= 49.1 mA	I= 51.1 mA	I=55.4 mA	I=57.3 mA	I=59.2 mA
4	0.19	0.168	0.165	0.158	0.156
3.5	0.31	0.22	0.2	0.202	0.192
3	0.29	0.15	0.193	0.109	0.11
2.3	0.17	0.08	0.056	0.052	0.048

 ISSN (print) 1813-2065, (online) 2309-1673

Table (4) The irradiation energy with the quenching coefficient for each laser current

E_α (MeV)	$k_o \times 10^{-6}$				
	I= 49.1 mA	I= 51.1 mA	I=55.4 mA	I=57.3 mA	I=59.2 mA
4	216.3	194.2	190.7	182.6	180.6
3.5	358.7	254.6	231.4	233.9	222.4
3	335.6	173.5	223.4	126.2	127.3
2.3	196.7	92.5	64.4	59.8	55.3

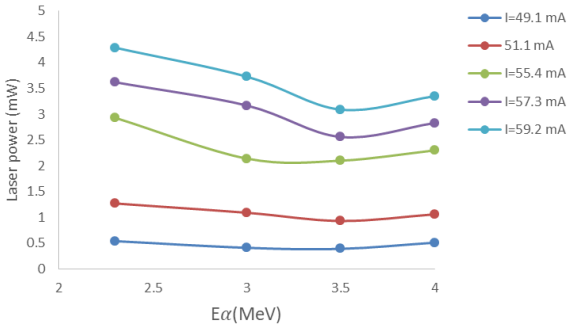

Fig. (2) The relationship between laser power and irradiation energy

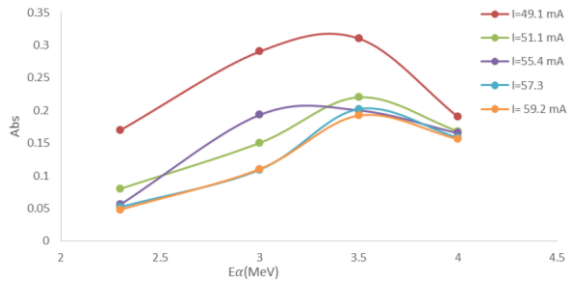

Fig. (3) The relation of absorption with irradiation energy for each laser current

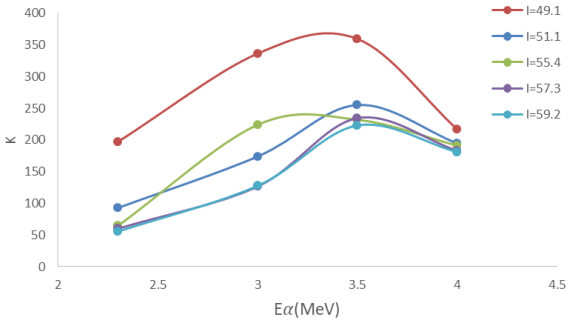

Fig. (4) The irradiation energy with the quenching coefficient for each laser current

4. Conclusions

In this study of the optical properties of the CN trace detector using the laser, the relationship between the intensity measured by the photodetector and the amount of operating current for the laser without a detector and in the presence of a non-irradiated detector and a number of detectors irradiated with alpha particles and different energies was conducted and studied. The intensity transmitted through the detector decreases with the increase in the energy of the alpha particles. The intensity of the laser's detector is absorbed more quickly as alpha particle exposure is increased. A drop in laser intensity through the detector and an increase in absorption were seen after exposing the polycarbonate surface to the laser. This was due to the surface particles interlocking and hardening as well as the particles' and free radicals' re-adhesion with one another.

References

[1] O. Deutschmann et al., "Heterogeneous Catalysis and Solid Catalysts, 1. Fundamentals", In Ullmann's Encyclopedia of Industrial Chemistry (2011).

[2] A.K. Hashim et al., "Comparison study of CR-39 and CN-85 detectors to evaluate the alpha radioactivity of some samples of drinks in Iraq", *Appl. Rad. Isotop.*, 167 (2021) 109410.

[3] R.A.P. Oliveira et al., "Radiation Detection Using The Color Changes Of Lilac Spodumene", 2009 Int. Nucl. Atlantic Conf. (INAC 2009), Rio de Janeiro (Brazil), September 27 to October 2, 2009.

[4] K. Linas et al., "Investigation of Colored Film Indicators for the Assessment of the Occasional Radiation Exposure", *Gels*, 9(3) (2023) 189.

[5] F. Ravotti, "Dosimetry Techniques and Radiation Test Facilities for Total Ionizing Dose Testing", *IEEE Trans. on Nucl. Sci.*, 65(8) (2018).

[6] B. Savoini et al., "Radiation damage in neutron-irradiated yttria-stabilized-zirconia single crystals", *J. Nucl. Mater.*, 277(2-3) (2000) 199-203.

[7] B.W. Morgan et al., "Optical Absorption of Fused Silica and Sapphire Exposed to Neutron and Gamma Radiation with Simultaneous Thermal Annealing", *J. Nucl. Mater.*, 570 (2022) 153945.

[8] E.S. Kempner, "Direct Effects of Ionizing Radiation on Macromolecules", *J. Polym. Sci. B: Polym. Phys.*, 49(12) (2011) 827-831.

[9] C. Vasile, E. Butnaru and P. Poni, "Radiation Chemistry Of Organic Solids", Inst. Macromol. Chem., Romanian Academy (Romania).

[10] A. Ashfaq et al., "Polymerization Reactions and Modifications of Polymers by Ionizing Radiation", *Polymers (Basel)*, 12(12) (2020) 2877.

[11] L. Wojnárovits, **"Radiation Chemistry"**, in Handbook of Nuclear Chemistry, A. Vértes, S. Nagy, Z. Klencsár, R.G. Lovas, F. Rösch, (eds), Springer (MA, 2011).

[12] A. Witkowski, A. Stec and T. Hull, **"Thermal Decomposition of Polymeric Materials"**, in SFPE Handbook of Fire Protection Engineering, Springer (NY, 2016).

[13] K. Landfester, "Miniemulsion Polymerization and the Structure of Polymer and Hybrid Nanoparticles", *Angewandte Chemie Int. Ed.*, 48 (2009) 4488-4507.

[14] R. Lyubushkin et al., "Renewable Polymers Derived from Limonene", *Chem. Eng.*, 7(1) (2023) 8.
[15] A. Samir et al., "Recent advances in biodegradable polymers for sustainable applications", *npj Mater. Degrad.*, 6(68) (2022).
[16] B. Jaleha et al., "KrF laser irradiation effects on nuclear track recording properties of polycarbonate", *Radiat. Measur.*, 38(2) (2004) 173-183.
[17] K.C.C. Tse, D. Nikezic and K.N. Yu, "Effects of UVC irradiation on alpha-particle track parameters in CR-39", *Radiat. Measur.*, 43(S1) (2008) S98-S101.
[18] F. Priamo et al., "Linear attenuation coefficient. Reference article", *Radiopaedia.org* (2023).
[19] A.S. Jasim, "Preparation and Optical Characterization of Polymer Composites Reinforced by Natural Materials", *J. Al-Nahrain Univ.*, 19(1) (2016) 91-97.
[20] A.N. Alias et al., "Optical Characterization and Properties of Polymeric Materials for Optoelectronic and Photonic Applications", *Int. J. Appl. Sci. Technol.*, 3 (5) (2013).
[21] S.M. Sze and K. Kwong, **"Physics of semiconductor devices"**, 3rd ed., John Wiley & Sons, Inc. (NJ, 2007).
[22] A. Ibrahim, R. Al-Rawie and I. Agool, "Optical Properties of Obliquely Evaporated Manganese Films", *Ibn Al-Haitham J. Pure Appl. Sci.*, 26 (3) (2013) 129-135.

 ISSN (print) 1813-2065, (online) 2309-1673

IRAQI JOURNAL OF APPLIED PHYSICS
Vol. 19, No. 3B, September 2023, pp. 43-46

Effect of Substrate and Annealing Temperature on Hall Effect and Activation Energy of $CuISe_2$ Compound

Muayyad N. Fathula[1]
Azhaar A. Ali[1]
Muna Y. Slewa[2]

[1] *Department of Electronic and Control Engineering, Technical College, Northern Technical University, Kirkuk, IRAQ*
[2] *Department of Physics, College of Education, University of Al-Hamdaniya, Nineveh, IRAQ*

Polycrystalline $CuISe_2$ thin films were deposited on glass substrate. The Hall effect discovered in the prepared films at various substrate and annealing temperatures, investigates the type of carriers, carrier concentration, and Hall mobility at room temperature. The thin films were n-type, the Hall mobility had the highest value (36.45 $cm^2/V.s$) for films prepared with substrate temperature of 150°C and annealing temperature of 200°C and the lowest value (6.08 $cm^2/V.s$) for films prepared films with substrate temperature of 350°C and annealing temperature of 400 °C (thickness of 1200Å). It was found that the substrate and annealing temperatures have changed the Hall mobility and carrier concentration.

Keywords: $CuIS_2$; Hall effect; Structural activation; Activation energy; Annealing
Received: 11 March 2023; Revised: 24 March 2023; Accepted: 31 March 2023

1. Introduction

Recently, the preparation of structured I-II.VI, ternary compound semiconducting materials has been one of the important methods for studying the physical properties of these materials, and has played an important role in solid state physics research as well as advanced technical applications [1-5]. Due to their expanding range in the industry, they are utilized in current technological applications through the manufacture sold state technology, including photovoltaic cells, electronic components, photoconductors, sensors, and solar coating [6-9]. $CuGaS_2$, $CuGaSe_2$, and $CuAlSe_2$ are three of the I-III-VI compounds that are quite significant. These are tripartite compounds with chalcopyrite structures similar to sphalerite structures, which are referred to as (zincblende) [10,11]. Because the chalcopyrite atoms' locations are similar to those of the diamond atoms, each type forms a face-centered cubic lattice network [12]. The conductivity of nonmetal and semiconductor crystals can be calculated by knowing the change in activation energy (of electrons) with temperature, then (273°C) electrons are bound to the atoms that make up the semiconductor crystal lattice, and as the temperature rises [13,14]. Because the energy of some electrons can escape from covalent bonds due to thermal fluctuation is greater than the activation energy of the intrinsic semiconductor, the number of freely moving electrons under the influence of the electric field increases, and thus the conductivity of the semiconductor increases with temperature [15,16]. There is no completely free electron or hole (273°C) if the semiconductor contains donor or acceptor impurities. The electrons of the semiconductor atoms are ionized, which causes the impurity atoms to be ionized [17,18]. As the temperature rises, self-conductivity becomes more important because the electrons of the valence band will require a sufficient amount of thermal energy to cross the energy gap as the impurity centers run out, allowing packet electron conduction [19,20].

The purpose of this work is to determine the impact of substrate temperature and annealing on the fluctuation of the Hall effect and activation energy of the chemical ($CuISe_2$).

2. Experimental Work

The $CuISe_2$ films were deposited on soda glass substrates using the thermal evaporation coating technique before beginning membrane deposition ($CuISe_2$) with a boat of molybdenum (Mo), when the pressure is reduced (10^{-6} mbar), we begin the process of heating the tank by gradually passing continuous current through the tank, and the material begins to evaporate at a constant rate (2Å/s) to achieve the film thickness (1200-1400Å). As a result, we obtained the membrane during the preparation process at room temperature. The floors are heated to different temperatures during the deposition process in order to obtain the preparation process at different deposition temperatures.

A Phillips X-ray diffractometer (XRD) was used to inspect the $CuISe_2$ films in the angle range 15-70° after they had been prepared to ensure their formation. The optical interference technique and a quartz crystal monitor were used to determine the thickness of the film before it was deposited [21], and the film's electrical conductivity was measured using a Philips DC power supply (40V, 1A), a digital electrometer, electronic thermometer, resistance box, and a cryostat (Leybold vacuum unit of turbo and rotary pumps LTC 60).

The Hall experiment was designed to determine the type of conductivity of membranes and to calculate Hall's factor, charge concentration, and carriers' mobility.

3. Results and Discussion

The crystalline structure of the prepared $CuISe_2$ alloy was confirmed by the XRD results in accordance with the ASTM cards [22]. For semiconductors, the change in electrical conductivity with temperature is described by the following relationship [23]:

$$\sigma = \sigma_o e^{-E_a/kT} \quad (1)$$

where E_a is the thermal activation energy, T is the temperature in Kelvin, k is the Boltzmann's constant, and σ_o represents the conductivity when the temperature is extremely high [24,25]

The presence of crystal grain boundaries complicates the situation in polycrystalline films, as the size of the grains and the natural barriers that form at the grain boundaries affect the movement of charge carried through the film. Polycrystalline films are effectively affected by potential barriers at the grain boundaries. As a result, the conductivity of these films is represented by the following equation [22]:

$$\sigma = en\mu_o e^{-e\varphi_b/kT} \quad (2)$$

where $e^{-e\varphi_b/kT}$ represents the effective mobility, μ_0 is the mobility of N_0 the single crystal, and $e\varphi_b$ is the height of the grain potential barrier [26]

The Hall effect is a standard tool for studying the mobility and type of charges in materials by measuring the Hall potential difference (V_H) and Hall's coefficient, as shown in the following equation [27]:

$$R_H = V_H/I \times t/B \quad (3)$$

where t is the conductor thickness and B is the magnetic field produced by the current flowing through the conductor

The R_H sign in Eq. (3) is negative for n-type semiconductors and positive for p-type semiconductors. The Hall mobility can be expressed as [28]:

$$\mu_H = R_H.\sigma \quad (4)$$

Table (1) displays the electrical conductivity values at room temperature with the first activation energy E_{a1} at each T_s, while table (2) displays the electrical conductivity values at room temperature with the second activation energy E_{a2} at each T_s.

Table (1) Values of electrical conductivity at room temperature with the first activation energy (E_{a1}) at each T_s

T_s (°C)	σ (Ω.cm)$^{-1}$ @ R.T.	E_{a1} (eV)	Temperature range (°C)
150	17.6 ± 0.2	0.0184 ± 0.002	- 120 to - 40
200	14.3 ± 0.15	0.0308 ±0.002	- 120 to - 30
300	2.97 ± 0.09	0.0655 ± 0.003	- 110 to - 35
350	1.6 ± 1.0	0.076 ± 0.002	- 62 to - 10

Tables (1) and (2) distinguish the two activation energies; the second activation energy ranges in degrees of the first activation energy. Figures (1) and (2) show how the electrical conductivity of $CuISe_2$ films changes with temperature when prepared and annealed at substrate temperature ranging from 150 to 350°C and annealing temperature from 200 to 400°C. The appearance of the electrical properties of $CuISe_2$ films is the source of detects (negative defects) caused by deviation from the pure structure. Figures (4-7) show how Hall effect measurements were used to determine the type of charge carriers in $CuISe_2$ films prepared at various temperatures.

Table (1) Values of electrical conductivity at room temperature with the second activation energy (E_{a2}) at each T_s

T_s (°C)	σ (Ω.cm)$^{-1}$ @ R.T.	E_{a2} (eV)	Temperature range (°C)
150	17.6 ± 0.2	0.032 ± 0.001	- 40 to 30
200	14.3 ± 0.15	0.00575 ±0.0015	- 30 to 25
300	2.97 ± 0.09	0.0938 ± 0.0014	- 50 to 34
350	1.6 ± 1.0	0.097 ± 0.0025	- 10 to 30

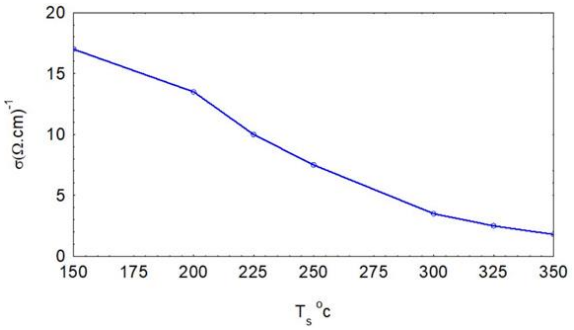

Fig. (1) Variation of electrical conductivity of the prepared films with substrate temperature

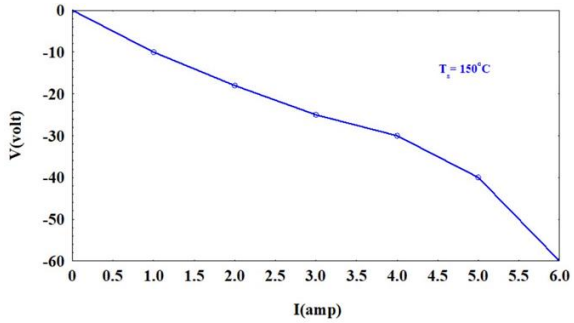

Fig. (2) Variation of the Hall voltage with current at T_s=150°C

The outcomes were presented using tables (1) and (2), as deposition temperature increases, the relationship between the density of charge carriers (n) and T_s and T_a decreases. The Se atom and the vacuum created by removing the Se atom will both leave two weakly bonded electrons, resulting in this vacuum being a double donor. At room temperature, the electrons are insufficient for the electron to jump to the conduction beam, but mobility decreases as T_s increases for the same reason mentioned above [29-32].

The reason for the decrease in charge carrier concentration with increasing T_s and atomic structure shift, and thus the energy of electrons below room

 ISSN (print) 1813-2065, (online) 2309-1673

temperature is insufficient for jumping into the conduction beam with increasing T_s when preparing and for the same reason as above.

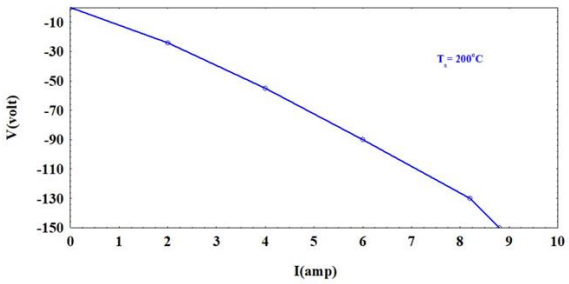

Fig. (3) Variation of the Hall voltage with current at T_s=200°C

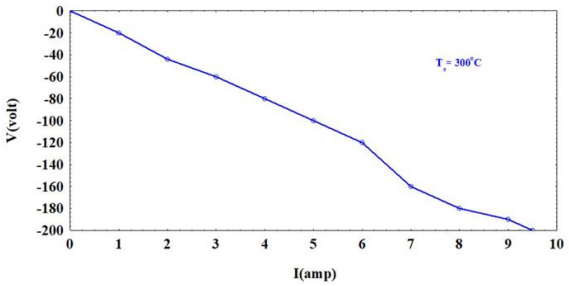

Fig. (4) Variation of the Hall voltage with current at T_s=300°C

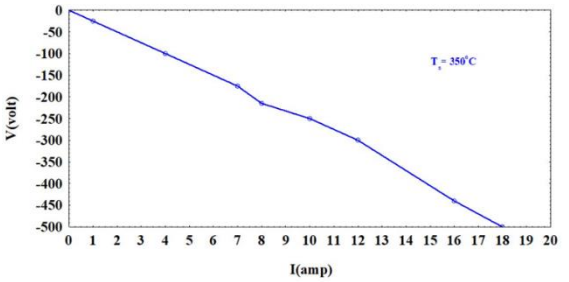

Fig. (5) Variation of the Hall voltage with current at T_s=350°C

4. Conclusions

Taking into account the findings of this study, it is possible to draw the following conclusions. The electrical conductivity was defined by two activation energies at different substrate and annealing temperatures. Based on Hall-effect investigations of the type of carriers, carrier concentration, and Hall mobility at room temperature, the thin film was determined to be of the n-type. We found the highest value of the carrier concentrate for films prepared at T_s=150°C with the deposit thickness t=1200Å, and lowest value for films at temperature 350°C with the same thickness. The Hall mobility was highest for films prepared with substrate and annealing temperatures of T_s=150°C and T_a=200°C, and lowest for films prepared with substrate and annealing temperatures of 350°C and 400°C, respectively, for films prepared at t=1200Å.

References

[1] R.A. Ismail et al., "Characterization of Si p-n Photodetectors Produced by Laser-Induced Diffusion", *Int. J. Mod. Phys.*, 19(31) (2005) 4619-4628.

[2] O.A. Hamadi, "Characteristics of CdO-Si Heterostructure Produced by Plasma-Induced Bonding Technique", *Proc. IMechE, Part L, J. Mater.: Design & Appl.*, 222 (2008) 65-71.

[3] R.A. Ismail et al., "Full characterization at 904 nm of large area Si p-n junction photodetectors produced by LID technique", *The Euro. Phys. J. – Appl. Phys.*, 38(3) (2007) 197-201.

[4] A.A.K. Hadi and O.A. Hamadi, "Optoelectronic Characteristics of As-doped Si Photodetectors Produced by LID Technique", *Iraqi J. Appl. Phys. Lett.*, 1(2) (2008) 23-26.

[5] O.A. Hamadi and K.Z. Yahiya, "Optical and electrical properties of selenium-antimony heterojunction formed on silicon substrate", *Sharjah Univ. J. Pure Appl. Sci.*, 4(2) (2007) 1-11.

[6] D.O. Scanlon and G.W. Watson, "Stability, geometry, and electronic structure of an alternative I-III-VI_2 material, $CuScS_2$: A hybrid density functional theory analysis", *Appl. Phys. Lett.*, 97(13) (2010) 131904.

[7] B.A. Bader et al., "Photodetector Based on Titanium Oxide Nanoparticles Produced via Pulsed Laser Ablation", *Adv. Cond. Matter Phys.*, (2022) article ID 8066167.

[8] A. Amara et al., "Electrical and optical characterisation of $CuInS_2$ crystals and polycrystalline coevaporated thin films", *Solar Ener. Mater. Solar Cells*, 91(20) (2007) 1916-1921.

[9] C. Rincon et al., "Optical properties and characterization of $CuInSe_2$", *Solar Cells*, 16 (1986) 335-349.

[10] M.J. Romero et al., "Comparative study of the luminescence and intrinsic point defects in the kesterite Cu_2ZnSnS_4 and chalcopyrite $Cu(In,Ga)Se_2$ thin films used in photovoltaic applications", *Phys. Rev. B*, 84(16) (2011) 165324.

[11] O.A. Hammadi, "Electrical and Spectral Characteristics of Visible-Blind ZnO/Si Heterojunction Fabricated by Plasma-Induced Bonding", *J. Optoelctron. Photon.*, 7(5) (2016) 21-24.

[12] A.K. Yousif and O.A. Hamadi, "Plasma-Induced Etching of Silicon Surfaces", *Bulg. J. Phys.*, 35(3) (2008) 191-197.

[13] O.A. Hamadi, "Effect of Annealing on the Electrical Characteristics of CdO-Si Heterostructure Produced by Plasma-Induced Bonding Technique", *Iraqi J. Appl. Phys.*, 4(3) (2008) 34-37.

[14] O.A. Hamadi, B.A.M. Bader and A.K. Yousif, "Electrical Characteristics of Silicon p-n Junction Solar Cells Produced by Plasma-Assisted Matrix Etching Technique", *Eng. Technol. J.*, 28 (2008).

[15] M.I.F. Ahmed, "Study of effect of temperature and doping of mobility of charge carriers on semiconductors", PhD dissert., Sudan University of Science and Technology (2015).
[16] O.A. Hamadi, "Profiling of Antimony Diffusivity in Silicon Substrates using Laser-Induced Diffusion Technique", *Iraqi J. Appl. Phys. Lett.*, 3(1) (2010) 23-26.
[17] A.S.A. Rawas et al., "Physical characterization of nickel doped nanostructured TiO_2 thin films", *J. Green Eng.*, 10 (2020) 7141-7153.
[18] O.A. Hamadi, N.J. Shakir and F.H. Mohammed, "Magnetic Field and Temperature Dependent Measurements of Hall Coefficient in Thermal Evaporated Tin-Doped Cadmium Oxide Thin Films", *Bulg. J. Phys.*, 37(4) (2010) 223-231.
[19] X. Huang, J. Li, "From single to multiple atomic layers: A unique approach to the systematic tuning of structures and properties of inorganic−organic hybrid nanostructured semiconductors", *J. Am. Chem. Soc.*, 129(11) (2007) 3157-3162.
[20] B.A.M. Badr, O.A. Hamadi and A.K. Yousif, "Measurement of thermooptic coefficient of semiconductors by single-beam scanning technique", *Eng. Technol. J.*, 27(5) (2007).
[21] Y. Lu et al., "Good performance and flexible PEDOT: PSS/Cu_2Se nanowire thermoelectric composite films", *ACS Appl. Mater. Interf.*, 11(13) (2019) 12819-12829.
[22] M. West et al., "Atomic spectrometry update-X-ray fluorescence spectrometry", *J. Anal. Atom. Spectro.*, 26(10) (2011) 1919-1963.
[23] O.A. Hammadi and M.S. Edan, "Temperature Dependencies of Refractive Index and Optical Elasticity Coefficient on Lens Induced in Nd:YAG Crystal", *Iraqi J. Appl. Phys.*, 8(1) (2012) 35-41.
[24] F. Steiner et al., "Influence of orientation mismatch on charge transport across grain boundaries in tri-isopropylsilylethynyl (TIPS) pentacene thin films", *Phys. Chem. Chem. Phys.*, 19(17) (2017) 10854-10862.
[25] E. Sheha et al., "Structure, dielectric and optical properties of p-type (PVA/CuI) nanocomposite polymer electrolyte for photovoltaic cells", *Optik*, 123(13) (2012) 1161-1166.
[26] R. Kilmurray, "Investigating the AC Hall effect as a characterisation tool for organic semiconductors", PhD thesis, Imperial College London (2019).
[27] Z. Yu et al., "Properties of different temperature annealed Cu(In,Ga)Se_2 and Cu(In,Ga)$_2Se_{3.5}$ films prepared by RF sputtering", *Appl. Surf. Sci.*, 261 (2012) 353-359.
[28] N.F. Mott and E.A. Davis, **"Electronic Processes in Non-crystalline Materials"**, Oxford University Press (2012).
[29] R. Horiba et al., "Growth and properties of vacuum deposited $CdIn_2S_4$ films", *Surf. Sci.*, 86 (1979) 498-503.
[30] S.D. Kang, M. Dylla and G.J. Snyder, "Thermopower-conductivity relation for distinguishing transport mechanisms: Polaron hopping in CeO_2 and band conduction in $SrTiO_3$", *Phys. Rev. B*, 97(23) (2018) 235201.
[31] H. Ahmadi Moghadam and M.H. Paydar, "Investigation of Sm_2O_3 additive on mechanical and electrical properties of Li_2O-stabilized β ″-alumina electrolyte", *Int. J. Appl. Cer. Technol.*, 14(6) (2017) 1183-1189.
[32] K. Ide et al., "Electronic defects in amorphous oxide semiconductors: A review", *phys. stat. sol. (a)*, 216(5) (2019) 1800372.

 ISSN (print) 1813-2065, (online) 2309-1673

IRAQI JOURNAL OF APPLIED PHYSICS
Vol. 19, No. 3B, September 2023, pp. 47-50

Study the Effect of Molar Concentrations on the In_2S_3/Si Photodetector Performance

Kawkab D. Salim
Niran .F. Jabar

Department of Physics, College of Education for Pure Sciences, Tikrit University, Tikrit, IRAQ

The effect of molar concentration on the performance of the In_2S_3/Si photodetectors prepared by thermal chemical spray technique was studied in this work. The characteristics of photodetectors include the I-V in dark using the forward and reverse bias conditions, were also investigated. The n-In_2S_3/p-Si heterojunction is an asymmetric. The ideal factor (n) was found to be greater than one and decreasing with increasing molar concentration. The spectral responsivity of the prepared photodetectors was also studied. The results showed it has two peaks, the highest value 0.8 A\W at wavelength of 450 nm and 1.05 A\W at wavelength of 700 nm. Specific detectivity of $2.38x10^{11}$ cm.$Hz^{1\2}$/W was determined and the value of quantum efficiency was 3.5%.

Keywords: Photodetectors; Indium sulphide; Molar concentration; Spectral response
Received: 11 March 2023; Revised: 24 March 2023; Accepted: 31 March 2023

1. Introduction

Indium sulfide (In_2S_3) has interesting photoluminescence properties and it was used in many applications in optoelectronic devices due to its wide band gup and photoconductive behavior, which makes it promising candidate for many technological applications [1,2]. Heterojunctions are important devices because of their wide applications in many electrical devices such as solar cells and photodetectors [3-8]. It is defined as a contact between two semiconducting materials those are different in their energy gap, dielectric constant, electronic affinity and work function [9]. There is also a difference in the lattice constants called lattice mismatch [10-12]. Junctions are classified into abrupt and gradient depending on the distance through which the transitions from one of the two materials to the other is carried out [13]. Also, heterojunctions are classified according to their sides. If the same type of connection appears, it is called isotype heterojunction (p/p and n/n). Otherwise, it is called anisotype heterojunction (p/n or n/p) [14].

There are many techniques for preparing the heterojunctions, including the chemical spray pyrolysis (CSP), molecular weight spray pyrolysis (MWSP), chemical bath deposition (CBD), vacuum thermal deposition (VTD) [15-17]. The properties of the heterojunction are functions of the preparation method, which is related to the exact composition [18]. Heterojunctions have been used in the manufacture of many semiconductor devices such as solar cells, high efficient transistors, photodetectors, semiconductor lasers and other applications [19].

2. Experimental Work

Indium sulfide (In_2S_3) thin films were deposited on single-crystal p-type silicon wafers with a crystalline directional of (111), electrical resistivity of 5 Ω.cm, thickness of 400 µm, area of 1 cm^2 and the mirror surface thin films were obtained by using thermal chemical spraying technique (CSP). Indium chloride ($InCl_2$) in the form of white powder with a molecular weight 221.18 g\mol and purity of 99.9% was used as a source of indium ions and is easily dissolved in water. Thiostamide $(CS(NH_2))_2$ with a molecular weight of 75.13 g\mol was also used. The thin films were prepared with different molar concentrations (0.05, 0.15, and 0.2 M) at temperature of 310°C with spraying time of 3 minutes and stop period of 15 minute to reach the same temperature for each spray after 12 sprays.

3. Results and Discussion

The forward and reverse bias conditions were used at an applied voltage of -1.5 to 1.5V. The highest value of the forward current was recorded at concentration of 0.2 M. The behavior of the forward current in the dark condition was close to the exponential function. The diffusion current dominated the recombination current and the current flowing through the junction increased with increasing applied voltage. This increase arises because the difference in the applied voltage works to inject the majority carries, resulting in a decrease in the built-in potential as well as in the width of the depletion region .In case of reverse bias, as shown in Fig. (1), the reverse bias current was low due to the low values of the applied voltage as well as the

increase in the width of depletion region and decrease in the concentration of carriers.

Table (1) The values of ideal factor

Ideality factor (n)	Molar concentration
10	0.05
6.5	0.15
4	0.2

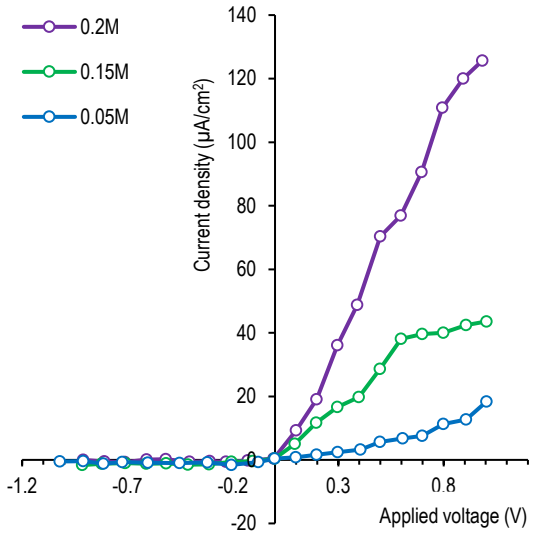

Fig. (1) The variation of I-V characteristics in dark

It was also noted that the heterojunction is anisotype due to the different behavior of the forward bias current from that of the reverse bias current. The ideality factor of the heterojunctions prepared using different molar concentrations was calculated from the following equation $n=qV\backslash k_B.\ln(I_f/I_{sat})$, were V is the applied voltage, I_f is the forward bias current, and I_{sat} is the saturation current. They were found in order the ideality factor be more than one. This behavior is attributed to more than one mechanism to transmit the current due to the lattice mismatch between In_2S_3 and Si, and also due to the crystal defects that may occur during the deposition process. Note that the value of ideality factor decreases with increasing molar concentration.

Figure (2) represents the I-V characteristics of the heterojunctions under the irradiation in the reverse bias condition. The detector was exposed to white light and the photocurrent increased with the increasing of the incident light intensity, which leads to an increase in the generation of photocarriers within the depletion region. The diffusion of carriers results in the generation of electron-hole pairs. Also, the internal electric field prevents the recombination of electrons with the holes. As well, the photocurrent increased with the increases in the applied potential difference in the reverse bias because the width of the depletion region increases with the increase in the applied potential difference and the absorption of light within the region close to it. As it is clear from Fig. (2), the deposited films at 0.2M show rough surfaces, which help the film material interacting with more incident photons and at different angles of incidence, which leads to an increase in the absorption of photons by trapping light, and thus increases the optical sensitivity of the photodetector.

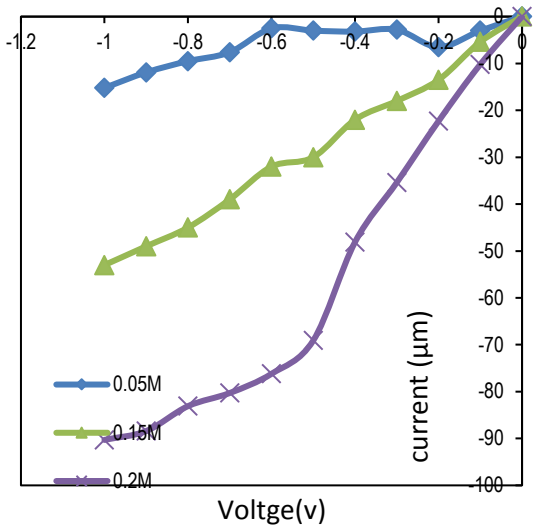

Fig. (2) The I-V characteristics of the heterojunctions under irradiation in the reverse bias

Figure (3) shows the variation of the spectral responsivity (R_λ) of the In_2S_3/Si photodetector as a function of the wavelength for different molar concentrations. It is noted from the figure that there are two peaks in the responsivity spectrum, the first belongs to the detector material In_2S_3 and the second peak belongs to silicon. The highest value of the responsivity was about 0.8 A/W at 450 nm and up to 1.05 A/W at 700 nm at a concentration of 0.2 M. We found from the spectral responsivity curves that the responsivity increases with the increase in molar concentration due to the increase in the growth rate, the improvement of crystalline structure of the films, and the lattice and thermal mismatch of the two heterojunction materials, which leads to a decrease in the series resistance due to the increase in the conductivity of the reagent material as well as to the increase in the film thickness. These results agree with the results of reference [20-22].

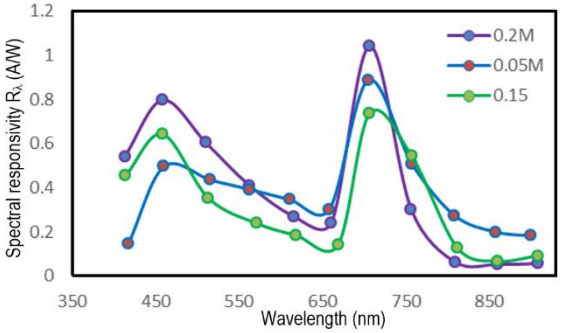

Fig. (3) The variation of the spectral responsivity of the In_2S_3/Si photodetector as a function wavelength

 ISSN (print) 1813-2065, (online) 2309-1673

Figure (4) indicates that the quantum efficiency (η) of the In_2S_3/Si heterojunction photodetector as a function of the wavelength for different molar concentrations. It was found that the highest value of the efficiency of 3.5% at 700 nm was recorded at concentration of 0.2 M. This is due to an increase in the particle size and the film thickness as well.

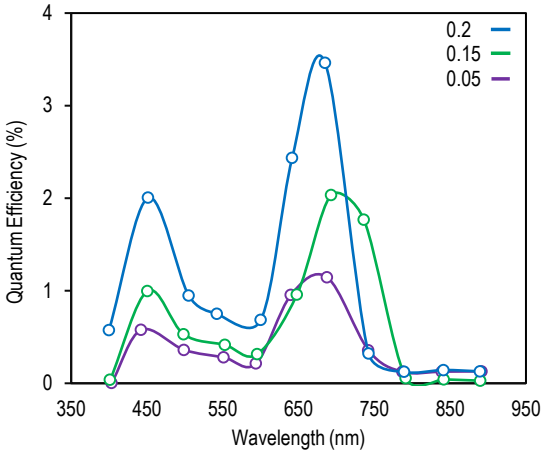

Fig. (4) The variation of the quantum efficiency of the In_2S_3/Si photodetector as a function wavelength

Figure (5) shows the specific detectivity of the In_2S_3/Si photodetector as a function of the wavelength with different molar concentrations. The optimum value was $2.94x10^{11}$ cm.$Hz^{1\backslash2}$/W at 450 nm. The increase in the molar concentration leads to increase the specific detectivity due to the increase in the spectral responsivity.

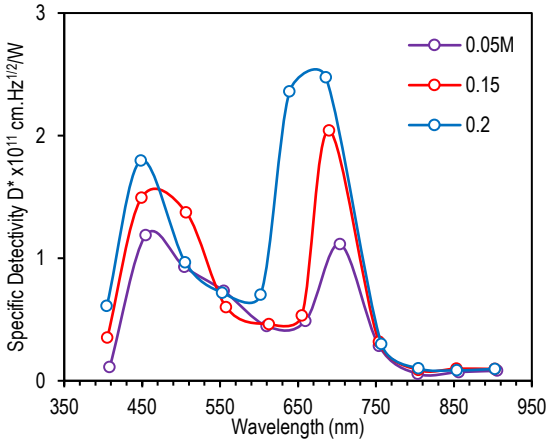

Fig. (5) The variation of the specific detectivity of the In_2S_3/Si photodetector as a function wavelength

4. Conclusions

Photodetectors were fabricated from In_2S_3/Si thin film heterojunctions by thermal chemical spraying technique with molar concentrations of 0.05, 0.15, and 0.2 M at temperature of 310°C. The I-V characteristics of the In_2S_3/Si heterojunctions in the dark was determined and the heterojunction was found to be anisatype. The value of the ideality factor of the prepared heterojunctions was greater than one due to the lattice mismatch between the In_2S_3 and silicon as well as because of the presence of some crystalline defects that may occur during the preparation process. Two peaks of spectral response were obtained, the first belongs to the In_2S_3 material and the other belongs to silicon. The highest quantum efficiency of the prepared photodetectors was obtained to be 3.5% at a concentration 0.2 M. The possibility of using these In_2S_3/Si heterojunctions prepared by thermal spraying technique in many applications can be confirmed.

References

[1] E. Shazly and A. Abd Elhady, "Electrical properties of β-In2S3 thin films", *J. Phys. Cond. Matter*, 10(59) (1998) 43-54.

[2] K. Benchouk et al., "Optical and electrical characterization of In_2S_3 buffer layer for photovoltaics applications", *Physica Procedia*, 2 (2009) 971-974.

[3] O.A. Hamadi, "Characteristics of CdO-Si Heterostructure Produced by Plasma-Induced Bonding Technique", *Proc. IMechE, Part L, J. Mater.: Design & Appl.*, 222 (2008) 65-71.

[4] O.A. Hamadi and K.Z. Yahiya, "Optical and electrical properties of selenium-antimony heterojunction formed on silicon substrate", *Sharjah Univ. J. Pure Appl. Sci.*, 4(2) (2007) 1-11.

[5] O.A. Hamadi, B.A.M. Bader and A.K. Yousif, "Electrical Characteristics of Silicon p-n Junction Solar Cells Produced by Plasma-Assisted Matrix Etching Technique", *Eng. Technol. J.*, 28 (2008).

[6] O.A. Hamadi, "Effect of Annealing on the Electrical Characteristics of CdO-Si Heterostructure Produced by Plasma-Induced Bonding Technique", *Iraqi J. Appl. Phys.*, 4(3) (2008) 34-37.

[7] R.A. Ismail et al., "Full characterization at 904 nm of large area Si p-n junction photodetectors produced by LID technique", *The Euro. Phys. J. – Appl. Phys.*, 38(3) (2007) 197-201.

[8] O.A. Hammadi, "Electrical and Spectral Characteristics of Visible-Blind ZnO/Si Heterojunction Fabricated by Plasma-Induced Bonding", J. Optoelctron. Photon., 7(5) (2016) 21-24.

[9] N. Barean, and J. Berned, "Recent studies on In2S3 containing oxygen thin films", *Solid State Commun.*, 122 (2012) 445-450.

[10] R.A. Ismail et al., "Characterization of Si p-n Photodetectors Produced by Laser-Induced Diffusion", *Int. J. Mod. Phys.*, 19(31) (2005) 4619-4628.

[11] O.A. Hamadi, "Profiling of Antimony Diffusivity in Silicon Substrates using Laser-Induced Diffusion Technique", *Iraqi J. Appl. Phys. Lett.*, 3(1) (2010) 23-26.

[12] A.A.K. Hadi and O.A. Hamadi, "Optoelectronic Characteristics of As-doped Si Photodetectors Produced by LID Technique", *Iraqi J. Appl. Phys. Lett.*, 1(2) (2008) 23-26.
[13] O.A. Hammadi, M.K. Khalaf and F.J. Kadhim, "Fabrication of UV Photodetector from Nickel Oxide Nanoparticles Deposited on Silicon Substrate by Closed-Field Unbalanced Dual Magnetron Sputtering Techniques", *Opt. Quantum Electron.*, 47(12) (2015) 3805-3813.
[14] Ch. Bao et al., "Low-noise and Large-Linear-Dynamic-Range Photodetectors Based on Hybrid-perovskite Thin–single crystals", *Adv. Mater.*, 29(39) (2017).
[15] R. Mohamed and, L. Amalraj, "Effect of precursor concentration on physical properties of nebulized spray deposited In_2S_3 thin films", *J. Asian Cer. Soc.*, 4 (2016) 357-366.
[16] O.A. Hammadi, M.K. Khalaf and F.J. Kadhim, "Fabrication and Characterization of UV Photodetectors Based on Silicon Nitride Nanostructures Prepared by Magnetron Sputtering", *Proc. IMechE, Part N, J. Nanomater. Nanoeng. Nanosys.*, 230(1) (2016) 32-36.
[17] O.A. Hammadi, "Characteristics of Heat-Annealed Silicon Homojunction Infrared Photodetector Fabricated by Plasma-Assisted Technique", *Phot. Sen.*, 6(4) (2016) 345-350.
[18] A.K. Yousif and O.A. Hamadi, "Plasma-Induced Etching of Silicon Surfaces", *Bulg. J. Phys.*, 35(3) (2008) 191-197.
[19] B.A.M. Badr, O.A. Hamadi and A.K. Yousif, "Measurement of thermooptic coefficient of semiconductors by single-beam scanning technique", *Eng. Technol. J.*, 27(5) (2007).
[20] N.F. Habubi, R.A. Ismail and M.M. Abbod, "The effect of molarity on some physical properties of In_2S_3 thin films deposited by chemical spray pyrolysis technique", *Int. Lett. Chem. Phys. Astron.*, 63 (2016) 134-140.
[21] O.A. Hammadi and M.S. Edan, "Temperature Dependencies of Refractive Index and Optical Elasticity Coefficient on Lens Induced in Nd:YAG Crystal", *Iraqi J. Appl. Phys.*, 8(1) (2012) 35-41.
[22] O.A. Hamadi, N.J. Shakir and F.H. Mohammed, "Magnetic Field and Temperature Dependent Measurements of Hall Coefficient in Thermal Evaporated Tin-Doped Cadmium Oxide Thin Films", *Bulg. J. Phys.*, 37(4) (2010) 223-231.

 ISSN (print) 1813-2065, (online) 2309-1673

IRAQI JOURNAL OF APPLIED PHYSICS
EDITORIAL BOARD

COPYRIGHT RELEASE FORM
IRAQI JOURNAL OF APPLIED PHYSICS (IJAP)

We, the undersigned, the author/authors of the article titled

……
……
……
……
……
……
……

that is submitted to the Iraqi Journal of Applied Physics (IJAP) for publication, declare that we have neither taken part or full text from any published work by others, nor presented or published it elsewhere in any other journal. We also declare transferring copyrights and conduct of this article to the Iraqi Journal of Applied Physics (IJAP) after accepting it for publication.

The authors will keep the following rights:

1. Possession of the article such as patent rights.
2. Free of charge use of the article or part of it in any future work by the authors such as books and lecture notes after informing IJAP editorial board.
3. Republishing the article for any personal purposes of the authors after taking journal permission.

To be signed by all authors:

Signature:……..date: ……
Printed name: ……

Signature:……..date: ……
Printed name: ……

Signature:……..date: ……
Printed name: ……

Correspondence author:……..……...……...
……
Address:……..……
……
Telephone:……..……..email: ……

Note: Complete and sign this form and mail it to the below address with your finally revised manuscript

The Iraqi Journal of Applied Physics
P. O. Box 88052, Baghdad 12631, IRAQ
www.iraqiphysicsjournal.com
Email: info@iraqiphysicsjournal.com
Email: editor_ijap@yahoo.co.uk
Email: ijap.editor@gmail.com

IRAQI JOURNAL OF APPLIED PHYSICS

Volume (19) Issue (3B) September 2023

CONTENTS